Earthshine and the Earth's Albedo

A [1,2], B[2], C[3] and D[3]

[1] U1

[2] U2

[3] U3

Received _____; accepted _____

ABSTRACT

Subject headings: Earth : albedo, global climate — Moon: reflection

Since late 1998 sustained observations of the earthshine have been made in California from Big Bear Solar Observatory. We also have intermittant observations from 1994-5. We have re-invigorated and modernized a nearly forgotten way of measuring the earth's albedo, and hence its energy balance. For about a quarter-century, early in the last century, Danjon and his followers observed the earthshine from France.

From California, we see the moon reflecting sunlight from Asia in our evening – before midnight – which is during the moon's rising phase, and from Europe in our morning – after midnight – which is during the moon's declining phase. We have precisely measured the scattering from the moon, as a function of lunar phase, which enables us to measure, in a typical night's observations, the earth's albedo to an accuracy of 2.0% (equivalent to measuring the earth's emission temperature to ~ 0.8 K). The albedo is due to the interplay of cloud cover and the different landscapes. In the observations, we see large variations in the earthshine from night to night, $\sim 5\%$, due to weather changes on the other side of the world. Averaging the data, we also see seasonal changes, upwards of 20%, with the earth being brightest in the spring.

We also find a favorable comparison of our results to models of the earth's reflectance which use as input cloud cover from satellites – with the trends from the model being muted in comparison to those from the earthshine data. Thus, our earthshine results imply that the models show variations which are too small, as though terrestrial features are overly smoothed in the models. Using satellite cloud cover data to extend our model results back over a solar cycle, we find variations in the power going into the earth's climate system are about five times more sensitive to the changes in the earth's albedo than to changes in the solar irradiance.

1. Introduction

It is important to know whether there is an on-going global change in the earth's climate. To answer this, one needs precise, global/integrated measures of relavent quantities. The earth's climate is driven by the net sunlight deposited in the terrestrial atmosphere, and so, is critically sensitive to the solar irradiance and the earth's albedo. Precise measurements of the solar irradiance have been made by various satellites (REFERENCES) and using ground-based proxies (REFERENCES). The spectrum of efforts to determine the earth's global albedo is not so rich. There have been efforts using systems of satellites (REFERENCES), but virtually no efforts from the ground. Nonetheless, the earth's energy balance is determined in large part by its global albedo – the fraction of the incident sunlight that is directly reflected back into space without altering the internal energy budget of the atmosphere. The earth's surface, aerosols in the atmosphere, and clouds all reflect some of the incoming solar short-wavelength radiation, preventing that energy from warming the planet. Short-wavelength radiation, usually defined as having wavelengths between 0.15 and 4.0 μm, includes about 99% of the sun's radiation; of this energy, 46% is infrared (> 0.74 μm), 9% is ultraviolet (< 0.4 μm) and the remaining 45% is visible, with wavelengths between 0.4 and 0.74 μm. A significant portion of the solar energy is absorbed by the earth, where it drives terrestrial phenomena before being radiated back into space. This long-wavelength radiation peaks at about 15 μm (corresponding to a black-body temperature of about $T_E = 255$ K).

The power going into the earth's climate system is

$$P_{in} = C\pi R_e^2(1 - A), \tag{1}$$

where C is the solar constant, R_e is the earth's radius and A is the short-wavelength Bond albedo (reflectivity). Similarly, the long-wavelength power that the earth radiates into space is

$$P_{out} = 4\pi R_e^2 \sigma \epsilon T_e^4, \tag{2}$$

where σ is the Stefan-Boltzmann constant and ϵ is the emissivity of the atmosphere (about 5.5 km

high, where the long-wavelength radiation is emitted).

If the planet is in radiative equilibrium, $P_{in} = P_{out}$, and we have

$$T_e^4 = \frac{C}{4\sigma\epsilon}(1 - A). \tag{3}$$

This means that the Bond albedo directly controls the earth's temperature. Global warming would result if A and/or ϵ decreased. By measuring the earth's reflectance and the spectrum of the reflected light, one can determine A and ϵ, respectively.

It has been known for some time that the so-called solar constant varies. In particular, data from the Active Cavity Radiometer (ACRIM I) on board the Solar Maximum Mission has shown for one cycle ($\sim$ 11 years) that the solar irradiance is about 0.1% greater at activity maximum than activity minimum (Willson and Hudson 1988, 1991). The precise origin of the changing irradiance is generally attributed to a competition between two components of the sun's magnetic field – dark sunspots and bright faculae. It is conventional wisdom that this is about several times too small to be climatologically significant over a solar cycle (REFERENCE). It has been argued that there may have been two to three times larger, sustained excursions (Lean 1997) in the recent past, like during the little ice age when a sunspot was rare. Still, there is strong evidence of a solar cycle going back more than 100,000 years (Ram and Stoltz 1999). If the 0.1% increase in the mean solar irradiance between the mid-1980s and 1990 were typical, it leads one to ask if it is the direct effect of varying solar magnetism on the irradiance that causes the dominant terrestrial signature of the solar cycle. Svensmark and Friis-Christensen (1997) have argued that indirect effect of the sun's magnetic magnetic activity cycle has a much greater terrestrial significance than the irradiance variations.

Svensmark and Friis-Christensen (1997) have studied satellite cloud cover data and measured a 3-4% greater cloud cover at solar activity minimum. They argue that this implies solar cycle changes in radiative input are about an order of magnitude larger than those implied by observed solar irradiance variations over the cycle. They further argue that the source of the excess cloud cover is the relatively greater cosmic radiation at activity minimum which arises from the sun's

magnetic field being weaker at activity minimum and, thereby, being less effective in shielding the earth from cosmic radiation. According to their argument, the relatively greater cosmic radiation creates relatively more ions which have a correspondingly greater cloud-seeding effect. The details of their interpretation of the cloud data may or may not be correct, but the apparent terrestrial magnification of solar effects emphasizes the importance of looking for long term trends in the albedo as an indicator of global climate change.

One might anticipate that global changes in the earth's climate would be reflected in changes in the earth's albedo. Here, we focus on a terrestrial determination of the earth's global albedo from an old, and largely forgotten method. That is, global albedo can be determined by measuring the amount of sunlight reflected from the earth and in turn, back to the earth from the dark portion of the face of the moon (the "earthshine" or "ashen light"). The most important historical program of earthshine measurements was carried out by Danjon (1928, 1954) from a number of sites in France. He used a "cat's-eye" photometer to produce a double image of the moon, allowing the visual comparison of the intensities of two well-defined patches of the lunar surface−−one in sunlight and the other in the earthshine−−at various lunar phases. Using the "cat's-eye" mechanism, he stopped down the light from the sunlit portion to match the brightness of the ashen portion. This differential measurement removed many of the uncertainties associated with varying atmospheric absorption and the solar constant, allowing Danjon to achieve an estimated uncertainty of roughly 5%. Our measurements are about an order of magnitude more precise, not simply because we have better cameras available, but we have also solved the problem of the uncertainty in the scattering from the moon as a function of the phase of the moon (see §5). At a better than 1% precision, our terrestrial measurements of the earth's albedo have a precision comparable to that from satellites.

From 1926 to 1930, Danjon made 207 measurements of earthshine. Dubois (1947) continued the program through 1960 from the observatory at Bordeaux using a Danjon-type photometer.

Danjon's and Dubois' results show a number of interesting features. The daily mean values of the observations vary more widely than would be expected on the basis of the variation of

measurements on a single night. This can be plausibly attributed to daily changes in cloud cover, but extensive cloud-cover data were not available at the time of the observations.

Danjon (1928) also examined his observations to determine whether there was a long-term trend in albedo, but found none. Dubois' observations for some 20 years ending in 1960, showed considerable annual variability, which he speculated was due to solar activity. His published monthly variations from 1940-1944 also show a strong correlation with the 1941-42 El Niño. In the past forty years, there have been observations of earthshine by Huffman et al. (1989) and one-time observations by Franklin (1967) and Kennedy (1969).

Danjon used his observations to estimate the mean global albedo. Since the observations are only at visible wavelengths, they must be corrected for the balance of the short-wavelength radiation, most of which is in the near IR. Estimates of this correction were made by Fritz (1949), after taking into account the decrease of the earth's albedo with increasing wavelength (our "blue planet"). Fritz also attempted to correct for the geographical bias in Danjon's observations. The western hemisphere, which was most frequently observed by Danjon, has a greater fraction of land than does the globe as a whole, implying that Danjon's value would be high because the sea is dark compared to land. Combining the decreases from the absence of the IR and geographical bias, Fritz found that Danjon's visual albedo of 0.40 corresponds to a Bond albedo (considering all the wavelengths and directions) of 0.36.

Flatte et al. (1991) noted that a correction must be made for the "opposition effect" present in lunar reflectance properties. Observations of the moon show that the moon's reflectivity has a strong angular dependence. This "lunar phase function" can rise by as much as a factor of two in going from 5° to 0° (exact backscattering). This enhancement was once thought to be due to the porous nature of the lunar surface (Hapke 1971) and was unknown in Danjon's time. More modern work has shown it to be caused by coherent backscatter in the lunar soil. The smallest lunar phase angle measured by Danjon was only 11°. The extent of the small-angle rise varies over different regions of the lunar surface, but can easily be the 20% required to reduce Fritz's value of 0.36 to the generally recognized standard of about 0.30 (Buratti et al. (1997)). In fact, we shall

see in §10 that an incorrect lunar phase function is the primary source of Danjon's overly large visual albedo.

The observations reported here were carried out at Big Bear Solar Observatory (BBSO) beginning December 1998, with some intermittent observations from 1994-5, using our earthshine telescope. Our initial results covering from the end of 1998 through the middle of 2000 were described in Goode et al. (2001). We found that the earthshine yielded an albedo of 0.295±0.005 for the 2/3 of the earth seen from BBSO. We also used satellite cloud cover data to determine a comparable albedo, 0.297±0.002, for the same parts of the earth at the same time. We also found upwards of 20% seasonal variation in the earth's reflectance – much large than the modeling implied. We also showed the method was sufficient to detect El Niño events and volcanic eruptions. Finally, we sound the hint of a solar ccycle variation of the earth's reflectance (cloud cover) being larger at solar activity minimum than at activity maximum. The observations are described in detail in §3. We note that our CCD detector has sufficient resolution and dynamic range to observe both the sunlit and earthshine portions of the moon in the same image (although a dark filter is usually interposed on the bright crescent to prevent blooming), so that we alternate observing the earthshine and "moonshine" (bright side). We report the results of our data including synoptic, seasonal, and annual variability.

As mentioned, we also make detailed comparisons of our observational results with the first modern modeling of earthshine. These calculations used ERBE scene models (Suttles et al. 1988). For the snow and ice cover information, we use simulations from the Canadian Center for Climate Modeling and Analysis (`http://www.cccma.bc.ec.gc.ca`), which gives the monthly mean snow/ice cover for each computational cell ($2.5^\circ \times 2.5^\circ$). The cloud cover data, updated every 6 hours, are a whole earth composite of visible-light satellite images from WSI-INTELLICAST (`http://www.intellicast.com/`). Model results, contemporaneous to the observations to which they are compared, are presented and discussed in §8.

2. Determining the Earth's Reflectivity from Earthshine

Terrestrial measurements of the short-wavelength (visible light and near infrared) albedo of a planet in our solar system is relatively straightforward – except for the earth. However, we can determine the albedo from the ground by measuring the earthshine. From a terrestrial perspective, the earthshine is the sunlight reflected from the bright side of the earth to the moon and finally back to an observer on the dark side of the earth. At any moment, the earthshine can provide an instantaneous, differential cross-section of the sunlight reflected from the earth, see Figure 1.

The earth's differential cross-section depends on its geometrical albedo and its phase function. The geometrical albedo is independent of β, rather it is proportional to the backscattered cross-section. At the earth's surface, the differential cross-section of the reflected sunlight for scattering by an angle β (note that β is the supplement of the usual scattering angle) is given by

$$\frac{d\sigma}{d\Omega} \equiv p_e f_e(\beta) R_e^2, \tag{4}$$

where R_e is the radius of the earth, p_e is the geometrical albedo of the earth and $f_e(\beta)$ is the earth's phase function, defined such that $f_e(0) = 1$, as can be seen in the Lambertian limit from Equation (7).

Using Equation (4), we can write the total scattering cross section as

$$\sigma = \int \frac{d\sigma}{d\Omega} d\Omega = \pi R_e^2 p_e \int_{-\pi}^{\pi} f_e(\beta) \mid \sin(\beta) \mid d\beta, \tag{5}$$

where p_e and f_e depend on the earth's weather, season and climate. Additionally, f_e depends on the earth's aspect.

From the total cross-section, we can define the Bond albedo, the fraction of solar energy incident on the planet that is reflected as

$$A = \frac{\sigma}{\pi R_e^2} = p_e \int_{-\pi}^{\pi} f_e(\beta) \mid \sin(\beta) \mid \beta. \tag{6}$$

Using earthshine data, we integrate over the phases of the moon to determine, say, a seasonally averaged Bond albedo. β varies between 0 and $\pm\pi$, with -π to 0 being the waxing moon and 0 to π being the waning moon.

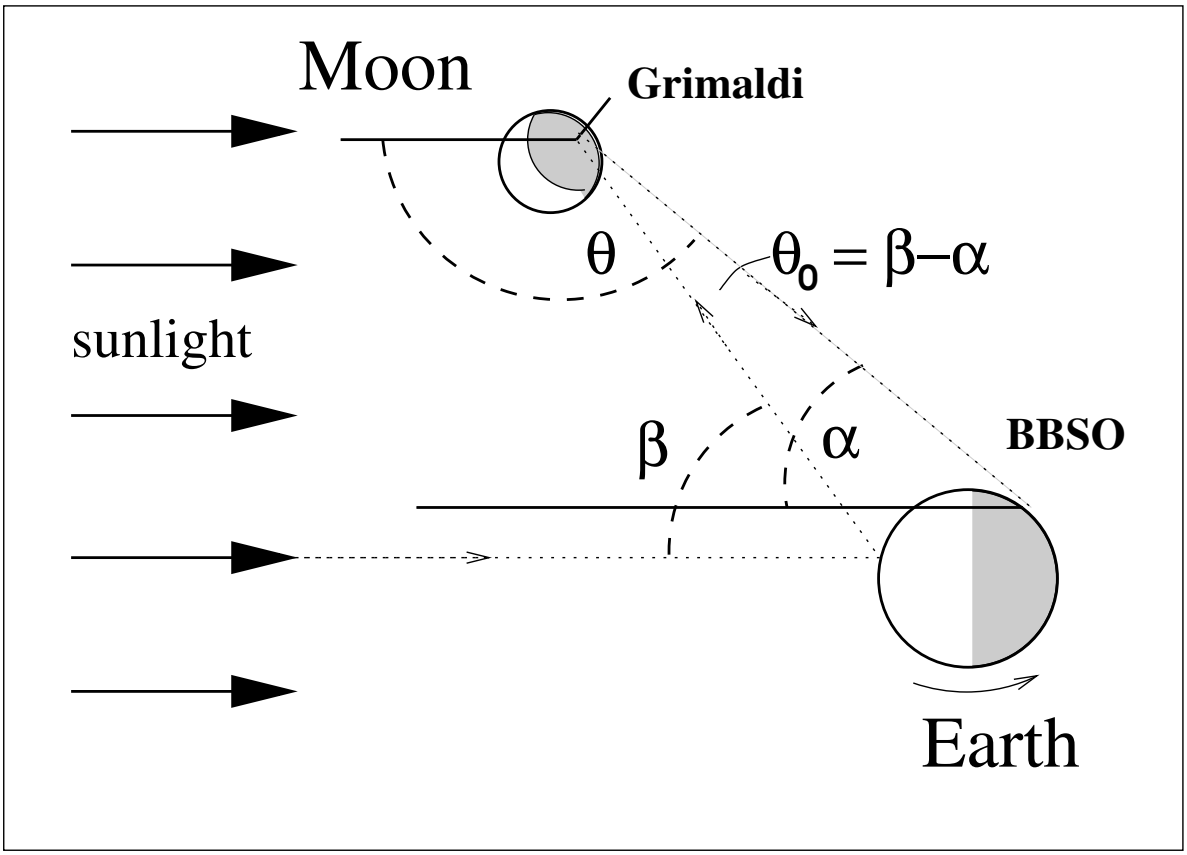

Fig. 1.— A not-to-scale cartoon of the sun-earth-moon system defining the earth's topocentric phase angle, α, with respect to BBSO. The plot also shows the moon's selenographic phase angle, θ, with respect to one of the fiducial points (Grimaldi) used in the observations made from BBSO (also indicated). β is the angle between the sunlight that is incident somewhere on the earth and reflected, as earthshine, to Grimaldi. $\theta_0 (= \beta - \alpha)$ is angle between the earthshine that is incident and reflected from the moon. The path of the earthshine is indicated by the arrows. θ_0 is less than 1°.

If we assume that the earth is a Lambert sphere, we can do the integral in Equation (5) exactly. A Lambert sphere reflects isotropically from its assumed to be fully diffusive surface. Then, f_L, the earth's Lambert phase function, is determined by

$$f_L(\beta) = \frac{(\pi - \mid \beta \mid)\cos\beta + \sin \mid \beta \mid}{\pi}. \tag{7}$$

The earth's phase function is very roughly Lambertian for $\mid \beta \mid \leq \frac{2\pi}{3}$ (see §6). Under this assumption, we determine a simple proportionality between the geometric albedo and the global or Bond albedo, namely,

$$p_{e,L} = \frac{2}{3} A_{B,L}. \tag{8}$$

Again, modeling shows that the earth's phase function is approximately Lambertian for $\beta \leq \frac{2\pi}{3}$. Thus, a convenient, differential measure of the earth's reflectivity is the effective albedo, A^*, where

$$A^* \equiv \frac{3}{2} \frac{p_e f_e}{f_L}. \tag{9}$$

which is the albedo of a Lambert sphere that would give the same instantaneous reflectivity as the true earth.

At that instant, an observer on the moon in the region illuminated by the sun and visible from the earth would see both the direct sunlight and some part of the sunlit earth. The solar intensity seen by that observer would be

$$I_s = \frac{C}{R_{ms}^2}, \tag{10}$$

where C is the solar constant and R_{ms} is the moon-sun distance measured in astronomical units. Similarly, the intensity of the earthlight would be

$$I_e = \frac{C}{R_{es}^2} p_e f_e(\beta) \frac{R_e^2}{R_{em}^2}, \tag{11}$$

where R_{ms} and R_{es} are the moon-sun and earth-sun distances, respectively. Thus, the earth's reflectivity can be expressed as

$$p_e f_e(\beta) = \frac{I_e}{I_s} [\frac{R_{em}}{R_e}]^2 [\frac{R_{ms}}{R_{es}}]^2. \tag{12}$$

In the observations, we study pairs of diametrically opposite fiducial patches, one in the earthshine and the other in the "moonshine" (sunlight reflected from the moon to the earth) both near the night-time lunar limb. For our purposes here, we call a representative pair "a" and "b" and treat them as unit projected areas. If a is illuminated only by the earthshine, the intensity observed by an observer on the earth at a distance R_{oa} would be

$$I_a = I_e \frac{p_a f_a(\theta_0)}{R_{oa}^2} T_a, \tag{13}$$

where T_a is the transmission of the earthshine through the atmosphere, and $f_a(\theta_0)$ is the *lunar* phase function for the near retroflection from patch a, see Figure 1. Thus, I_a/T_a is the observed intensity at zero airmass. Similar to Equation (13), the intensity of the sunlit portion, b, would be

$$I_b = I_s \frac{p_b f_b(\theta)}{R_{ob}^2} T_b, \tag{14}$$

where θ is the lunar phase angle and θ, like α and β, varies between 0 and $\pm\pi$, and where the lunar phase function, $f_b(\theta)$ embodies the dependence of the fiducial patch on the angle between the sunshine and the moonshine, see Figure (1). Thus,

$$\frac{I_a/T_a}{I_b/T_b} = \frac{I_e}{I_s} \frac{p_a f_a(\theta_0)}{p_b f_b(\theta)} \frac{R_{ob}^2}{R_{oa}^2}, \tag{15}$$

and so

$$p_e f_e(\beta) = \frac{I_a/T_a}{I_b/T_b} \frac{p_b f_b(\theta)}{p_a f_a(\theta_0)} [\frac{R_{em}}{R_e}]^2 [\frac{R_{oa}}{R_{ob}}]^2 [\frac{R_{es}}{R_{ms}}]^2. \tag{16}$$

Since $[\frac{R_{0a}}{R_{0b}}]^2$ is so close to unity that we can safely set that factor in Equation (16) to unity. Thus, we determine that

$$p_e f_e(\beta) = \frac{I_a/T_a}{I_b/T_b} \frac{p_b f_b(\theta)}{p_a f_a(\theta_0)} [\frac{R_{em}}{R_e}]^2 [\frac{R_{es}}{R_{ms}}]^2. \tag{17}$$

We measure I_a and I_b in our nightly observations, and extrapolate to zero airmass (e.g., I_a/T_a). We have measured the lunar phase function quite accurately over the last two years. We use total eclipse data from 93November 29 to measure the ratio of the geometical cross-sections of the two fiducial patches, $\frac{p_b}{p_a}$. For our fiducial regions, this ratio ranges between 0.9 and 1.1. In §6, we combine Equations (9) and (17) to define our measure of the earth's reflectivity, A^*, in terms of measured quantities, including the varying earth-moon distance.

3. Observations: Earthshine Instrumentation and Data Acquisition

Earthshine observations are currently being carried out at BBSO. The earthshine telescope is aligned with, and mounted atop the 65 cm solar telescope. Figure 2 shows a schematic of the earthshine telescope.

3.1. Hardware

The basic optical components of the earthshine telescope consist of an f/15 telescope primary which is a 6-inch diameter air-spaced doublet. The telescope tube is attached and aligned with the 65 cm solar telescope, which enables us to use the large telescope's drive software, permitting tracking following the moon's variable rate. The tracking rate is updated, via software, every thirty minutes to match the changing lunar motion in the east-west direction. Minor north-south corrections are done with the telescope control paddle as needed during the course of the night's observations. The moon is initially acquired using a simple two-lens finder scope aligned with the other telescopes on the 65 cm main telescope. The 65 cm telescope is regularly re-balanced for equipment changes so that tracking stability is not a problem even with long exposures. The observatory dome is automated to follow the solar disk during daytime operation. However, the sensors that make this possible do not work for lunar observing, so the dome must be checked every thirty minutes, or so. At the end of the tube is a stray light field stop. The incoming moonlight passes the field stop, and then enters a light tight optical assembly box that holds the filters and camera optics.

In the box, just behind the tube field stop and just before prime focus, is the earthshine neutral density filter switcher. Two filters are placed in the switcher. The first neutral density filter is a Schott NG3 2mm (the laboratory measured transmission of the filter as a whole is 0.0115 from 4000-7000 Å) for the Bright Side (BS) measurements. The BS or moonshine filter covers the entire field of view and is in place to prevent camera saturation and to provide a reasonably long exposure time (several 100 ms) compared to the smallest exposure time for the camera (10 ms).

Thus, to determine the absolute value of the earth's reflectance, one needs to know precisely the transmission of this filter (§4.3). The second filter is a Schott NG10 2mm (transmission is about 2×10^{-5} 4000-6000Å), which is essentially a blocking filter to cut off the bright side of the moon to permit the dark side or earthshine (ES) observations. The ES filter covers the bright side of the moon to permit long, dark side exposures (∼60-150 s) to get optimal signal to noise for the ES images. The ES filter is carefully placed within the switcher filter holder, by hand, at the beginning of each observing session. Its location, designed to cover the terminator, depends on the phase and libration of the moon. Both filters were scanned to check transmission with wavelength at Gamma Scientific in San Diego using a Radoma spectroradiometer. Both filters were found to be well within the quoted Schott tolerances.

The prime focus is after the switcher, and it is closely followed by a flat field lens. Next in the optical train are two near IR filters that stop any light beyond 7000 Å from reaching the camera. An iris behind the near IR filters acts as a further stray light stop. Behind the iris is a camera lens that focuses the lunar image on the CCD. Between this lens and the camera is a space for a filter wheel which can be used for narrow band measurements. All elements are rail mounted for linear adjustments, and lens elements are in moveable $y - z$ mountings for fine adjustments. All fine-tuning was done in the Fall of 1998, and nothing has been changed on the system since the start of data acquisition in December 1998. The system was "frozen" to limit possible errors in calibrating the lunar phase function. Flat field images help to point out the location of occasional dust particles that get into the optics. Compressed air removes most particles, and when necessary, elements are removed for cleaning, and then are carefully replaced to preserve optical alignment.

The CCD camera used in our current earthshine observations is an Apogee 7. The camera is a 512 X 512 16-bit scientific system with a SITe back-illuminated, thinned silicon chip. This chip, which is one of SITe's highest grade, is designed for higher quantum efficiency than unthinned front illuminated chips – this advantage is most apparent toward the blue. One drawback of the higher efficiency SITe chip is its sensitivity to "after-images" caused by exposure to UV. Testing the earthshine system to limit this effect resulted in the following observing procedures: The UV

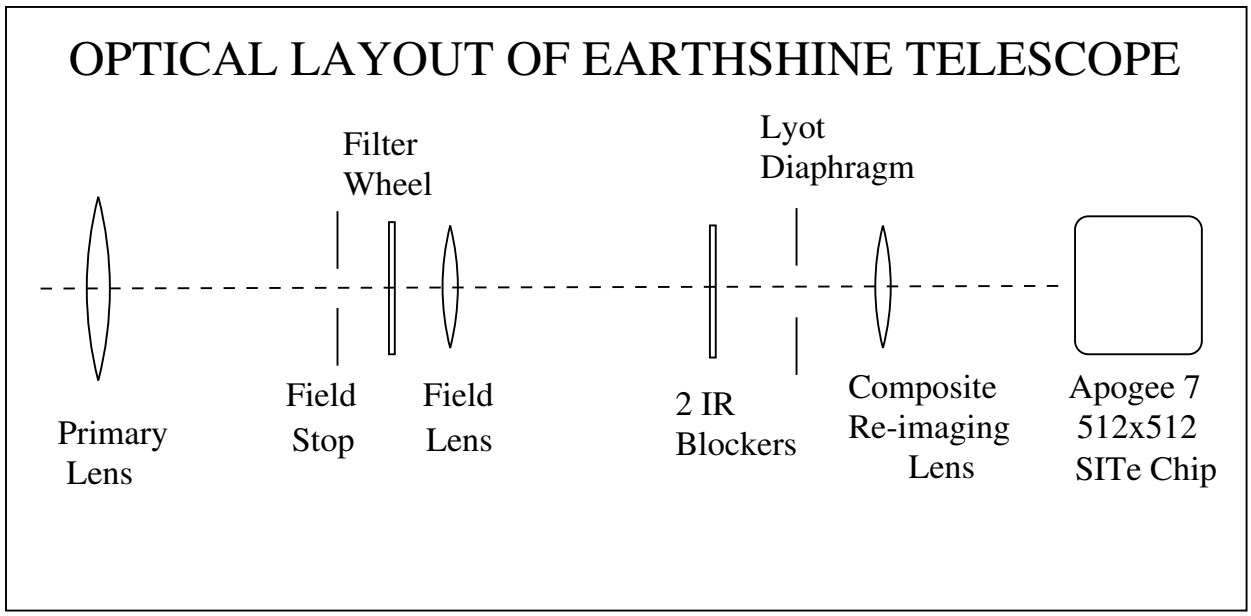

Fig. 2.— The optical set-up of the earthshine telescope.

from the BS images is blocked by the NG3 filter. The worst after-images show up in the ES images on the unfiltered half of the image – which are of long exposure. It was found that by increasing the number of short BS images, the UV residual image was removed. Careful examination of dark current and flat field images taken during the course of observations is done to confirm this, night by night.

Initial testing demonstrated a linear response over the camera's entire 16-bit range. To check for change in the camera's response with time, a calibrated radiometer was purchased to check the camera's responsivity during each new moon. Dome flats are taken in varying illumination to get pixel count versus intensity. The radiometer is an IL 1700, a NIST traceable Silicon photodiode radiometer. Once a year, the radiometer will be returned to International Light for re-calibration.

3.2. Observations

After initial tests, our current round of earthshine observations began in December 1998. A typical raw image is shown in Figure 3. The ten fiducial patches used in the data reduction (see

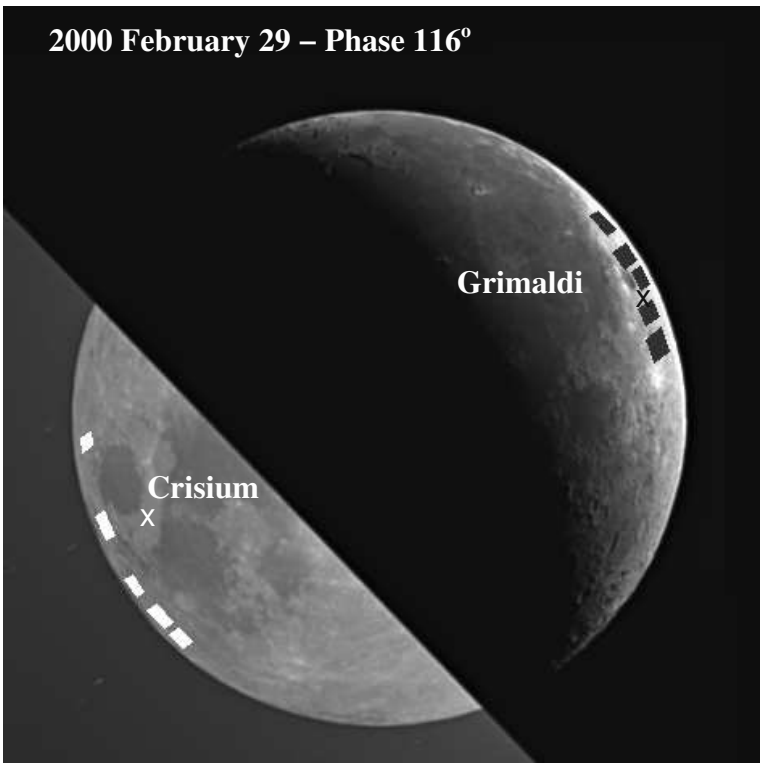

Fig. 3.— The moon showing the bright side and the earthshine. The Grimaldi side is in the moonshine and the Crisium side is in the earthshine. Our ten fiducial patches used in the observations made from BBSO are indicated. The crosses give the approximate positions of Danjon's fiducial patches. Goode et al. (2001) used one fiducial patch on each side, and on the Crisium side it is the one closest to the white cross, while on the Grimaldi side, it is the one immediately above the black cross. The lunar phase is 115°.9, near a declining quarter moon. The ES is flat across the disk. The flatness is due the uniform, incoherent back-scattering (non-Lambertian). Bear in mind that since the moon has no atmosphere, it doesn't have solar-like limb darkening.

§4) are also indicated. The camera's graphic user interface C code, supplied by the manufacturer, was modified to efficiently handle the routine earthshine observations. The nightly observations follow a simple set of procedures. Most are almost completely automated. To begin, a few initial images are taken to center the moon. When the image is centered, the ES filter is set by hand, and the observer moves downstairs to the control room. Then, more images are taken to determine the ES and BS exposures which optimize the signal to noise ratio. Finally, data are taken and stored. During the course of observations BS, ES, dark current, and flat field images are taken regularly.

The first 8 months of observations covered lunar phases between 0° and ±140°, which is about 21 days a month. The initial observation over this wide range of phases was necessary to determine the lunar phase function and prove its' repeatability. During the first 8 months, for the phases near the full moon (-40° through 0° to +40°), ES images were not taken because both fiducial patches were in, or so near to sunlight that ES measurements were unreliable. On these nights only BS, dark current, and flat fields, were taken to determine the scattering of light from the fiducial patches as a function of the phase of the moon. The lunar phase function was determined by July 1999, so that the BS-only nights were dropped – except for observations of the full moon. Full moon observations are still taken to determine the role of the opposition effect (REFERENCE) in the lunar phase function (phases -15° to +15°). Current earthshine observations cover about 14 days per month, and cover lunar phases between ±40° to ±150° centered on the first and last quarters of the moon when we have optimal conditions for measuring the earthshine – close to full-earth with a few hours of observations being possible. Data rates vary depending on phase. An average night will give about 1 image per minute. This means that the number of raw images saved for data reduction, varies between 100 to 600 per night.

4. Data Reduction

4.1. Image Analysis

The earthshine and moonshine intensities are measured by integrating the brightness of a pair of fiducial patches – one from the bright side and the other from the dark side of the lunar disk. In our study, ten physically fixed fiducial patches have been used with five in the earthshine and five in the moonshine, see Figure 3. In selenographic (lunar) coordinates, the center latitudes and longitudes of the five patches on the Crisium side are (-17.5, -70.), (-11.2, -71.5), (-5., -76.), (0., -75.), and (7.5, -76.5), and those of the five patches on the Grimaldi side are (28.5, 72.5), (12.5, 75), (0., 77.), (-7.5, 75.), and (-13., 75.). Each patch covers a longitudinal range of about 10 degrees and latitudinal range of 3 to 5 degrees, the surface area being about 0.1% of the lunar surface, which corresponds to about 100 camera pixels. These patches are located in the "highlands" of the lunar surface, and the physical reflectivity of each is roughly comparable. One of the patches on the Grimaldi side is very close to Danjon's choice, while the patches on the Crisium side are all closer to the limb than Danjon's patch (Figure 3).

To locate these patches in each lunar disk image taken every night, it is essential to establish the transformation between the CCD image coordinate system and the selenographic coordinate system. For this purpose, we first define the limb and center of the lunar disk for each image. Each of the raw lunar images is contrast-enhanced, and the limb points are defined by looking for suitable positions of large intensity gradient. Empirically, a minimum of 40 rim points need to be obtained, and are then used to make a Maximum Likelihood fitting to decide the lunar center in the image plane. Once the lunar center and limb are determined, the radius of the lunar disk is calculated in the CCD's coordinate frame. The next step is to define the position of the lunar pole in the image plane. To this end, some outstanding lunar features, whose precise selenographic coordinates are known, are used to co-register the two coordinate systems. The topocentric location of the lunar pole at any given moment can be precisely calculated using parameters from an astronomical almanac, from which one can determine the projected positions of these lunar

features in the image plane, which is perpendicular to the vector pointing from the local observer to the lunar center. By comparing these projected positions with the positions of these features in CCD coordinates, the angle between the projected N-S axis of the moon and the Y-axis of the CCD coordinate system is derived. [SOON I SHOUL DO ANOTHER THING TO DETERMINE THIS ONCE AND FOR ALL SO THAT WE DO NOT NEED THIS STEP ANY MORE AND THE ANALYSIS WILL BE FULLY AUTOMATIC @QJ]

Once the transformation between the image plane and the selenographic system is established, the five pairs of fiducial patches can be precisely located on the lunar disk image. The apparent areas of these patches change from night to night because of lunar libration. The intensity is read out as an average of the whole area, and the difference due to the geometric effect of the reflectivity arising from libration, is accounted for in our next step of data reduction (§4.2).

To ensure accurate photometry, flatfielding and dark current subtraction are performed on each image. For earthshine images, we also need to subtract the background scattering from the bright side of the moon. The background scattering should be a function of both the inclination of the vector connecting the lunar center and the background point with respect to the lunar equator, and the distance from the background point to the crescent. After experimentation, we found that we could safely assume that on the earthshine side, where the background points are not too close to the crescent, at a fixed inclination with respect to the lunar equator, the background intensity falls off linearly with the distance of the background point to the lunar center. Such a linear relation holds for the points which are not too far from the lunar equator. So, for each fiducial patch, centered on the vector connecting the lunar center and the patch, we open a small cone with an angular range of 5 degrees, and fit the intensities of the background points which are beyond the lunar limb and inside the cone, as a function of their distance to the lunar center. In this way, we can extrapolate the scattering intensity to the position of the fiducial patch using the parameters obtained from the least-square fit, and then subtract the linearly extrapolated value from the intensity of the fiducial patch. This procedure is illustrated in Figure 4.

In accordance with Equation (17), the intensity obtained from above is also corrected by

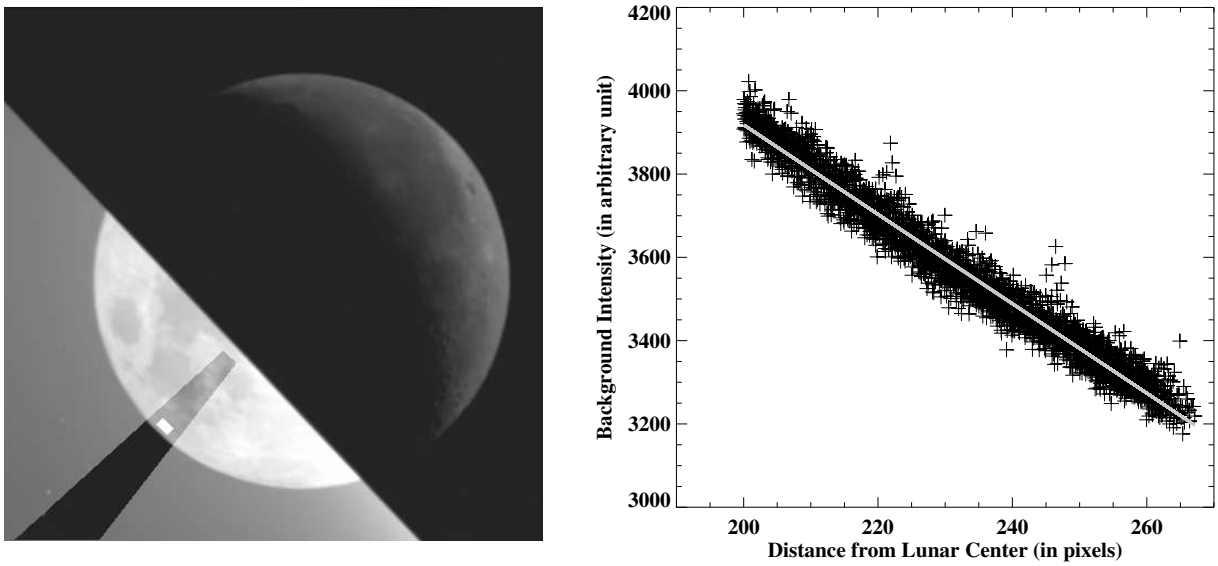

Fig. 4.— Illustration of the background subtraction for earthshine images. The image on the left shows a background cone around a fiducial patch, within which the intensity of the background points are read out to make a fit as a linear function of the distance from the lunar center. For the image shown the intensity inside the cone has the background subtracted already. The plot on the right shows the decline of the off-limb intensity as the background point gets further from the lunar center, and the overplottd thick grey line indicates the least-square linear fit.

scaling to a set of standard distances between the sun, moon and earth, before the successive steps of calibration described in the subsequent subsections. These distance parameters are obtained precisely from ephemeris.

4.2. Atmospheric Extinction

To eliminate the effect of the atmospheric extinction, observations are carried out for as long as possible during the night so that a measurement of the intensity at varying airmass can be obtained. For the bright side of the moon, the variation of the intensity should follow Beer's law:

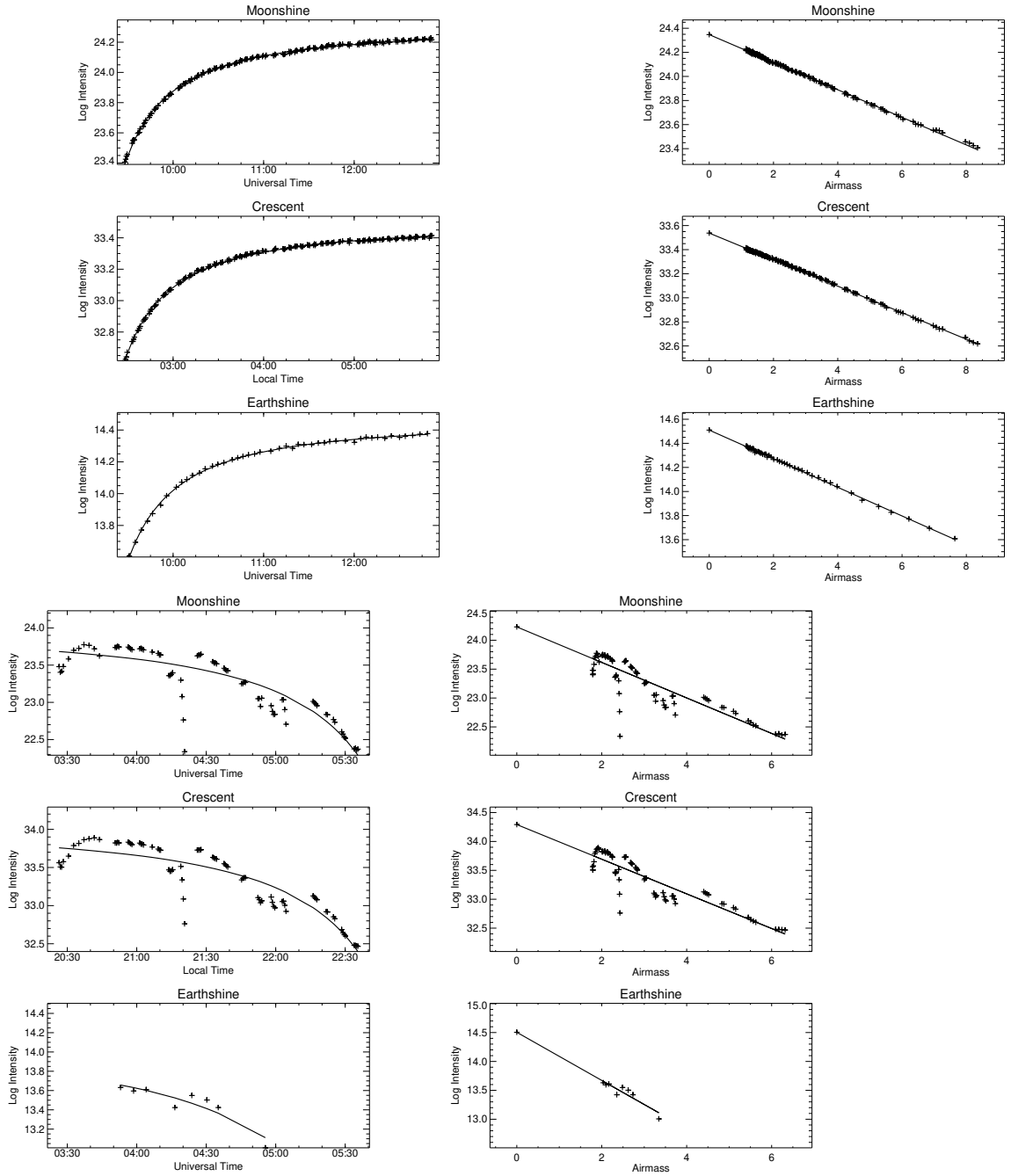

Fig. 5.— Each panel indicates either the moonshine (top panel of each triptych), the crescent (middle panel of each triptych), or the earthshine (bottom panel of each triptych) intensity plotted against time (on the left) and airmass (on the right). The "+" indicates observed data points and the solid lines are the fits to Beer's law. Upper six panels: data from the night on September 5, 1999, demonstrating typical good night, and the standard deviation of the fitting is 0.007, 0.005, 0.007 (from top to bottom). Lower six: data from the night on September 17, 1999, demonstrating a typical, partly cloudy night, and the standard deviation of the fitting is 0.219, 0.183, 0.077 (from top to bottom).

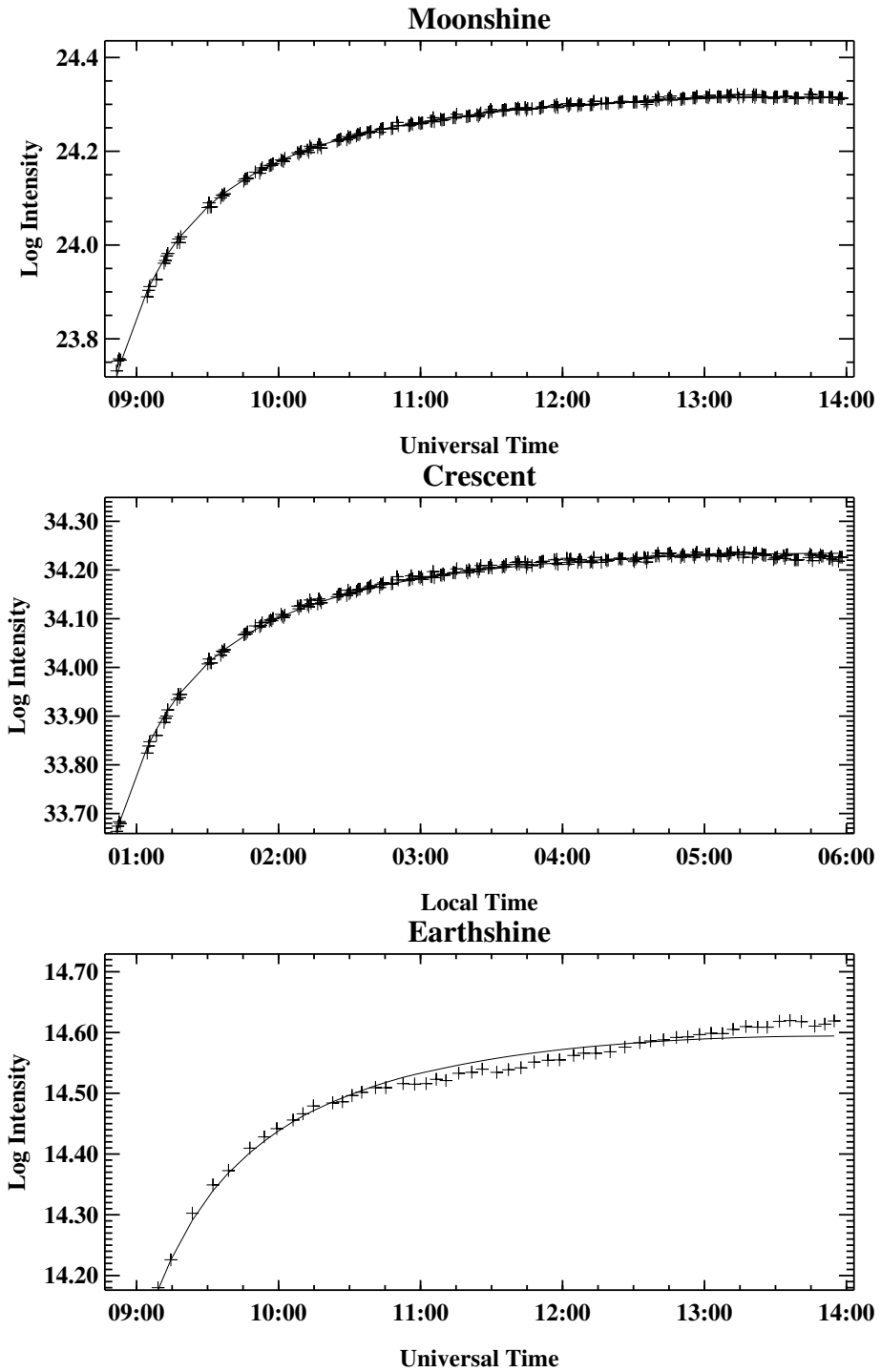

Fig. 6.— The moonshine, crescent and earthshine intensities and their Beer's law fit for the night of 2000 January 28, showing that while the moonshine and crescent intensity follows Beer's law very well, the earthshine intensity evolution deviates from Beer's law. The standard deviations of the fits are 0.004, 0.005, 0.014, respectively The fact that the fit is poor to the earthshine alone implies sizeable short-term variations in the earth's reflectance.

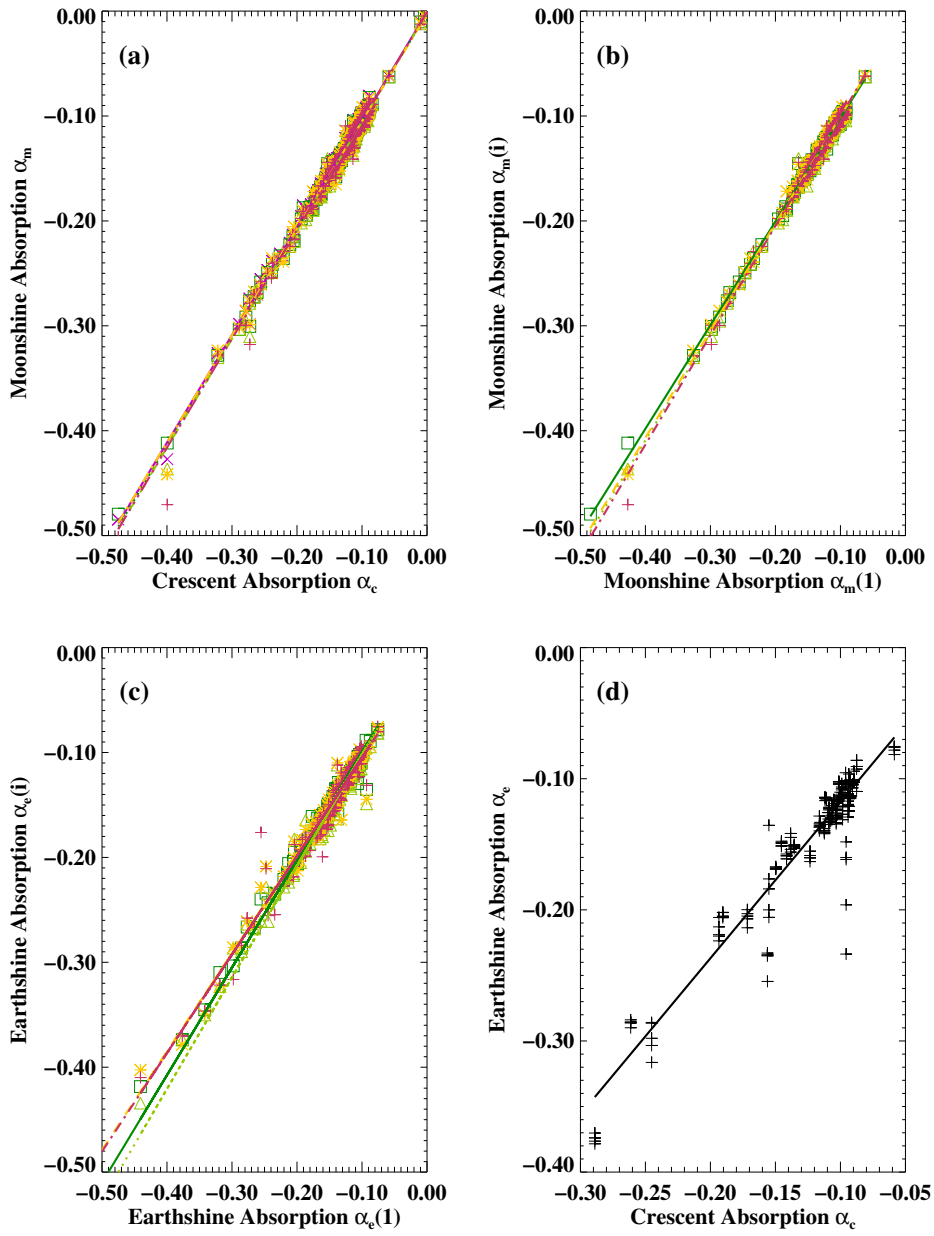

Fig. 7.— The variation of the atmospheric extinction coefficients for the crescent, (α_c), moonshine (α_m) and earthshine (α_e). Panel (a) illustrates α_m (for five fiducial patches as indicated by different symbols) against α_c; (b) shows α_m of four out of five fiducial patches (as indicated by different symbols) scaled to the fifth fiducial patch, illustrating that α_m is virtually the same for different patches; (c) shows α_e for four out of five fiducial patches (as indicated by different symbols) scaled against the other fiducial patch, showing that α_e is also the same for different fiducial patches in the earthshine; and (d) shows α_e (of all fiducial patches in earthshine) against α_c. The solid line in each panel indicates a least-square linear fit.

$$I = I_0 e^{(-\alpha z)}, \tag{18}$$

where I is the observed intensity, α is the atmospheric extinction coefficient, z is the local airmass and I_0 is the intensity at zero airmass – the intensity if the earth had no atmosphere.

The airmass, z , is determined from the angular altitude of the moon in the sky at different times in such a way that when the coaltitude θ_c - the inclination of the observer's line of sight with respect to the local zenith, which is the complement of the moon's angular altitude - is smaller than $60°$, $z = 1./\cos(\theta_c)$, otherwise z is interpolated from a standard airmass table (Table 1):

The above calculation refers to the airmass at sea level with the pressure $p_0 = 760$ mmHg and temperature $t_0 = 10°C$, and the real airmass at the observer's location must be corrected by a multiplicative factor of $p/p_0/(0.962 + 0.0038t)$ (REFERENCE: C. W. Allen, 1973, Astrophysical Quantities, p.125). BBSO is 2067m above sea level, and the pressure scale height at this altitude is 8200m, which yields $p = p_0 exp(-2067./8200.)$. We then incorporate the calculated z into the Beer's law fitting to determine α and I_0. We reckon that throughout a night, the evolving lunar phase function can also contribute to the changing intensity. The maximum phase change in a long night is less than two degrees, within which the intensity change is negligible compared to the change due to the airmass. Nevertheless, we employ a quasi-iterative way to correct this minor effect, in that we use an initial fit of the phase function (see the following section on how to obtain the phase function) to correct the data, and after the airmass correction, we make the phase function fit again. After a few iterations, the data converge to a stable result. The observed

Table 1: Standard Airmass Table (θ_c in degrees)

θ_c	60.	62.	64.	66.	68.	70.	72.	74.	76.	78.	80.
z	2.00	2.12	2.27	2.45	2.65	2.90	3.21	3.59	4.07	4.72	5.60
θ_c	81.	82.	83.	84.	85.	86.	87.	88.	89.	90.	-
z	6.18	6.88	7.77	8.90	10.39	12.44	15.36	19.79	26.96	40.00	-

intensity at each moment, I_i, is corrected, using the airmass, to the intensity at zero airmass, $I_i^0 = I_i \exp(\alpha z)$. I_0 from the fitting is further used as the intensity for that night's lunar phase function.

The goodness of the fit to Beer's law offers a ready criterion by which each night's local sky can be judged – the "good" night's data can be separated from that of the "bad" (noisy) nights (Figure 5). In practice, unless it is cloudy the data from almost all observable nights are preserved, and the standard error in the fitting for each night is further used as the input error for the lunar phase function fit. Figure 5 shows an example of a typical good night and a bad night, as judged by fitting to Beer's law. Experience from the observations shows that the data usually follow Beer's law quite well, and the accuracy of the moonshine fitting is often better than 1%. Among all the datasets collected for 320 nights from December 3, 1998 to November 30, 2000, for 147 nights, the accuracy of the fitting is better than 1%, and for 115 nights, the accuracy is between 1% and 2%.

In the case of earthshine intensity, apart from the atmospheric transmission, the evolution of the earthshine is also influenced by changing of the earth during a given night; e.g., the sun rising over a cloudy China. In addition, almost every month, on a few nights, we observe that the evolution pattern of the earthshine intensity does not track Beer's law in an unambiguous way, even though the moonshine intensity closely follows Beer's law. An example of such a case is shown in Figure 6. In general, the fit to the earthshine yields a standard deviation that is larger than that for the moonshine fitting by one-half to one percent. This latter difference contains the signal of the earth's albedo. On nights when the evolution of the earthshine evolution is significantly controlled by real changes in the earth's reflectance, apart from the atmospheric extinction, as illustrated Figure 6c, the atmospheric absorption coefficient α obtained from the Beer's law fitting of the earthshine observations may deviate from the true value. That is, some part of the earthshine signal may be subsumed by the atmospheric extinction coefficient, so that the correct of atmospheric attenuation cannot be properly determined from the standard Beer's law fitting.

To deal with this problem, we investigated the relationship between the earthshine coefficients, α_e, and the moonshine coefficients, α_m. As a reference, we have also examined α_m for different fiducial patches and α_c, the fitting parameter for the integral intensity of the whole crescent. Figure 7 (a) and (b) show the relationship between α_c and the $\alpha_m^i (i = 1, 2, 3, 4, 5)$ for all five fiducial patches. A least-square fit reveals that the α_m^i $(i = 1, 2, 3, 4, 5)$ can be regarded as being identical to one another, and to α_c. This is not a surprise even though the atmospheric attenuation is also a function of the wavelength (REFERENCE), as the light from a moonshine fiducial patch should have the same spectrum as the light from the whole bright side. Similarly, the earthshine absorption coefficient, α_e, is linearly correlationed with α_c (Figure 7 (d)), but the absolute value of α_e is systemetically larger than that of α_c, indicating a stronger atmospheric attenuation in earthshine than in moonshine. This is because the earthshine and the moonshine have different spectra; specifically, the earthshine is bluer than the moonshine because the bluer the light the more effectively the earth's atmosphere scatters it away.

The solution to fitting nights like those shown in Figure 6 lies in exploiting the linear scaling law that we find between α_e and α_c, which enables us to make a better determination of α_e from α_c for the nights when the usual, local airmass changes leading to a good Beer's law fit for the moonshine are compounded by sharp earthshine variations such that the mixture yields observational data that deviates sufficiently from Beer's law that one cannot be confident of the fit obtained in the usual way. Our solution lies is using α_c to fix α_e for the problematic nights, beginning with

$$\alpha_e = a \times \alpha_c + b, \tag{19}$$

where the scaling parameters a and b are obtained by a linear least-square fit of the above relation using α_e and α_c from the nights which do not show apparent global evolution that strays strongly from the Beer's law fit. We reckon that for the nights of significant global change, the standard deviation of the Beer's law fitting of the earthshine (σ_e) must be a lot larger than that of the crescent (σ_c), given that the local atmosphere is reasonably stable throughout a single night. For this reason, we make a further assumption that when σ_e is less than a cutoff value q times σ_c, i.e.,

$\sigma_e < q\sigma_c$, we regard the global change as not being significant during this night, and α_e from the Beer's fitting for this night is reliable. Only then do we use these nights to make the fit in order to determine a and b.

In Table 2, we list the fitting results, a, b, σ (the standard deviation of the fit), σ_a and σ_b (the fitting errors of a and b respectively) for various cutoff values, $q = 1.0, 1.2, 1.5, 2.0, 2.5$.

We can see from Table 2 that for $q < 2.0$, the fitting results are consistent with each other. In general, the absolute value of α_e is larger than that of α_c by more than 0.01, or about 10%. That is, using $\alpha_c \sim 0.1$ and Table 2, we have $\alpha_e \sim 1.2 \times \alpha_c - 0.01 \sim 0.11$. Note that we do not distinguish among the α_e from different fiducial patches, because there is no reason for us to believe that the α_e^i should be different from one another (also see Figure 7c). As a matter of fact, we have tried to scale α_e^i to α_c separately, and the resulting fitting parameters a and b do not differ for different patches. In the subsequent analysis, we employ the scaling parameters at $q = 1.2$ in Equation (19) to obtain α_e from α_c for nights when $\sigma_e > 1.2\sigma_c$. Then, we use α_e to fit out the atmospheric attenuation, so that we can determine the true earthshine signal. After applying this correction, a direct result is that while the average of the [A*] is not altered, for some nights their appreciable, original deviations from the average, at comparable lunar phase, is greatly reduced. For those same nights the calculated α_e yields a slightly poorer fit to the data than would a direct fitting to Beer's law. The cost of this latter fitting was to force some of the earthshine signal into the atmospheric extinction coefficient, yielding an erroneous extrapoltation to zero airmass.

4.3. Measuring the Transmission of the Bright Side Filter

A precise determination of the earth's reflectance from observing the moon depends on an accurate measurement of the ratio of the true earthshine intensity to the true moonshine intensity. This determination is complicated by the fact that the moonshine is so bright that when we measure it, we must use a blocking filter (see Figure 3) that reduces the intensity of the moonshine by about 99%. The reduction enables us to have a reasonably long exposure time (of order a few

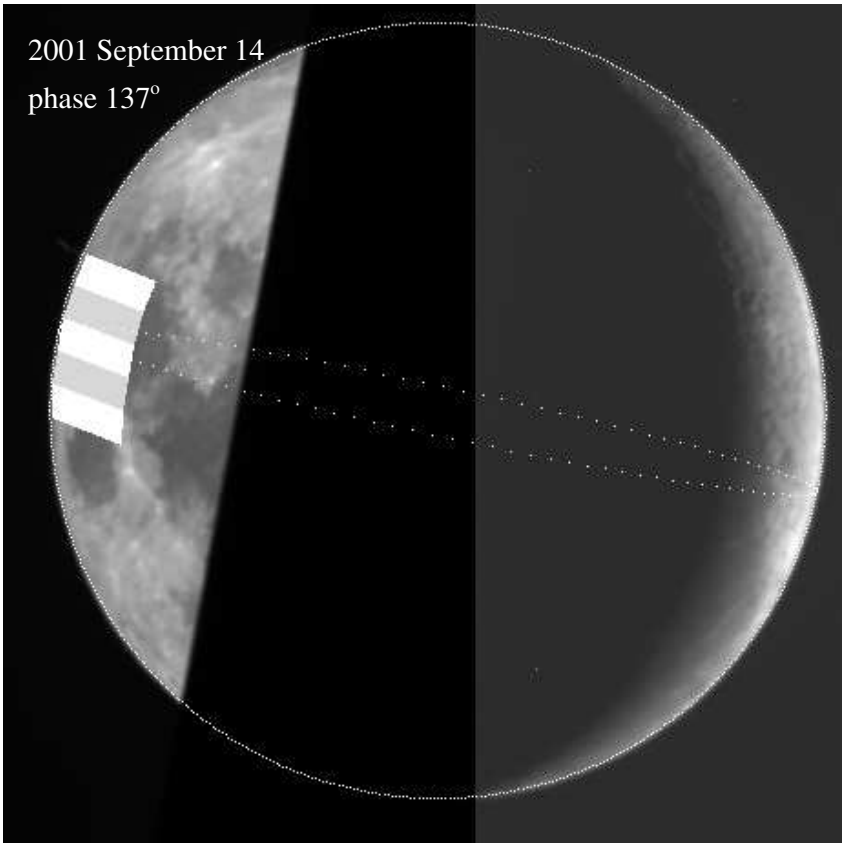

Fig. 8.— Image of the earthshine on the night of September 14, 2001 shown is one without the moonshine blocking filter. The bright, rectangular patch indicates the area of five strips used to compare the earthshine intensity with and without the moonshine blocking filter, so as to determine the transmission of the moonshine blocking filter. To allow long exposures of the earthshine, when the moonshine filter is not in place, on September 14th, the ES filter *and* a strong tertiary blocking filter were used to eliminate the crescent (as well as three-quarters of the moon). Hence the sharp terminator for the earthshine. The lunar phase was 137° that night and for perspective the crescent is restored on the right-hand side of the image.

100 ms) compared to the shortest possible exposure time of the camera (10 ms). When we observe the earthshine, the moonshine or BS filter flips out and the strong, blocking ES filter flips in to prevent camera blooming. Thus, to know the true ratio of the earthshine to moonshine intensity, we must also precisely determine the transmission of the moonshine blocking filter at the point through which the moonlight passes. This fact became abundantly clear after October 13, 2000 when the original filter broke, and was replaced by one that was comparable in the lab tests for the transmission over the whole filter. Initially, we assumed that the transmission of the new filter was the same as the old one. However, we found that the observed moonshine intensity noticeably increased indicating that the new filter has a significantly larger transmission than the old filter.

In the observations, the moonshine blocking filter is placed in a fixed position in the pupil plane covering the entire lunar image, so that the light always passes through the same point on the filter. This is important because there is some point-to-point variation in the transmission of the filter. In our effort to precisely determine the transmissions of the old and new filters at the pupil point of the lunar image, we employed identical approaches for both of the filters. To measure the transmission of the old filter, we re-analyzed thirty nights of moonshine and earthshine data that we had in-hand for nights near the new moon - where the earthshine signal is most intense. To illustrate the re-analysis procedure, one can look at Figure 8 for guidance. For that night, we measured the total earthshine intensity in five parallel strips, somewhat wider than the fiducial patches and runnning from the earthshine fiducal points toward the moonshine crescent. In that figure, the five strips are shown together as a striped, bright four-cornered patch. Each stripe in the bright patch runs from the edge of the moon and is 5° wide in latitude and 30° long in longtitude. That way, each strip would have a statistically significant number of counts in the earthshine region, even for the relatively short exposure times of a few hundred milliseconds, used on other nights, for each data point with the blocking filter in place (but without the much stronger ES filter in place). For the night in the figure, we also completely blocked the crescent with a tertiary filter, allowing much longer exposure times (of order a few minutes). The lunar phase in Figure 8 is 137°, large magnitude phase angles are chosen so that the earthshine is the brightest, while the stray light the smallest. For one typical night, the result of the re-analysis is

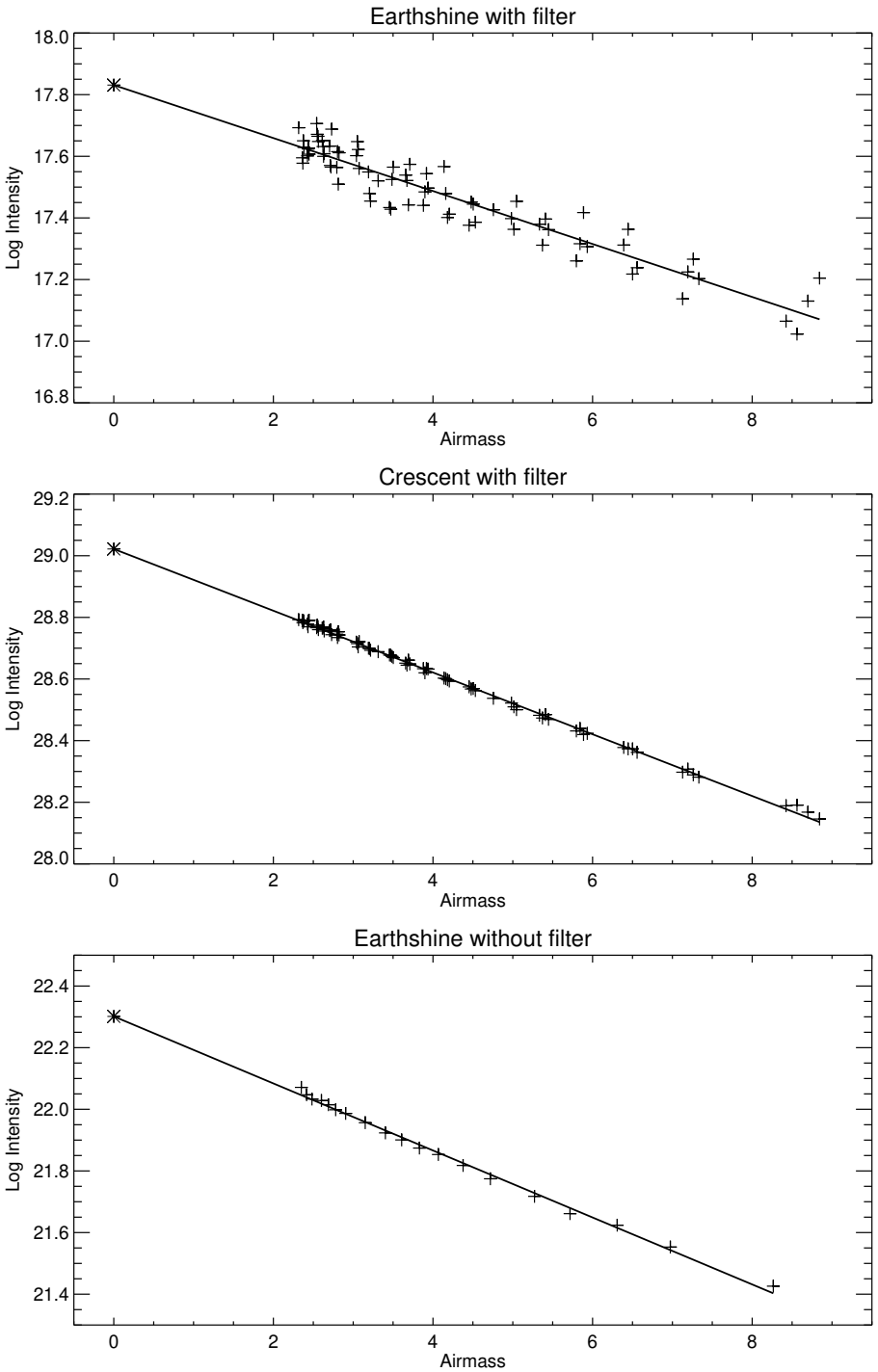

Fig. 9.— The upper panel shows the observed, filter-blocked earthshine intensity as a function of airmass on February 1, 2000. Each "+" sign in that panel represents the intensity of one stripe. Thus, at each airmass point for which there were data, one sees five point clusters. The linear fit to the data has been extrapolated to zero airmass with that result being indicated by the asterisk, which is the left-most mark on the fit. The lower panel shows the same type of data, but without the filter. The ratio of the two intensities, for that night, extrapolated to zero airmass, and corrected for the small effect of stray light, implies a blocking filter transmission of 0.0114 ± 0.0005. The lunar phase that night was $+134°$.

shown in Figure 9. The ratio of the earthshine to moonshine intensity extrapolated to zero airmass, and corrected for the small effect of stray light, (as described in §4.1), yields a transmission of 0.0114±0.005 for that night. The mean transmission for all thirty nights is 0.0113±0.0006 for the old filter. Implicit in this approach to determining the broadband transmission of the filter is the reasonable assumption that the spectrum of the earthshine and moonshine are roughly the same. They do not have to be identical because the transmission curve is flat over visible wavelengths. Most of the noise in the result arises from the short exposure time for the blocking-filter-covered observations. The 0.0113±0.0006 is quite close to Schott's quoted value of 0.0115 for the whole filter.

For the new filter, we have re-analyzed twelve nights of data in the same way and find a transmission of 0.0128±0.0004 for the pupil point, whereas the reported average across the filter is 0.0114. The latter transmission is nearly identical to that of the old filter, but quite far from 0.0128±0.0004. The larger transmission at the pupil point accounts for the apparent rise in moonshine intensity after October 13, 2000. As a cross-check of the transmission of the new filter, on the near moon night of September 14, 2001 (lunar phase of 137°), we masked the crescent (a tertiary filter added on top of the ES filter) and allowed for exposures of several minutes when the moonshine blocking filter was not in place. This alternative approach yielded a transmission of 0.0123±0.0003, which is closely consistent with the result for the other twelve nights as determined from the first method. In this latter approach, there is a trade-off between a long enough exposure time to be far above the camera's noise level and a short enough exposure to ensure that there are a enough points from which to obtain a reliable fit to Beer's law on the relatively short observing periods for nights with large magnitude lunar phases. With the latter approach, the data are much further above the camera's noise level than with the former method. The agreement between the results from two approaches gives us confidence that even with the relatvely shorter exposures in the first method, our determination of blocking filter transmission is reliable.

5. Lunar Phase Function

The lunar phase function is defined (see §2) as the relative change in moonshine intensity as a function of the phase of the moon. It is measured from the readout intensity from each of the fixed fiducial patches (five on the Crisium side and five on the Grimaldi side) used throughout the observations, after carrying out,step-by-step, each of the corrections described above in measuring the moonshine intensity. When the relative, observed intensity readout is plotted against the lunar phase for all nights, the data are quite scattered around the average curve. This is illustrated in (Figure 10a) for the Crisium and Grimaldi pair used in Goode et al. (2001). This Figure and that pair are analyzed in detail in this section. Results for all pairs are presented later in this section. On the face of it, this large scatter in Figure 10a would seem to preclude a precise determination of the earth's albedo from measuring the earthshine. However, most of the scatter is not due to unknown or random sources of noise, but rather known physical effects for which one can systematically account, and then remove. There are several steps of calibration that are necessary before we have the true lunar phase function. The results of the corrections are shown, one step at a time, in the four panels of Figure 10. The bottom panel reveals a precise lunar phase function (HOW PRECISE), which give us real confidence that observing the earthshine can yield a precise reflectance for the earth.

5.1. Atmospheric Correction

The nightly fits of the moonshine intensity to Beer's law are quite good, and so the extrapolation to zero airmass would seem quite reliable. However, there is an appreciable change in our lunar phase function (see Figure 10a), for the same phase, from month-to-month. As we shall see, the prime cause of this is that, even after extrapolation to zero airmass, the resultant intensity is subject to changes in the local atmospheric conditions. It seems that the local atmosphere is not a uniform plane, parallel gas, but rather we have something more like a canopy superposed on a plane parallel atmosphere. The canopy mutes the intensity by the same amount

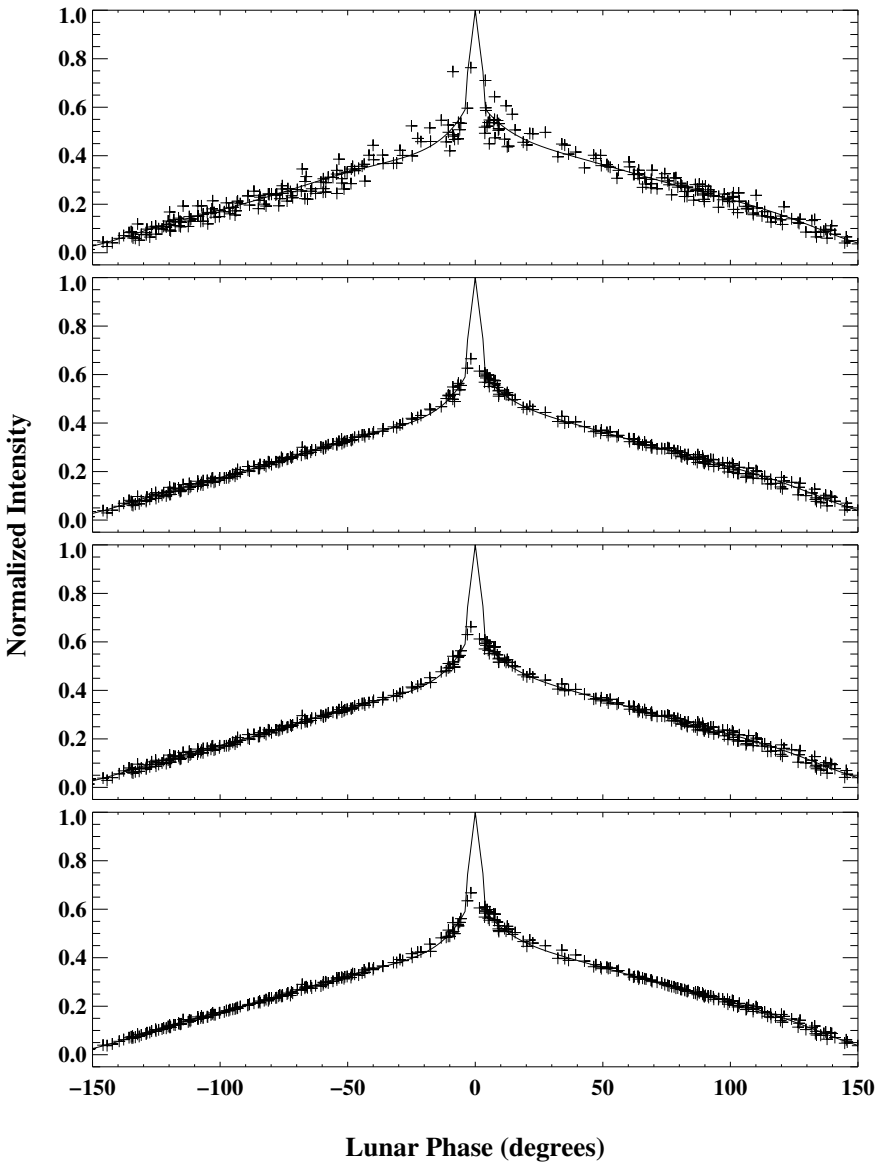

Fig. 10.— The top panel show the apparent, relative lunar phase function from the raw data, for which there are points down to 2°. The function is made relative by normalizing it to unity at phase angle 0°, which means that the ratio of the true right and left branch intensities yields the ratio of the geometrical albedoes between Crisium and Grimaldi. The peak near small phase angles represents the opposition effect. Data from a total eclipse are used to connect the positive and negative phase branches of the lunar phase function. No eclipse data are shown in this figure. The second panel from the top shows the result after including correction for the local atmospheric effects using the lunar crescent as a guide star. The third panel also includes the correction for lunar declination. The fourth panel includes the correction for lunar libration. The fit shown in each panel is the final one resulting from all of the corrections described in §5.

for all airmasses, and therefore its effect remains after extrapolation. Because of this, there is a deviation in the intensity measured from the same fiducial patch at the same lunar phase, but on different nights (that is, successive lunar cycles). To solve this problem, we employed the common practice of nighttime observers doing absolute photometry who use standard stars to account for the muting. We have found that the crescent of the moon is our best standard "star". That is, we correct from night-to-night variations using the correlation between the change of the moonshine intensity and the crescent intensity.

In the extrapolation to zero airmass, we use a fifth degree weighted polynomial fit for both the fiducial patch intensity and the average crescent intensity over the area of the bright portion as the way to determine the average of the intensity at each lunar phase. In removing the canopy effect, we give double weight to nights for which the lunar phase is less than $\pm 5^{\circ}$. We do this because of the pronounced opposition effect that gives a sharp increase in the moonshine intensity when lunar phase approaches zero degrees (see §5.4). The deviation of the measured intensity at each data point from the fitting curve, see Figure 10, for the lunar phase function, in both the moonshine case and the crescent case are obtained, and the cross correlation between these deviations is calculated. For the morning observations, for which the lunar phase is positive, we get a cross correlation of 0.73, and for the evening when the lunar phase is negative, we obtain a quite similar value of 0.77 (Figure 11). The relative correlations are determined from a simple least-square linear fit between the moonshine deviation and crescent deviation using

$$\frac{I_i - \bar{I}_i}{\bar{I}_i} = a_0 \times \frac{C_i - \bar{C}_i}{\bar{C}_i} + b_0 + \sigma_i, \tag{20}$$

where I_i is the observed fiducial patch intensity, C_i is the crescent intensity, $\bar{I}_i$ and $\bar{C}_i$ are the average fiducial patch intensity and crescent intensity, respectively, at the same lunar phase, and σ_i is the scatter about the linear least-squares fit. Note that throughout this section $\bar{I}_i$ is the solid line in Figure 10, which was derived by interating the steps described in §5.1-5.3. The coefficients a_0 and b_0 are derived from the least square fitting of Equation (20). From Figure 11, it is clear that a_0 is close to unity (morning/Grimali:0.81±0.08 and evening/Crisium:0.74±0.07), while the respective b_0's are essentially zero – 0.002 and 0.001 – more than two orders of magnitude smaller

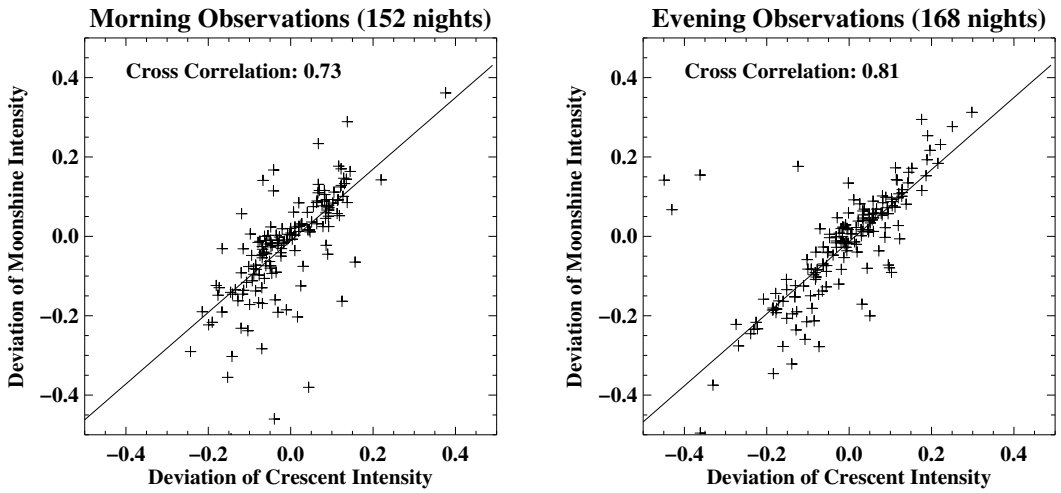

Fig. 11.— The deviation of the moonshine fiducial patch intensity from average against the deviation of the overall intensity of the crescent. Left: data points from morning observations of Grimaldi; right: data points from evening observations of Crisium. The solid lines in each panel show the linear fit to each cluster of points.

than a_0. Therefore, we determine the correct, relative zero airmass intensity, I_i', by removing the canopy effect by subtracting the linear term in Equation (20) from the earthshine data, i.e.,

$$I_i' = I_i - a_0 \times \bar{I}_i \times \frac{C_i - \bar{C}_i}{\bar{C}_i} \tag{21}$$

The scattering among the datapoints is much reduced after this correction (Figure 10b). This correction is of comparable significance for the evening data (lunar phase < 0) and the morning data (lunar phase > 0), as the comparable cross-correlations imply.

5.2. Declination Correction

The second step in correcting the deficiencies in the apparent lunar phase function is to remove variations arising from the systematic change of relative position of the moon to the plane of the earth's orbit about the sun. The difference in right ascension between the sun and the moon (hereafter, the "relative right ascension") changes from 180 to -180°, which essentially determines

the lunar phase, defined as the angle from between the moon-earth line and the sun-moon line, see Figure 1. However, there is a clear ambiguity in the lunar phase angle that makes the apparent lunar phase function multi-valued. In detail, the difference in the declination between the sun and the moon (hereafter "relative declination") changes as well, since the orbital plane of the moon around earth is inclined to that of the earth around the sun. Toward the full moon, the relative declination also becomes important in determining the lunar phase. Then, at the same lunar phase, but on different nights (that is, different months), the position of the moon may be different, and this difference alters the readout intensity of the fiducial patches. To correct for this effect, for a given lunar phase near the full moon, we choose a standard position of the moon and normalize the readout intensity of different positions to this standard position. The standard position is the one for which the relative declination is zero, i.e., the moon is in the plane of ecliptic, and the lunar phase is equal to the relative right ascension, i.e., a total lunar eclipse. The normalization is made as follows:

$$I_i - \bar{I}_i = a_1(P_i - P_{i,RA}) + b_1 D_i + c_1 + \sigma_i, \tag{22}$$

where I_i is the observed intensity, $\bar{I}_i$ is the average intensity at the same lunar phase as I_i, obtained from the fifth degree polynomial fitting in Figure 10, $(P_i - P_{i,RA})$ is the difference between the lunar phase and the relative right ascension, D_i is the relative declination, and a_1, b_1, and c_1 are fitting parameters which are determined from the least square fitting using all the observed intensities. The fitted parameters, a_1 (morning/Grimaldi: -0.003±0.002 and evening/Crisium:3.4e-5±7.0e-5), b_1 (morning/Grimaldi: -0.4.7e-5±0.0002 and evening/Crisium:0.0007±0.0002) and c_1 (morning/Grimaldi: 0.009±0.008 and evening/Crisium: 0.009±0.009) are all quite small. The normalized intensity, I_i', is derived by removing the relative right ascension and declination:

$$I_i' = I_i - [a_1(P_i - P_{i,RA}) + b_1 D_i]. \tag{23}$$

The c_1 term is regarded as part of the errors (σ_i).

This correction is only made for lunar phase between -15 and +15 degree since the effect of the relative position of the moon is only important around the full moon. However, after this

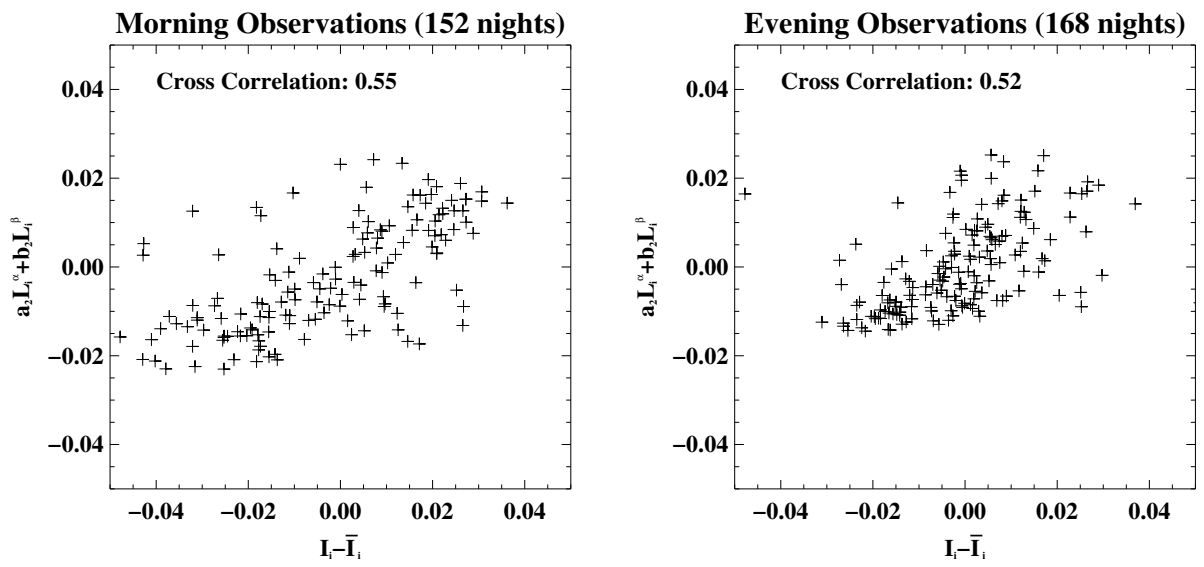

Fig. 12.— The deviation of the moonshine fiducial patch intensity (after the first and second step corrections) from average against the deviation as a fitting result from Equation (24). Left: data points from morning observations; right: data points from evening observations.

correction, the modest improvement reveals barely apparent changes in the data points, compare left branches of Figures 10b and c) for small phase angles.

5.3. Libration Correction

The third step in rectifying the apparent lunar phase function requires removing the effects of latitudinal and longitudinal lunar libration. Since the orbit of the moon around the earth is not in the equatorial plane of the moon, a terrestrial observer alternatively sees the north pole and south pole of the moon during each orbit. This is the latitudinal libration. Further, the slightly elliptical orbit of the moon has the consequence that the moon moves slower at apogee than at perigee, and therefore is seen to be wobbling around its axis of rotation. This is longitudinal libration. An additional, very small dynamical libration arises because the moon is prolate, and its pointing wanders. The dynamical libration adds to both the latitudinal and longitudinal librations. These librations allow us to see about 60% of the moon's surface. As a result of both kinds of libration,

for different cycles of the lunar orbit, even at the same lunar phase, we would expect changes in the positions of the fiducial patches on the lunar disk. The readout intensity thus changes as a function of the geometric position of the fiducial patches on the lunar disk. The longitudinal and latitudinal librations cause the apparent lunar phase function to be multi-valued. To first order, we derived a description of the deviation of the observed intensity from the averaged intensity as a linear function of the longitudinal and latitudinal librations, which goes as:

$$I_i - \bar{I}_i = a_2 L_i^{\alpha} + b_2 L_i^{\beta} + c_2 + \sigma_i, \tag{24}$$

where the $I_i - \bar{I}_i$ are the deviations of each night from the mean, and where L_i^{α} is the longitudinal libration and L_i^{β} is the latitudinal libration. Here, L_i^{α} and L_i^{β} really measure the position of the lunar pole in the sky with respect to its mean position, so that all the kinds of libration are taken into account. From a least squares fit, we obtain the coefficients a_2 (morning/Grimaldi: 0.0019±0.0004 and evening/Crisium: -0.0018±0.0004) and b_2 (morning/Grimaldi: 4.2e-5±0.0003 and evening/Crisium: -0.0003±0.0004), while c_2 is 1-2 orders of magnitude smaller than a_2. Since the magnitude of the a_2's are about an order of magnitude greater than the b_2's, the longitudinal libration is more significant than the latitudinal libration. Figure 12 shows the result of fit, and, in particular, that the fit describes the data, in that it can be seen that the observed scattering at this step is mainly accounted for by the libration. For the determination of Figure 12, we used 152 mornings and 168 evenings, and the correlation between the fit and the data is 0.44/0.52 respectively. Using the parameters from the fit, we then normalize the intensities at all lunar phases to the case of zero libration with the equation:

$$I_i' = I_i - (a_2 L_i^{\alpha} + b_2 L_i^{\beta}) \tag{25}$$

To check the validity of the libration correction, we performed the the libration correction again – but doing it before performing the atmospheric correction described in §5.1. We next performed the atmospheric correction (which still dominates) and the declination correction. At that point, we performed the libration correction again, and we found that $I_i - \bar{I}_i$ does not have a significant correlation with the libration. In particular, the parameters from the linear fit of

Equation (24) are reduced by an order of magnitude. This test not only confirms the validity of the libration correction performed above, but also guarantees that the three-step corrections can be performed in any order.

The lunar phase function for each of the ten fiducial patches were produced from a fifth degree weighted polynomial fit to the corrected data. The same algorithm was used for all the steps above, as the means of deriving the average of the intensities for all lunar phases. After each step of correction, the standard deviation of the fit is deduced from orginally 0.05/0.05 (evening/morning) to eventually 0.01/0.01, with the phase function normalized to unity. A restricted regularized fitting is performed as well, which parameterizes the intensities at 181 bins (corresponding to lunar phase 0° to 180°). These 181 parameters from the fitting describe the lunar phase function, in that the intensity of any lunar phase is the linear interpolation between the values at the two grids into which the lunar phase falls. Note that since there are no data points beyond 150° degrees, the phase function fit beyond this range is not reliable. Similarly, there are not enough data points within ±5°, and so, in the next section we will describe how we determined the fitted peak in Figure 10 by treating opposition effect at small phase angles (near the full moon). From the third-step fit, the estimated error of the mean is at the level of 0.5%, thus, we have measured the lunar phase to 0.5%.

5.4. Opposition Effect

To this point, the lunar phase function is incomplete because it is not absolutely calibrated, and we have not determined its functional form for the smallest phase angles. To do these, we need to know the phase function for small phase angles, and that means that the final lunar phase function for each fiducial patch needs to be normalized to the full moon opposition peak. In reality, the moon is not observable at zero lunar phase because the shadow of the earth would occult the moon, as the earths shadow occupies about ±0.8°. So far, the smallest phase we have reached is ±1.0° on the night of November 29, 1993, when a total lunar eclipse occurred over Big Bear. On that night, the sky was clear and stable throughout, and observations were made both

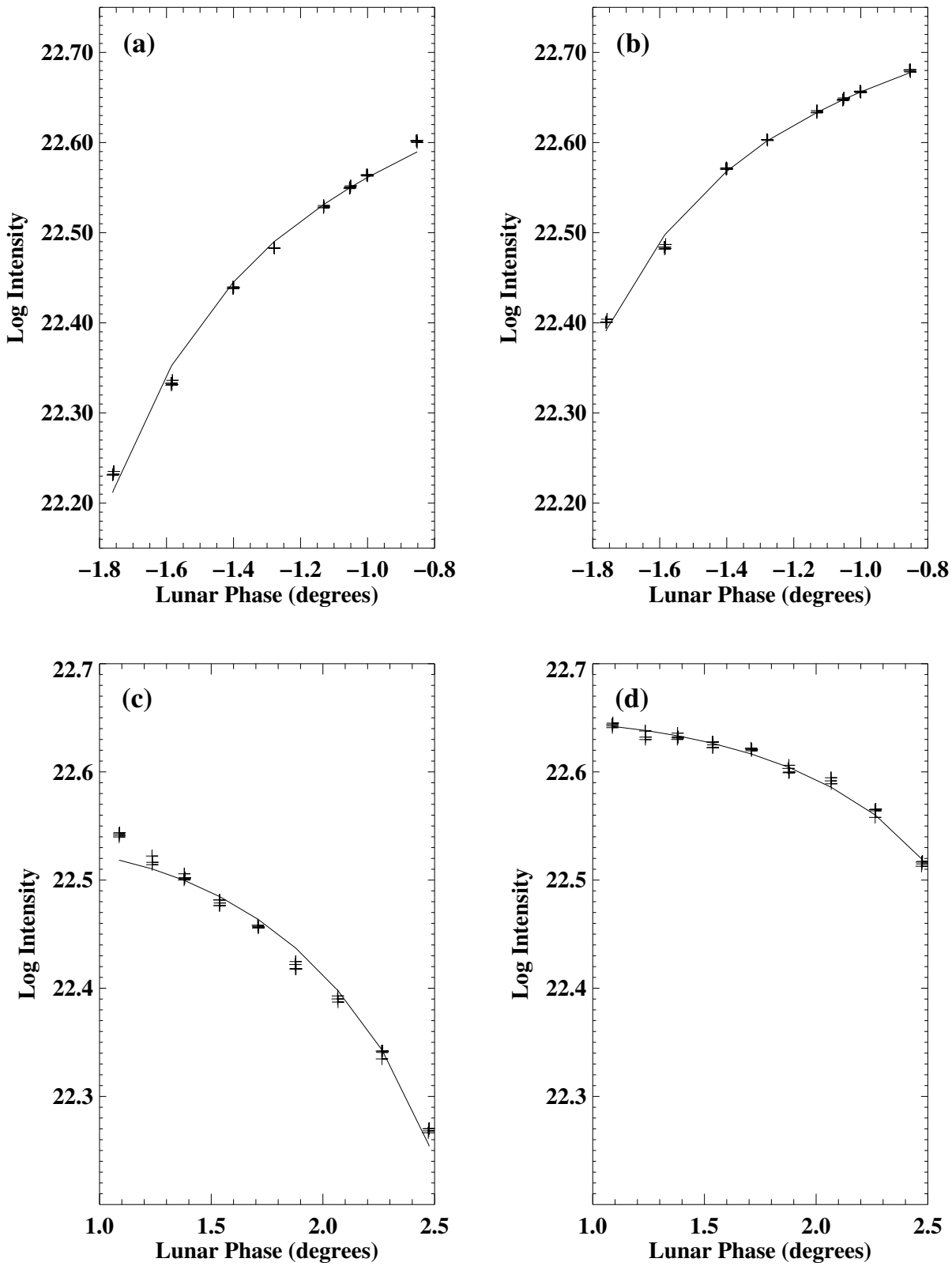

Fig. 13.— Fit of lunar eclipse data obtained on November 29, 1993. (a) Beer's law fit of the Crisium side (Equation 18); (b) Composite Beer's law plus opposition effect fit on the Crisium side (Equation 26); (c) same as (a) on the Grimaldi side; (d) same as (b) on the Grimaldi side.

before and after the total eclipse, covering lunar phase angles of magnitude ranging between about 1° and 2°, which offers a unique dataset to investigate the slope of the opposition surge effect for all fiducial patches on both the Grimaldi and the Crisium sides.

The images taken during the eclipse were processed and the intensities of the fiducial patches were read out as described in Section 4.1. The atmospheric attenuation has to be corrected to obtain the real moonshine intensity. However, throughout the night, the evolution of the moonshine intensity was controlled not solely by the changing airmass, but also by the changing phase angle. This latter effect is appreciable because of the strong opposition effect at small lunar phase angles. As a result, the shape of the intensity evolution for the two patches deviates strongly from Beer's law (see Figure 13a and c). Thus, Equation (18) can no longer produce a reasonable fit.

We developed a simple solution to this problem under the reasonable assumption that the opposition effect is linear for very small phase angles, say, from 0 to 5°. During the eclipse, the phase angle changes by less than two degrees for either the Crisium branch or the Grimaldi branch. To determine the slope of the opposition peak for each of the ten fiducial patches, we represent the observed intensity by:

$$I_i = I_0 \times (1 - \gamma|P_i|) \times e^{-\alpha z_i}, \tag{26}$$

where I_i is the observed intensity at phase angle $|P_i|$ (in degrees) and airmass z_i. In contrast to Equation (18), I_0 describes the intensity at both zero airmass and zero phase angle. The second term on the right hand side describes the linear increase of the phase function as the lunar phase goes to zero. The last term describes the exponential atmospheric attenuation, i.e., Beer's law, where α is the atmospheric absorption coefficient for the moonshine.

In applying Equation (26), we used the observed I_i, after correcting for libration (see §5.3), at lunar phase P_i and airmass z_i in Equation (26)above, and made a least-square non-linear fit to obtain α, I_0, and the linear opposition effect coefficient, γ. The fit was made for all ten fiducial patches. We did not correct for the declination because the moon is in total eclipse, and that

correction should be quite small. We collected about 40 data points for the fit on each side of the moon, i.e., before and after totality, and the standard deviation of the final fit is at the level of 0.5%. Figure 13b and d reveal the improvement in fitting results for one pair of fiducial patches using Equation (26) instead of Equation (18). The improvement is typical of that for all ten patches. From Figure 13, it is also clear that Equation (26) accurately describes the composite effect of the opposition surge and Beer's law. The fitted opposition peak slope parameter, γ, was then used to normalize the phase function for each of the fiducial patches. Figure 10 shows an example of the final lunar phase function normalized to the opposition peak. Of course, each fiducial patch has its own lunar phase function. In detail, for lunar phase of 5° in Figure 10, we used the slope, γ, determined for very small angles to extrapolate to the intensity at zero lunar phase from that at 5°, i.e., $I(0) = \frac{I(5)}{1-\gamma\times 5}$. Then, we normalized that branch of the phase function its γ and $I(0)$=1 to fix $I(5)$. Combining our knowledge of $I(5)$ with the relative phase function indicated by the +'s in Figure 10, we obtain the right branch of that figure. The normalization removes the ratio of the geometrical albedoes between the two patches, which is restored in Equation (27).

In Table 3, we list the values of the derived opposition coefficients, γ, for all ten fiducial patches. The value of γ for all fiducial patches is approximately 0.08 per degree, indicating that when lunar phase changes from six degrees to zero degrees (full moon), the intensity doubles. This is the well-known opposition surge which has not been quantitatively determined previously. The formal error in the determination of γ is about 0.5%.

The parameter I_0 is also used to obtain the ratio of the earthshine patch reflectivity to the moonshine patch reflectivity p_a/p_b. Table 4 gives the ratios determined between the each of the five Crisium patch reflectivities to the each of the Grimaldi patch reflectivities:

In Figure 14, we compare Danjon's fitted phase function to our corrected one. Danjon used slightly different fiducial patches, but that is not the source of differences. Rather, it is the opposition surge which was unknown in Danjon's time. There is a clear offset in the Danjon phase function which would yield uniformly higher albedos than the true phase function. For our

Table 2: α_e against α_c

q	a	b	σ	σ_a	σ_b
1.0	1.1886	-0.0073	0.0099	0.0183	0.0023
1.2	1.1830	-0.0061	0.0128	0.0170	0.0023
1.5	1.1813	-0.0051	0.0132	0.0172	0.0023
1.8	1.1881	-0.0050	0.0140	0.0171	0.0023
2.0	1.2281	-0.0095	0.0167	0.0169	0.0023
2.5	1.2222	-0.0124	0.0164	0.0161	0.0022

Table 3: Opposition Effect

Patch	1	2	3	4	5
Grimaldi side	0.084	0.078	0.083	0.079	0.083
Crisium side	0.086	0.079	0.076	0.083	0.083

Table 4: $\frac{p_a}{p_b}$ (Crisium Side/Grimaldi Side)

Patch	1	2	3	4	5
6	1.121	1.130	1.141	1.086	1.109
7	1.041	1.050	1.060	1.009	1.030
8	0.919	0.926	0.935	0.890	0.909
9	0.983	0.991	1.001	0.953	0.972
10	0.989	0.996	1.006	0.958	0.978

phase function, we have eliminated this erroneous overestimate, by about ∼20%, of the earth's reflectance introduced by the phase function in earlier incarnations of earthshine studies, like those of Danjon.

6. Determination of the Earth's Albedo

The effective albedo is calculated from the earthshine measurement by combining equations (9) and (17):

$$A^*(\beta) = \frac{3}{2f_L}\frac{p_b f_b(\theta)}{p_a f_a(\theta_0)}\frac{I_a/T_a}{I_b/T_b}\frac{R_{em}^2}{R_e^2}, \tag{27}$$

where $\frac{I_a/T_a}{I_b/T_b}$ is the ratio of the earthshine intensity to the moonshine intensity in two opposing fiducial patches, after each is extrapolated to zero airmass. The ratio between the physical reflectivity of the two opposing fiducial patches, $\frac{p_b}{p_a}$, is determined from the lunar eclipse data taken at BBSO on November 29, 1993, as discussed in Section 5.4. The lunar phase function for the bright side, $f_b(\theta)$, is used in the formula to account for the geometrical dependence of the reflectivity of the moon, while $f_a(\theta_0)$ accounts for the fact that the earthshine is not exactly retroflected from the moon ($\theta_0 \lesssim 1^\circ$). In our analysis, θ_0 is taken as the angle between the observer's position and the mean of the sub-solar point (position on the earth's surface of the solar zenith)and the sub-lunar point (position on the earth's surface of the moon's zenith) with the apex of the angle being defined with respect to the fiducial patch under consideration, see Figure 1. We assume that the moonshine and earthshine have the same lunar phase function for each fiducial patch. Thus, we take $f_a(\theta_0)$ from the appropriate moonshine phase function. The earthshine is somewhat bluer than the moonshine because of Rayleigh scattering by the earth's atmosphere. Therefore, we have to assume that the reflection of visible light from the moon doesn't depend on wavelength, unlike the case of reflection from the earth. Since the moon has no atmosphere and the characteristic size of lunar surface material is much larger than the wavelength of visible light, the reflection of the earthshine/moonshine shold be insensitive to the wavelength of the reflected, visible light.

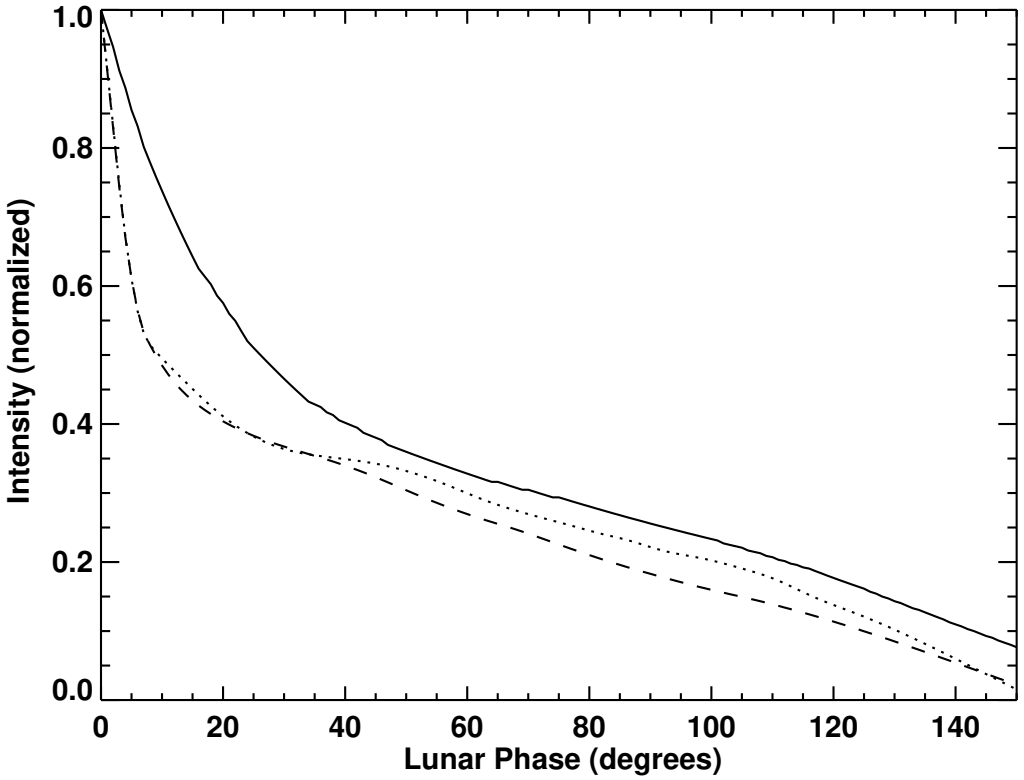

Fig. 14.— Danjon's phase function (solid line) is plotted against lunar phase. Using Figure 10d, the dashed line is our phase function for evening observations and the dotted line for morning for the fiducial patech of Figure 10.

For convenience, the measured earth's albedo is often expressed as the magnitude of the effective albedo, A* (see Equations 9 and 27), i.e.,

$$[A^*] = -2.5\log A^*. \tag{28}$$

This standard astronomical definition implies that the larger $[A^*]$ is, the smaller the albedo. Note that a 1% change in A^* corresponds to a about $0^m.01$ change in $[A^*]$.

Each night we observe 10 fiducial patches, 5 on the Crisium side, and 5 on the Grimaldi side. In principle we obtain 25 values of [A*] from the 25 combinations of the 5 pairs of fiducial patches. This gives us a way to evaluate the reliability of our measurement of [A*]. Figure 15 (a) and (b) shows the [A*] plot (morning and evening respectively) against lunar phase for all 25 datasets. It is clear that the same pattern of variation appears in all datasets, indicating that this pattern is real and not from measurement noise. We take an average of the 25 measurements of [A*] for each night as shown in Figure 15 (c), and the standard deviation of the mean in [A*] is calculated as 0.016 and 0.018 for morning and evening respectively, yielding a measurement accuracy of better than 2%. In detail, we calculated the $\sigma^2 = \frac{\Sigma_i([A^*]_i - [\overline{A^*}]_i)^2}{N-1}$, where N=5 and i=1-25.

So far, observational data have been accumulated for 30 months covering the winter of 1998-1999 through the middle of 2001 (1998 December 9 - 2001 June 30). We also have 74 nights of data from 1994 January 7 - 1995 August 4 that will be discussed in §6.2. Both the instantaneous [A*] variation during each single night, and the variation of the nightly average [A*] throughout the seasons, have been obtained and compared to the simulated results using a scene model, snow/ice cover data and satellite cloud cover data.

6.1. The Observed $[A^*]$'s during 1999-2000

Figure 15 illustrates the change of $[A^*]$ against lunar phase as determined from the nightly earthshine observations – with the morning and evening observations presented separately and combined. In the plots, each data point represents a nightly averaged $[A^*]$ value, with which we study the changes in $[A^*]$ for different nights, months and seasons. One may first note that while

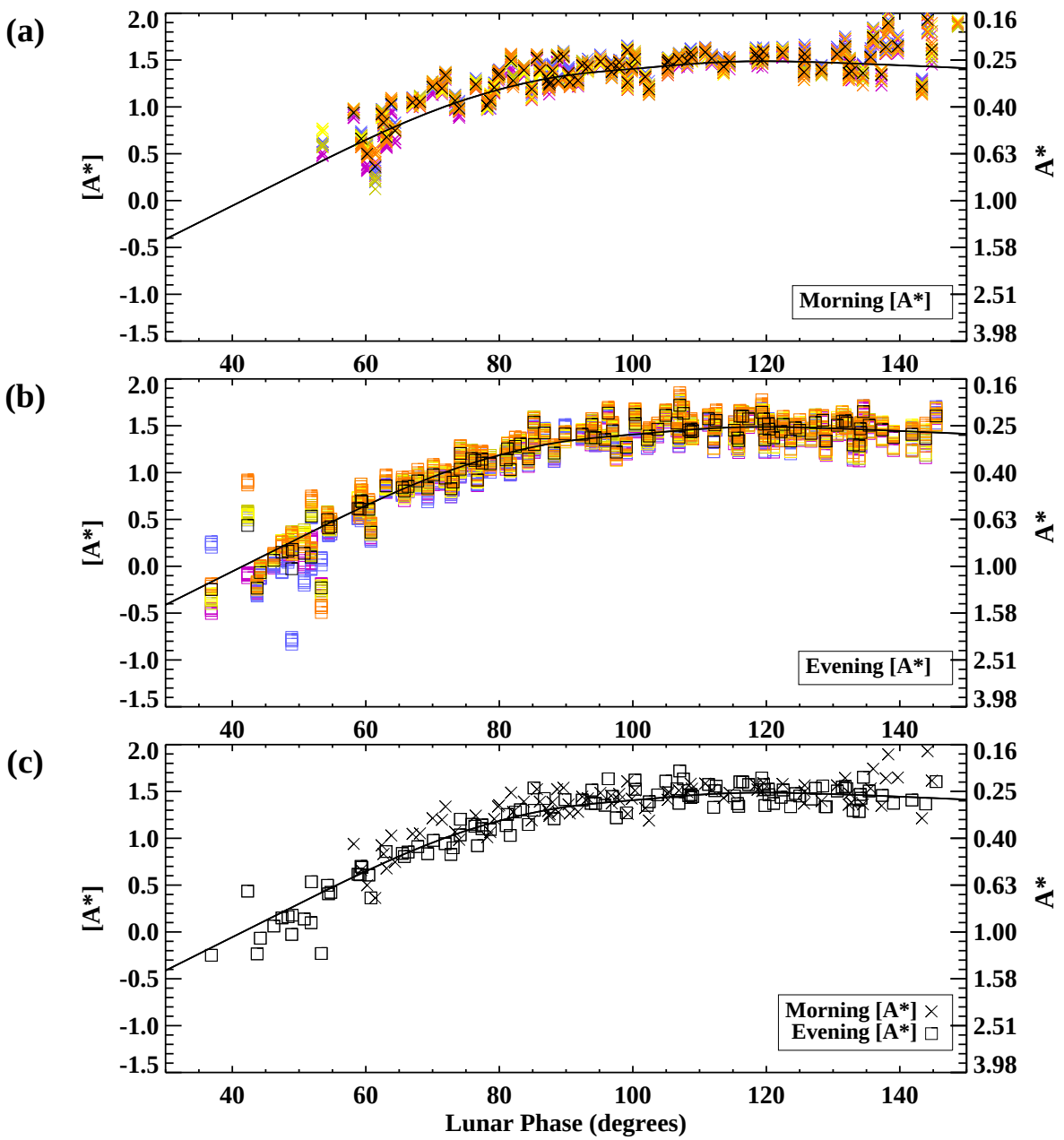

Fig. 15.— Plot of $[A^*]$ determined from 25 sets, as indicated by different colors, for (a) morning and (b) evening observations, superposed with the average of the 25 sets in black. Panel (c) gives the average of the 25 sets for each night, and for mornings and evenings, respectively. The dark solid line in all panels indicate the curve from the fit to the data in the bottom panel, as described in §7. On the righthand y-axis, we use units of A^*.

$[A^*]$ is relatively flat near the quarter moon, it sharply decreases as the full moon approaches. This decrease implies that the earth looks relatively shinier due to enhanced reflectivity at grazing angles (glint). For lunar phase magnitude much below about 40°, we presently regard the results as unreliable because of the proximity of the earthshine fiducial patches and the terminator (the transition from the moonshine to the earthshine is not sharp). Further, we do not have reliable earthshine data near the new moon (much beyond a lunar phase magnitude of about 140°) because the earthshine is visible for only a brief time near sunset or sunrise, depending on whether the moon is in its waxing or waning phase. Thus, the extrapolation to zero airmass is unreliable. For large phase angles, it is also difficult to find a fiducial patch that is confined to the moonshine.

A detailed examination of Figure 15 reveals that, with respect to the fitted mean, the $[A^*]$ determined from the local BBSO morning observations (lunar phase > 0) are not apparently distinct from those determined from the local evening observations (lunar phase < 0); i.e., the earthshine data from BBSO nights implies that the contemporaneous sunlit parts earth are equally shiny in the evening and in the morning (evening: 0.297±0.006 and evening 0.295±0.006 TRUEA?). The lack of a difference may seem somewhat surprising because the earthshine we observe in the mornings and in the evenings comes from the reflection of sunlight from different parts of the earth. In our evening observations, the earthshine is dominated by southeast Asia. In the mornings, the earthshine is dominated by Africa, Europe and the Atlantic.

Bearing in mind that a change in $[A^*]$ of $0^m.01$ corresponds to a 1% change in A^*. We observe a roughly ±5% night-to-night variation in the earthshine, A^*, even near the quarter moon where the data are most reliable. This variation is primarily associated with night-to-night changes in the cloud cover, rather than some error in the data collection/reduction process. In Figure 15, the spread about the mean is even larger, and we shall see that this is primarily associated with seasonal variations (§6.4) in the reflectance.

To better understand the influence of the earth's varying topography and cloud cover on $[A^*]$, we plot the albedo as observed throughout single nights in Figure 16. This plot comes from using Equation (27) after extrapolation to zero airmass, and inputting the proper lunar phase for each

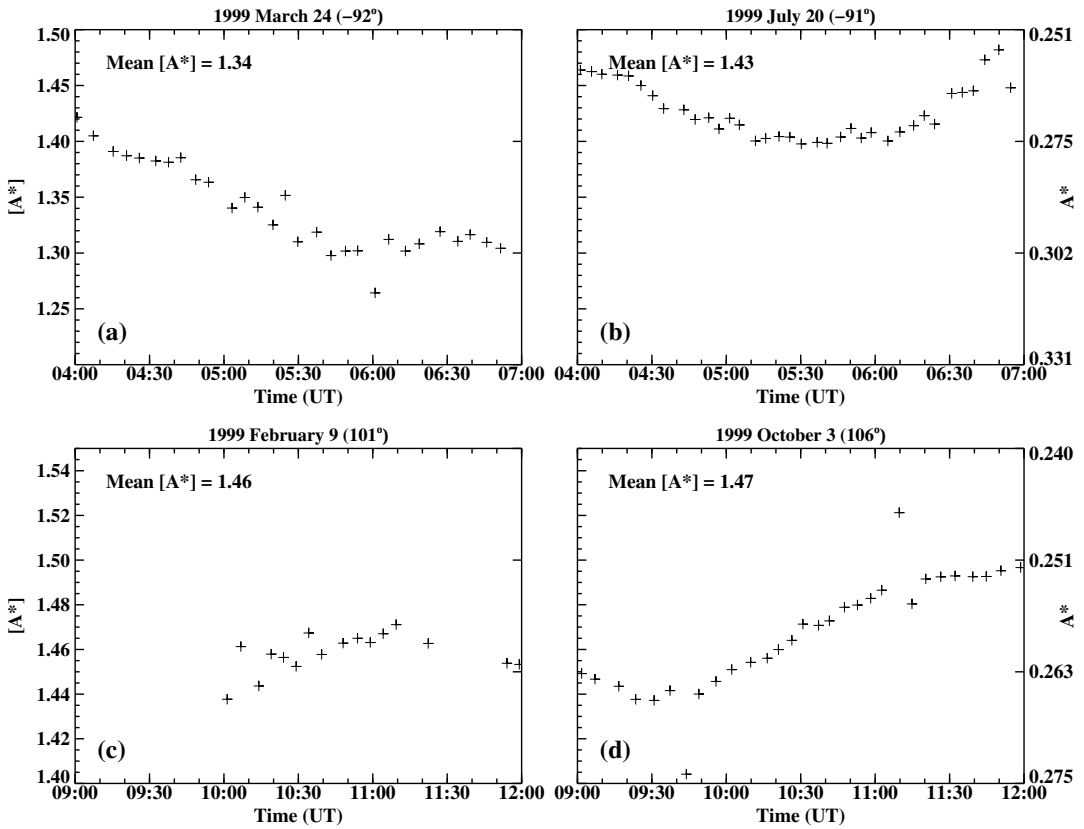

Fig. 16.— Plots of $[A^*]$ observed in the night of (a) 1999 March 24, (b) 1999 July 20, (c) 1999 February 9, and (d) 1999 October 3, against the time of observations. The right y-axis gives the result in units of A*. The values are dervied for the fiducial pair of Figure 10

observed time point. Note that the lunar phase function changes by about 1° per hour. In Figure 15, each point represents the mean of single night, as indicated in each panel of Figure 16. In Figure 16a and Figure 16b, observations of two nights with almost the same lunar phase, but from different months are compared. Both observations were made in evening at BBSO (as opposed to the early morning). They demonstrate a common tendency of a decreasing $[A^*]$, or a brighter earth, as the sun is rising over Asia, increasing the contribution from the relatively bright Asia. This causes a 5-10% change in A^* over the period of observations. Even though the temporal evolution of the points in Figure 16a and 16b closely resemble each other, the mean value of A^* in Figure 16a is 5% smaller. This difference reflects a greater Asian cloud cover on March 24 than July 20. As we shall see in §6.4, some part of the appreciable difference is due probably due to seasonal changes in cloud cover, rather than differences in the part of the world we are measuring. In Figure 16c and Figure 16d, the observations are from two mornings at similar phases of the moon, and covering comparable local times. One notices immediately, that A^* in Figure 16c and 16d are about 10% smaller that their counterparts in 16a. In Figure 16c and 16d, each panel shows an increasing $[A^*]$, or a darker earth, as time goes on. This is because the sunrise over the Atlantic is increasing the role of the darker, and less cloudy, ocean in the earthshine.

From Equation (27), one may surmise that the observational errors arising from measuring A^* from two opposing fiducial patches come from the errors in the readout intensity from the moonshine and earthshine fiducial patches, and error in the determination of lunar phase function. The ratio $\frac{p_b}{p_a}$ can be regarded as the relative normalization of the phase functions of the opposing fiducial patches. The standard deviation of the lunar phase function can be determined down to 0.5% from a co-variance calculation with a comparable uncertainty for the ratio $\frac{p_b}{p_a}$. The standard deviation of the Beer's law fitting of the moonshine for each night is taken as the error of the moonshine intensity. This gives a value of 1.1%. For the case of the earthshine, the scattering of the data is due to both the errors and the real physical changes in the terrestrial albedo. The average standard deviation from Beer's law fitting of the earthshine intensities is 1.9%. Conservatively speaking, if half the amount of such scattering comes from the real physical change in average, the error in nightly earthshine intensity measurement is about 1.0%. Adding up all

the errors and assuming they are independent, we get a nightly measurement error of nearly 2%. If one regards the measurements from different pairs as being independent, the 2% is reduced to about 1% If we combine nights to obtain, say, a seasonal average, then the total error will be smaller, but no smaller than that associated with the mean values of the various lunar phase functions and their relative normalizations. For instance, we have 216 nights of data for which the fit to Beer's Law has a standard deviation of less than 1% for the single pair of fiducial patches of Figure 10. We regard these as our "good" nights. If we calculate the standard deviation of the mean for the 95 (121) mornings (evenings) pairs, we find 0.3% (0.4%). Combining this with the uncertainty in the lunar phase, we find an error of less than 1% in the binned A^*'s. Such error bars would be weel-within the symbols of Figure 15 Of course, systematic errors are possible in the determination of the lunar phase function and the geometrical albedos, but if they are comparable to the measurement errors we can reasonably identify, they are still considerably smaller than the spread in the $[A^*]$'s the appear in, say, Figure 15.

6.2. Solar Cycle Variations in $[A^*]$?

There are many terrestrial signatures with an 11/22 year periodicity that, by default, would seem to be associated with the sun's magnetic activity cycle. Perhaps the most impressive is the demonstration of a wandering, near 11 year periodicity in the dust in Greenland ice core data going back more than 100,000 years, Ram and Stoltz (1999). With such signatures in mind, it is one of our primary goals to determine whether or not the earth's reflectance varies with solar activity. We have sufficient data to do a preliminary probe of this question. We have more than 200 nights of observations covering the two year period 1999-2000 (a time of high solar activity). We also have 72 nights of earthshine data covering 1994-1995 (a time of low solar activity). These 72 nights favor no particular season. We show these data in Figure 17 against the fit from Figure 15. The mean A^* from the earlier time is 2.5%±1.5% greater. The deviation from the same curve for the 1999-2000 data is 0.0%±0.9%. RESULT25 This suggests that the earth was 2.5%±1.8% more reflective in the earlier time which was also a time of lower solar activity.

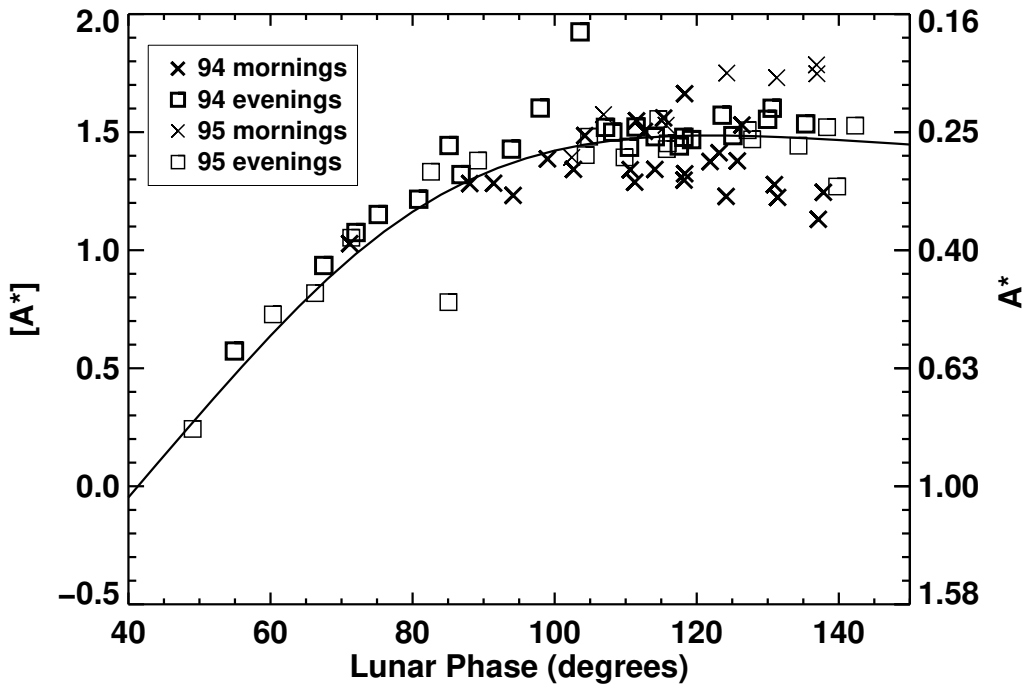

Fig. 17.— Plots of $[A^*]$ observed during 1994 and 1995. They are shown separately as morning and evening observations for each of the two years. The fit shown is that from Figure 15 which is for the 1999-2000 data.RESULT25?

The hint of a shinier, and hence cloudier earth in the earlier time of lower solar activity could be consistent with the results of Svensmark and Friis-Christensen (1997). The 2.5% larger albedo is about the same as would result from the 3-4% greater cloud cover at activity minimum for which Svensmark and Friis-Christensen argue using satellite cloud cover data from the previous solar cycle. On the other hand, if we examine our data more carefully, we find that the largest part of the discrepancy comes from 1994 morning observations. The morning observations are sensitive to South America and the Pacific just west of it. This place and time was in the midst of an El Niño event, so we cannot confidently conclude that the 2.5%±1.8% excess is a change tied to the systematic variation in solar activity. Nonetheless, suppose the difference in reflectance were tied to the cycle. What size change in the net sunlight reaching the climate system would be caused by that change in solar activity? And how would it compare to changes in the sun's irradiance that are tied to the cycle?

The net sunlight reaching the earth depends on the sun's irradiance and the earth's reflectance. It has been know for sometime that the solar irradiance is correlated with solar activity, Willson and Hudson (1991) with the irradiance being about 0.1% greater at activity maximum. The latest results covering the twenty years of satellite observations of solar irradiance are shown in Figure 18, Fröhlich (2001). It is generally agreed that a 0.1% variation over the activity cycle is too small to be climatologically significant (see Lean for a review). What about the earth's reflectance? Taking the aforementioned 2.5% change as being real, how significant would that be? To see the relative roles of varying solar irradiance and the varying reflectivity of the earth in the change in the net input of sunlight to the climate system between a time of high solar activity (1999-2000) and one of low activity (1994-1995), we use Equation (1) under the assumption that the A's scale with the A^*'s to find that

$$\frac{\delta P_{\rm in}}{P_{\rm in}} = \frac{\delta C}{C} - \frac{\delta A^*}{1-A}, \tag{29}$$

so that $\frac{\delta C}{C} \sim 0.001$. Our observations of the earthshine take the ratio of the earthshine to moonshine, so we are insensitive variations of the solar irradiance. The 2.5%±1.8% change in reflectance translates to $\frac{-\delta A^*}{1-A^*} \sim 0.011 \pm 0.007$. The two effects are in phase and contribute to

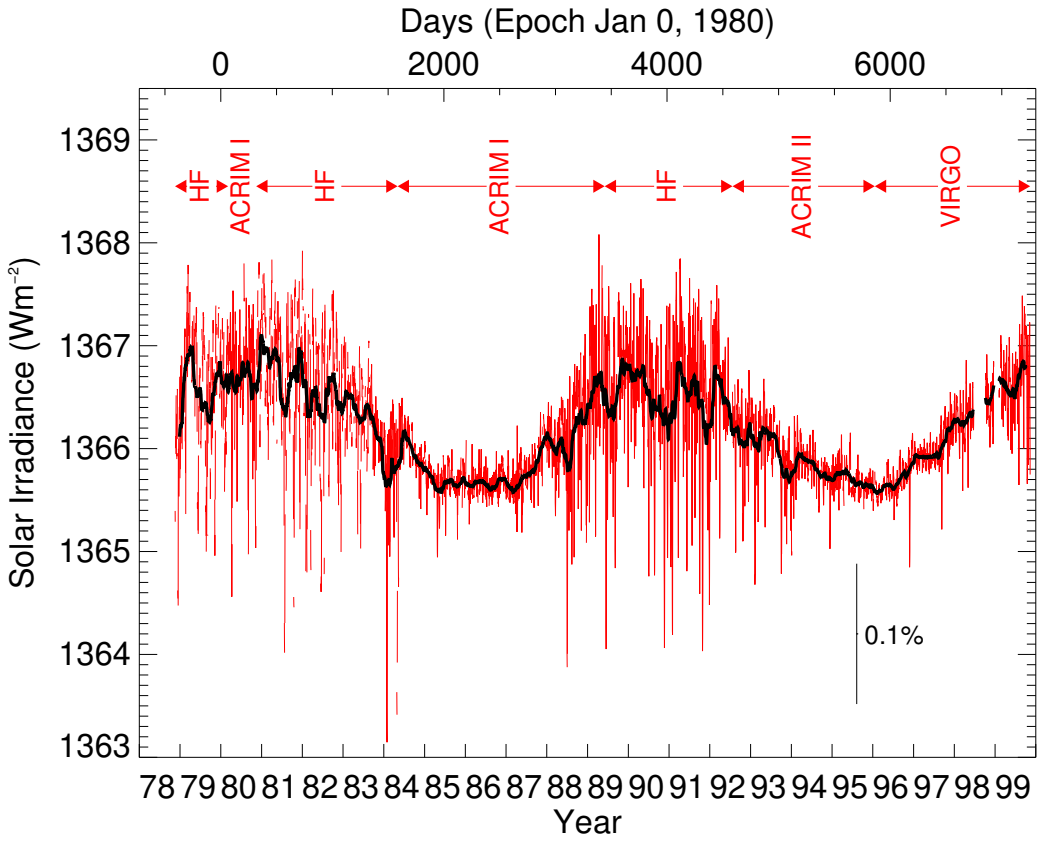

Fig. 18.— Plot of the solar irradiance vs. time

a greater power going into the climate system at activity maximum. However, the effect of the albedo is about an order of magnitude greater. Still, our result is only significant at the 1.5σ level, and whether the earth's reflectance varies with the solar cycle is a matter of controversy, Svensmark and Friis-Christensen (1997) and Goode et al. (2001).

Currently, we are taking data at about five the rate we did in 1994-1995. We are also building a three-station global network which would triple our current data rate. Thus, during the declining phase of the current activity cycle, we should be able to precisely determine the correlation between the earth's reflectance and evolving solar magnetic activity.

6.3. Modeling the Observations

For the simulations, we have the information to determine a Bond albedo by using scene models of the earth, and adding cloud cover data from satellites and snow/ice cover from models. The Bond albedo is given in terms of the albedo of each element of the earth's surface by,

$$A = \frac{1}{\pi R_e^2} \int d^2R(\hat{R} \cdot \hat{S})a, \tag{30}$$

where d^2R is an element of the earth's surface, $\hat{R}$ is a unit vector pointing toward the local zenith, and $\hat{S}$ is a unit vector pointing toward the sun. The albedo of each surface element, a, depends on the surface type, cloud and snow/ice cover and solar zenith angle. The integral is over all portions of the globe illuminated by the sun (i.e.,$(\hat{R} \cdot \hat{S}) \geq 0$). However, to compare the simulations with our observations, we have to consider the ratio of the earthlight to sunlight, Γ that would be seen by an observer on the moon.

There is a systematic variation of Γ throughout the lunar month. When the moon is nearly new (lunar phase $\theta \approx \pm\pi$), the earth is nearly full, and so Γ is relatively large ($\approx 10^{-4}$). Conversely, when the moon is nearly full ($\theta \approx 0$), the earth is a thin crescent and Γ becomes vanishingly small. Fluctuations of Γ about its systematic behavior are caused by varying terrestrial conditions, including weather, the seasons and climate change. The lunar phase, θ is defined in Figure 1. After correction for the dependence of the reflectivity on lunar phase, one obtains

$$\Gamma = \frac{1}{\pi R_{em}^2} [\frac{R_{ms}}{R_{es}}]^2 \int_{(\hat{R}\cdot\hat{S}, \hat{R}\cdot\hat{M})\geq 0} d^2R(\hat{R} \cdot \hat{S})a(\hat{R} \cdot \hat{M})L, \tag{31}$$

where $\hat{M}$ is the unit vector pointing from the earth toward the moon, and the integral is over all of the earth's surface for which the sun and moon are simultaneously above the horizon (i.e., $\hat{R} \cdot \hat{S}$ and $\hat{R} \cdot \hat{M} \geq 0$). The anisotropy function, L, generally depends on surface type, cloud cover, and the zenith angles and relative azimuth of the sun and moon. L is defined so that it is unity for a Lambert surface(see Equation 7). In terms of Equation (27),

$$A^* = \frac{3}{2f_L} \Gamma \frac{R_{em}^2}{R_e^2}, \tag{32}$$

because Γ is the ratio of the earthshine to moonshine intensity after reflection from the moon is divided out.

6.3.1. The Models

In modeling the reflectance properties, a and L, of the earth, we used scene models developed for the Earth Radiation Budget Experiment (ERBE) observations (Suttles, et al. 1988). Twelve scenes are tabulated, varying from "desert" (areas for which the annual precipitation is less than 26 cm) to "mixed land-ocean" areas which are cells bordered by two land and two ocean cells. For the snow/ice cover, we used simulations from the Canadian Centre for Climate Modelling and Analysis (CCCM II, `http://www.cccma.bc.ec.gc.ca`). The Gaussian grid is roughly $3.8^\circ \times 3.8^\circ$ in longitude and latitude. The model gives the monthly mean snow/ice cover for each grid cell. The simulations of the earth's albedo were performed using two different cloud cover data sets.

Our primary dataset for the model calculations is uncalibrated images of the global cloud cover produced by the Weather Services International (WSI) Corporation. We use these data in the simulations of our observations. The WSI Corporation is the only place we know of which is currently producing real-time, online publication of global cloud cover maps. WSI is publishing maps (`http://www.intellicast.com`) composed of data from both geostationary and polar orbiting satellites, including: GOES7, GOES8, METEOSTAT 5 and POES. Data from multiple orbits are mosaicked together to provide wide-scale global and full earth views in a single image. To allow for continuous night and day viewing of cloud patterns, infrared imagery is used. We download and calibrate daily WSI images.

For studies covering the previous solar cycle, we use the D2 (revised algorithm:REFERENCE) monthly mean fractional cloud cover data from International Satellite Cloud Climatology Project (ISCCP). The ISCCP dataset covers 10 years for the period January 1984 through December 1993. We have used calibrated data on a square grid which is $2.5^\circ \times 2.5^\circ$ degrees in latitude and longitude. NEED A DETAILED DISCUSSION OF HOW CLOUD COVER DATA ARE CONVERTED TO FRACTIONAL CLOUD COVER.

ISCCP was established as part of the World Climate Research Program (WCRP) to collect and analyze satellite radiance measurements to infer the global distribution of clouds, their

properties and their diurnal, seasonal, and interannual variations. Data are collected from the suite of weather satellites (including NOAA, METEOSAT, GOES-EAST, GOES-WEST, GMS satellites) operated by several nations and processed by several groups. All ISCCP data products are archived at the ISCCP Central Archive (`http://isccp.giss.nasa.gov`).

To calibrate the daily, WSI images, each is placed on the "T42" square grid of ISCCP. We have made WSI monthly mean cloud cover maps (values are in arbitrary units), and compared them with the ISCCP monthly mean maps (in units of fractional cloud cover). This yields us a nonlinear calibration curve (HOW? DETAILS?). The first simulated results, revealed that the earth's effective albedo, $[A^*]$, obtained from thus calibrated WSI maps, was smaller than that expected from the Global Circulation Model (GCM) and from the observations. WHAT IS THIS? This implies that the fractional cloud cover was overestimated during the calibration of WSI maps. To match the observed values we have subtracted a constant value from the WSI fractional cloud cover maps (IS THERE A BETTER SOLUTION TO THIS?). It is worth noting that the above mentioned corrections in the nonlinear calibration curve only reduce the daily mean value of the earth's albedo, and do not affect its daily variations which occur as the earth rotates.

We emphasize that there is *no* intercalibration between the model reflectances and those determined from our earthshine observations. THE PREVIOUS PARAGRAPH BELIES THIS.

6.3.2. Model Results Covering 1999 -2000

In Figure 19, we show daily mean global albedos from simulations of the whole earth covering 1999.0-2001.5, and calculated using Equation (30). Roughly, the figure shows peaks in the earth's reflectivity in the fall and spring, while showing minima in the winter and summer (see §6.4). From this, we determine a mean Bond albedo of 0.300 ± 0.002 (WHAT IS THE PRECISE VALUE?) over that period.

Applying Equation (32), we also simulated the earthshine observations shown in Figure 15 covering *the same parts of the earth at the same time*. The results are shown in Figure 20. Note

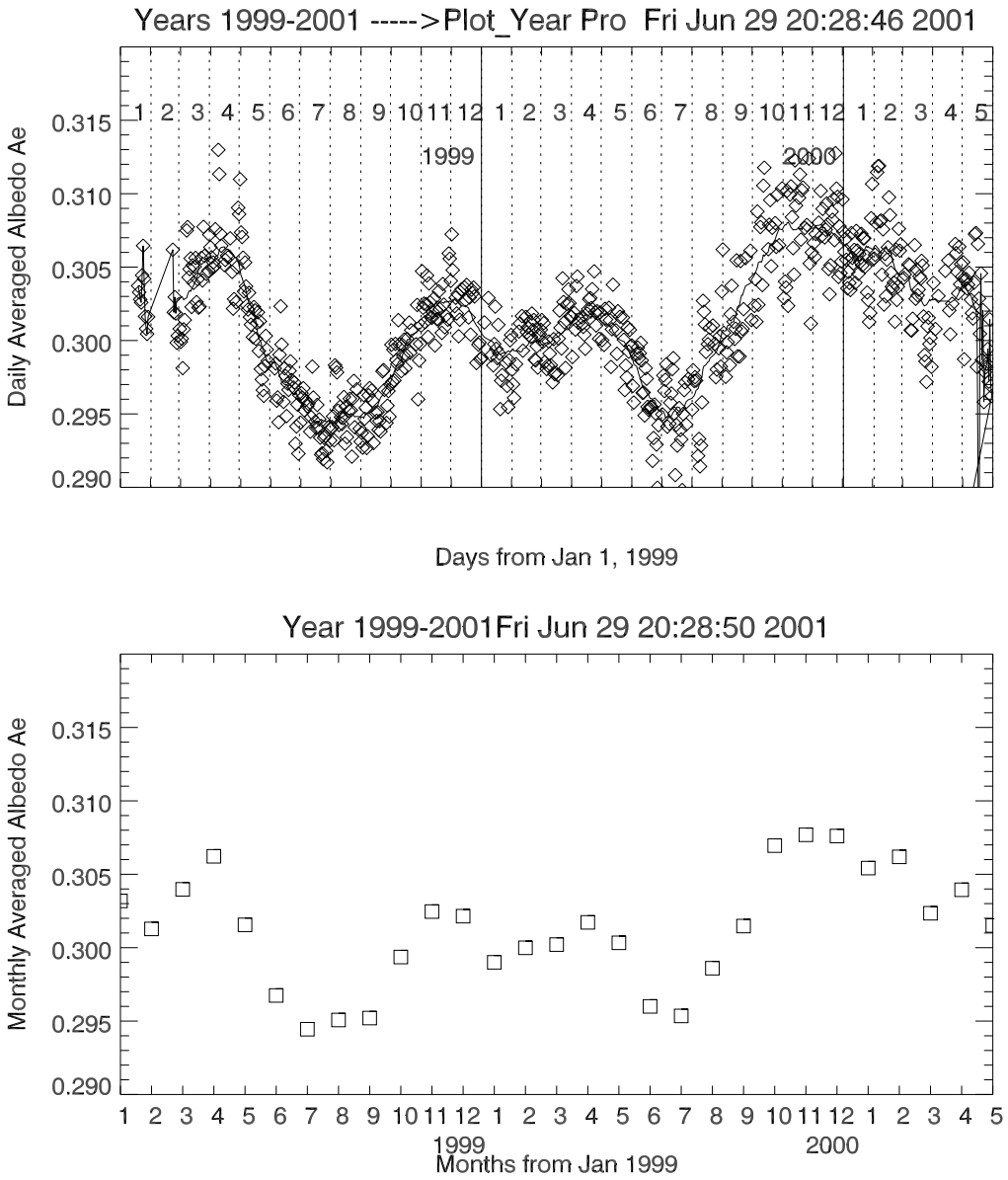

Fig. 19.— Daily mean global albedos (diamonds) during the two year simulation beginning January 1999. The bold solid line shows the 30 day running mean. The amplitude of the simulated seasonal variation of the whole earth albedo is 4-5%.

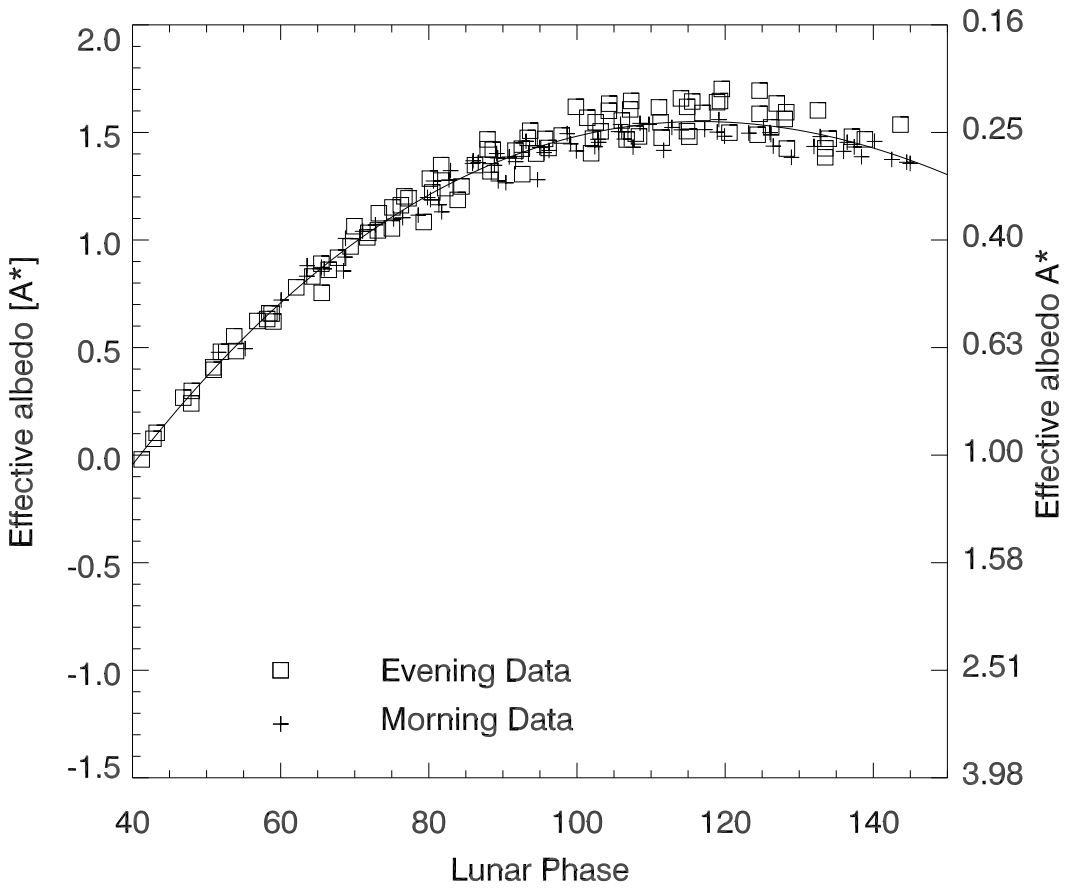

Fig. 20.— Plot of [A*] vs. lunar phase (in absolute value) from simulations covering same phase of the earth as the observational results in Figure 15. Each data point represents the averaged [A*] value throughout one night; "+" indicates morning observation (lunar phase > 0) and "square" indicates evening observation (lunar phase < 0). The solid curve is a 3^{rd} degree polynomial fit of the data points. The solid curve is indistinguishable from the fit to the data shown in Figure 15. On the right-hand y-axis, we show the scale in units of A^*.

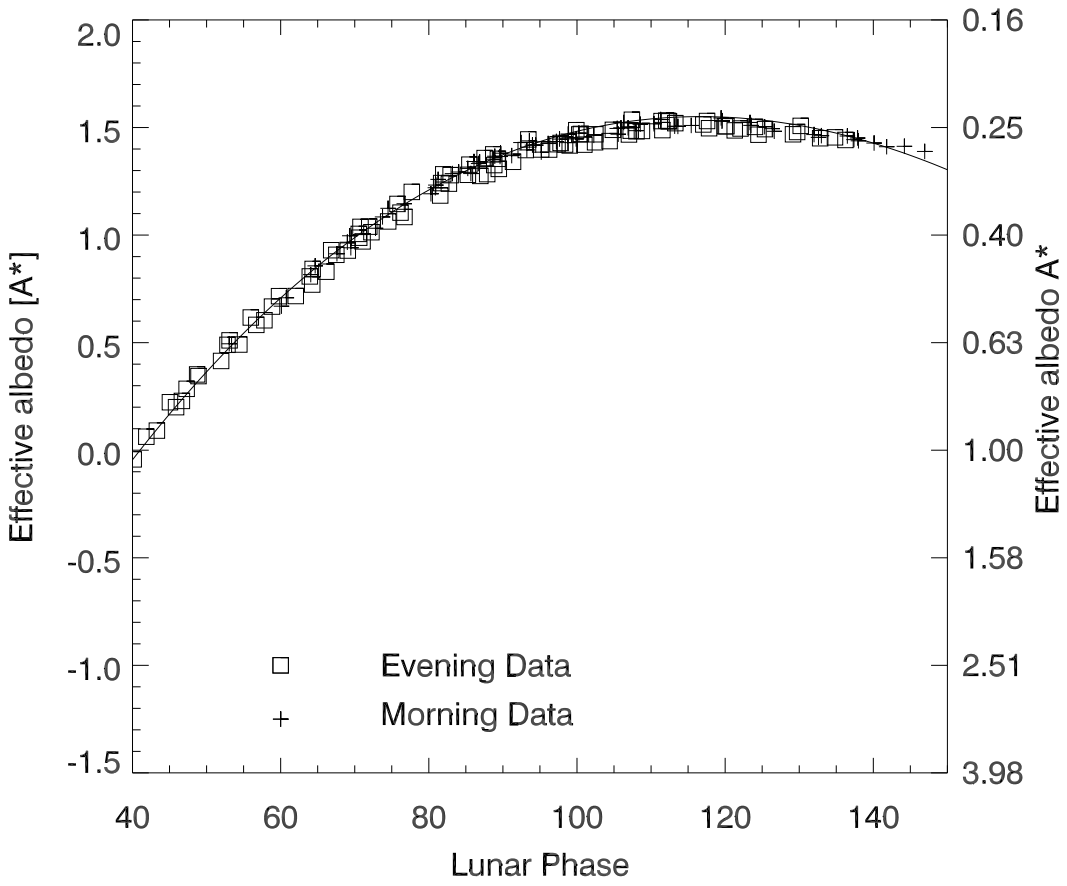

Fig. 21.— Plot of [A*] vs. lunar phase (in absolute value) from simulations covering the whole earth for all days for which we have observations. Each point represents the 24-hour average of UT defined days for which we have earthshine data. The "+"'s and "squares"'s are given to show whether the 2-hour average is connected to observations at positive or negative lunar phase. The solid curve is a 3^{rd} degree polynomial fit of the data points. The solid curve is indistinguishable from the fit to the data shown in Figure 15. On the right-hand y-axis, we show the scale in units of A^*.

that the distribution is tighter to the fit than in Figure 15. Thus, the greater scatter in Figure 15 cannot be due to different nights for the same lunar phase seeing different parts of the earth because each night's simulation covers exactly the parts of the earth which are observed. We shall return to the origin of the difference in the spread in §6.4. However, like the observational results, there is no clear distinction between the simulations for day and night. It is also clear from the simulations shown in Figure 20 that the evening data have a greater scatter about the mean than do the morning data. This implies a more variable cloud cover over Asia. In Figure 21, we show the same kind of plot as Figure 20, but covering the entire earth for nights for which we have observations and cloud cover data (see the difference in coverage between the solid lines and solid boxes in Figure 22). Since the whole earth simulations average over more of the globe, it is not a surprise that the simulations of the whole earth show considerably less scatter than those of just part of the earth. We also note that the mean albedo, A^*, is larger for the whole earth than it is for the part we see (BY HOW MUCH IN % AND WHY, IS THERE MORE LAND?). NEED NUMBERS FOR ALL ERROR BARS.

6.3.3. Comparing Daily Observations and Model Results

In Figure 22, we show evening and morning earthshine observations overlaid on model calculations covering the entire day. The two lower panels show the earthshine as a function of time (note that the time is plotted in reverse chronological order). The solid curve shows the variation of the calculated effective albedo A^* during the twenty-four hour period, and the solid boxes are the observed effective albedo. These results come from near to a quarter moon and are compared with the earthwide WSI cloud cover from the same day in the top panel.

The top panel shows the cloud cover maps illustrating which parts of the earth contributes to the earthshine. We highlight (the large bright areas) those parts of the earth that are the source of the earthshine (i.e., are simultaneously in the sunshine and are visible from the moon at some time during the observation). The cloud cover is also shown as secondary grayscale, for instance, the east-west dark bands just north and sourth of the equator illustrate cloudless areas. We also

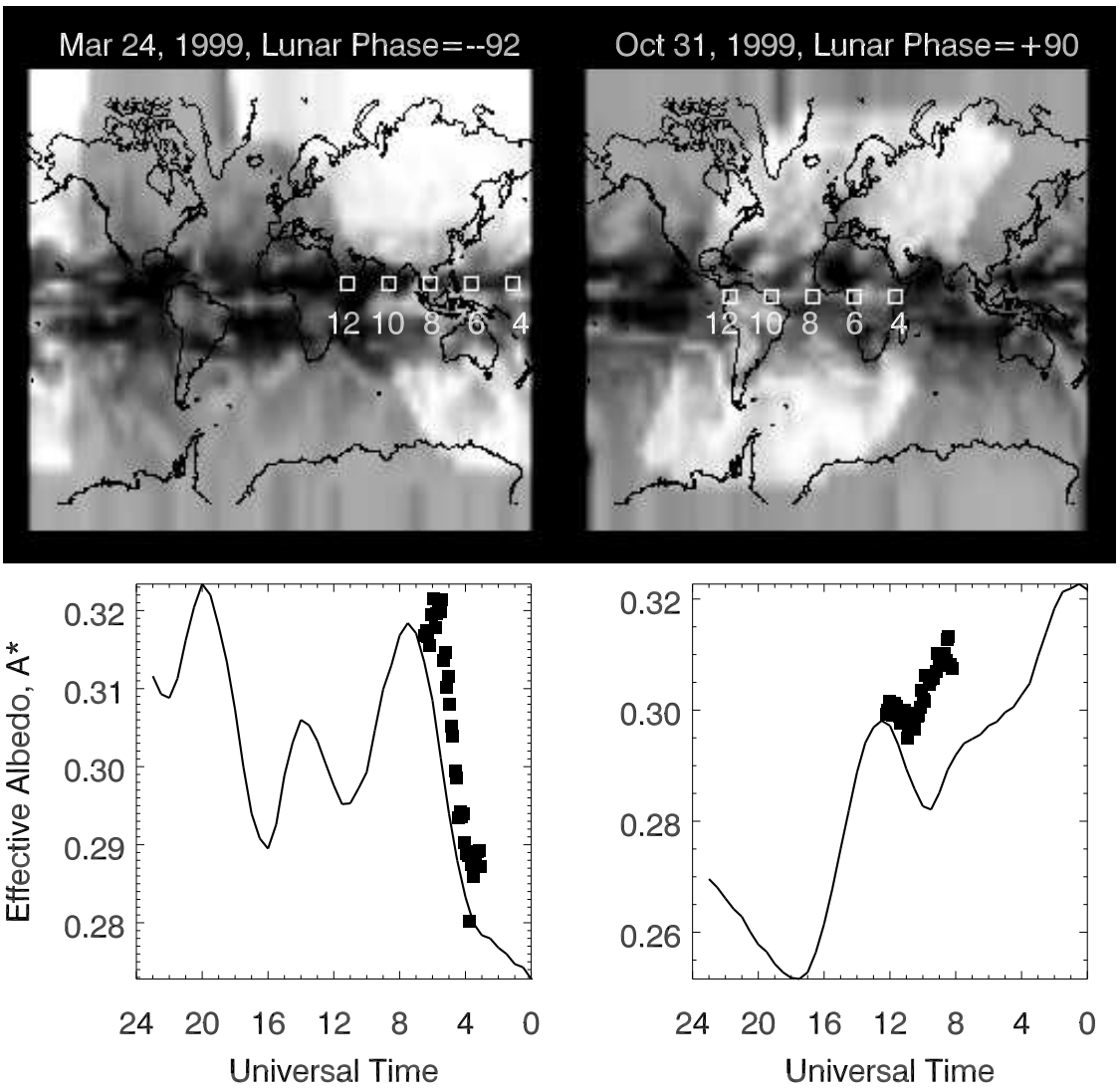

Fig. 22.— In the top panels, the satellite-derived WSI cloud cover maps are shown in gray-scale with brighter areas indicating greater cloud cover. The extended bright areas highlight those parts of the earth that are the source of the earthshine. For 31 October 1999, note that the northernmost regions are not sunlit and the southernmost regions do not contribute to earthshine because the moon is fairly far north in the sky. Simulations of 506 nights show that not detecting the pole in this way reduces A by about 0.005 because of the nearly invariant, relative brightness of the polar regions (SHOULD THIS GO ELSEWHERE?). The boxes in the top panels indicate the longitudes of maximal contribution to the earthshine at the Universal Time (UT) shown. The solid boxes in the lower panels show the observed effective albedo as a function of time (note that the time axis is reversed), while the solid line indicates the simulated A^*.

indicate with boxes an intersection of the earth's surface with the bisectrix of the spatial angle between the surface intersection of the lines from the center of the earth to the moon and the sun or, in other words, the point of equal angles, where the angle of incidence is equal to the angle of reflection.

The observations are consistent with the simulations for 24 March 1999, which is one of the nights for which the agreement is quite good. On 31 October 1999, a more typical night, there is a discrepancy of about 5% relative (or 0.015 absolute) in the effective albedo. One may notice slight, and opposite, temporal offsets between the simulations and observations in the lower panels. One must bear in mind that the cloud cover data are a composite of many observations which are taken over about six hours. Thus, a precise timing between the observations and simulations is not possible. We simply assume that the cloud cover is invariant from one posting to the next. We make no effort to smooth the transition (WHAT IS THE TYPICAL TRANSITION??). Under circumstances of rapid cloud movement could result in observational and simulated results which don't have the same form. (LOOK FOR EXAMPLES, AND DISCUSS BY CLOUD TYPE. DISCUSS CLOUD TYPE IN GENERAL)

As the cloud cover is fairly steady and high at geographical latitudes above 45°, the short timescale variations in reflectance in Figure 22 are due to primarily to irregularities in the fractional cloud cover at low latitudes and secondarily to the scene type. In the lower left panel of Figure 22, one sees that the observed and calculated maxima in A^* at 7:00 UT are due to a relative cloud excess over the Far East, while the calculated local minimum in A^* at 11:00 UT arises from the cloudless area above India and the Arabian Sea. In the lower left panel, there is a nearly 10% change in A^* over about two hours. This sharp increase is due to the increasing contribution of a cloudy Asia to the earth's reflectance as the earth rotates. An offset between the observed and calculated effective albedos is evident in the lower right panel; this turns out to typify the general result that the observed night-to-night variations are greater than those of the simulations. The larger variation in the observed results is a consequence of the more muted seasonal variations predicted using the models.

6.4. Seasonal Averages of [A*]

The seasonal variation of the earth's reflectance is not well-known. In fact, Goode et al. (2001) have shown that over a year and a half (1999.0-2000.5) that the earth's seasonal variation was upwards of 20%. This surprisingly large value is about twice that determined from the simulations covering the same nights and the same parts of the earth. The formulation of the simulations was detailed in §6.3. Large scale, seasonal variations can be well-determined from the earthshine. Starting from Equation (27), the fractional seasonal variation depends only on the observed intensities extrapolated to zero airmass. That is,

$$\sum_{i=1}^{N} \frac{A^*_{\rm seas}(\theta_i) - \overline{A^*}(\theta_i)}{\overline{A^*}(\theta_i)} = \sum_{i=1}^{N} \frac{(\frac{I_a/T_a}{I_b/T_b})_{\rm seas,i} - \overline{(\frac{I_a/T_a}{I_b/T_b})_{\rm i}}}{\overline{(\frac{I_a/T_a}{I_b/T_b})_{\rm i}}}, \tag{33}$$

where N is the number of nights for which we have data in a particular season, θ_i is the lunar phase on the i^{th} night of that season, and $\overline{A^*}(\theta_i)$ is the fit shown in Figure 15. The average for a particular season is computed from each night's data by determining the fractional change for that night's phase angle with respect to the mean for that phase angle for all nights, irrespective of season. With this formulation, possible systematic errors associated with the moon's geometric albedo and the phase function have been largely eliminated. In the formulation of Equation (33), we minimize the dependence on lunar phase by recalling that effects arising from the fact that A^* is a strong function of lunar phase. These seasonal anomalies, which are formulated as fractional changes in A^*, carry information about variations in weather, climate and surface type. The fractional seasonal variation of the earth's reflectance over two years (1999-2000), as determined from our earthshine observations, is shown in Figure 23. From December 1998 through the beginning of January 2001, there are 255 nights of observations with 22 nights in the earliest bin, 23 nights in the next bin and 15 nights in each of remaining 14 bins; the extra nights in the two earliest bins serve to reduce the uncertainties. The three points in the last part of 2000 and early 2001 show an especially large negative fractional anomaly implying that seasonal variations are more like 30%, rather than the 20% reported by Goode et al. (2001). The three points are well-correlated with their simulated counterparts, but show a large sysmeatic offset. We have

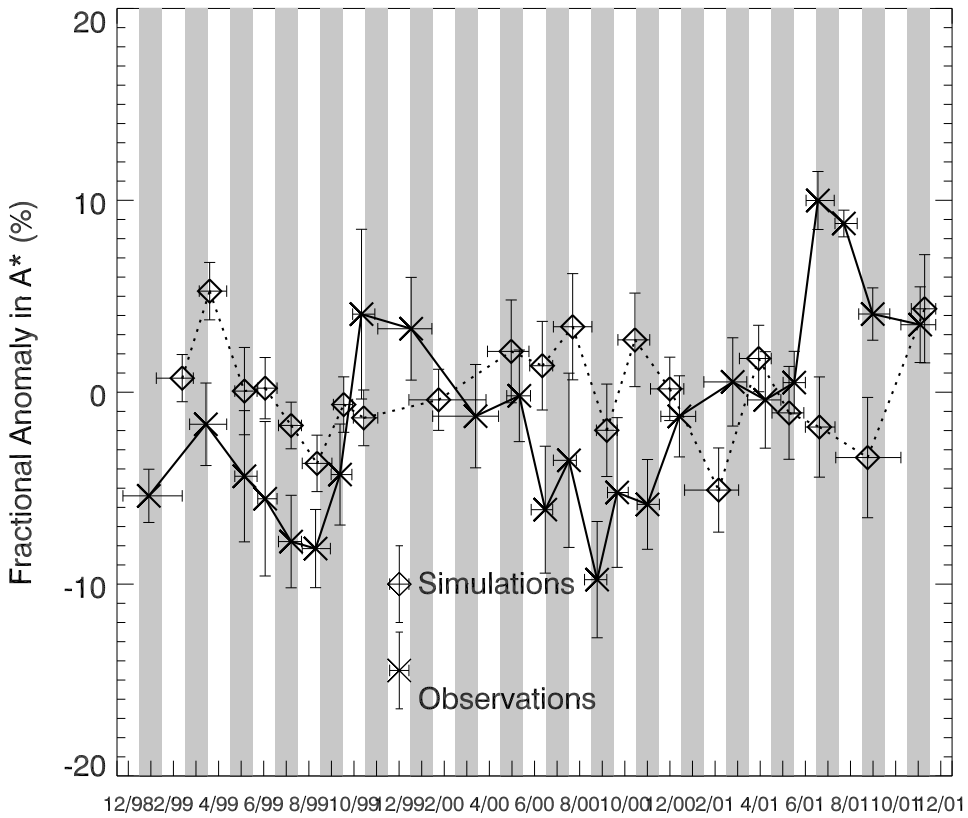

Fig. 23.— Seasonal anomalies in the effective albedo, A^*. From December 1998 through mid-December 2001, there are 288 nights of observations, each bin containing 11 nights; the last bin contains only the remaining 2 nights (MAYBE WE SHOULD NOT PLOT IT). From January 1999 onward, there are 227 nights for which we have both observations and contemporaneous satellite cloud cover data, which have been averaged in 20 bins with 11 nights in each (21st has only 7 nights AGAIN MAYBE BETTER NOT PLOT IT). The $\times$'s show the mean of the observations, with the vertical bars being the standard deviation of the mean. The size of the latter stems from the large night-to-night variations in the cloud cover, rather than from uncertainties in the observations. The horizontal bars indicate the temporal span of each average. The diamonds indicate the corresponding simulation results.

looked carefully and find no instrumental error leading to those three points. Further, we note that the most recent data point in Figure 23 does not show the offset.

As in the whole earth simulations in Figure 19, one can see in Figure 23 a clear seasonal trend with the earth being brightest in the spring, when it is also the cloudiest. We see the seasonal trends in spite of the fact that the night-to-night variations are a significant fraction of the seasonal trends. We emphasize that the large vertical error bars arise from the large night-to-night variations in the cloud cover, rather than any errors in the data (see also Figure 15). In fact, the night-to-night error bars are small compared to the formal error bars in Figure 15 (which are within the symbols). With all of this, we see about 30% variation in A^* from season-to-season.

The observed seasonal variation is correlated with the corresponding simulations with a 95% confidence level. However, the observations show about three times as much variability, with the differences being greatest at the extremes. The seasonal variation of albedo is the essential origin of the relatively greater spread among the observed $[A^*]$'s in Figure 15. The muted seasonal amplitude of the simulations may well derive from the coarse binning of the scene models and/or the use of simulated snow and ice cover. DETAILS LIKE CLOUD COVER BINNING AND WHY THAT IS DONE. We note that the whole earth seasonal simulations in Figure 19 show an even more muted seasonal variation. This is no surprise considering the relative spreads about the mean in Figures 20 and 21.

6.5. Comparisons with Danjon's Results

To compare our results with those of Danjon, we show in Figure 24 the fit our data (see Figure 15) analyzed using Danjon's phase function (as shown in in Figure 14). The solid line in the figure shows the fit to the data using the correct lunar phase function. Clearly, the result of using Danjon's phase function is an albedo that is about 0.1 larger than the true value for phases near the quarter moon. These phases are most significant in the determination of the albedo, as can be seen from Figure 25. The inconsistency between Danjon's albedo of about 0.40 and our observed

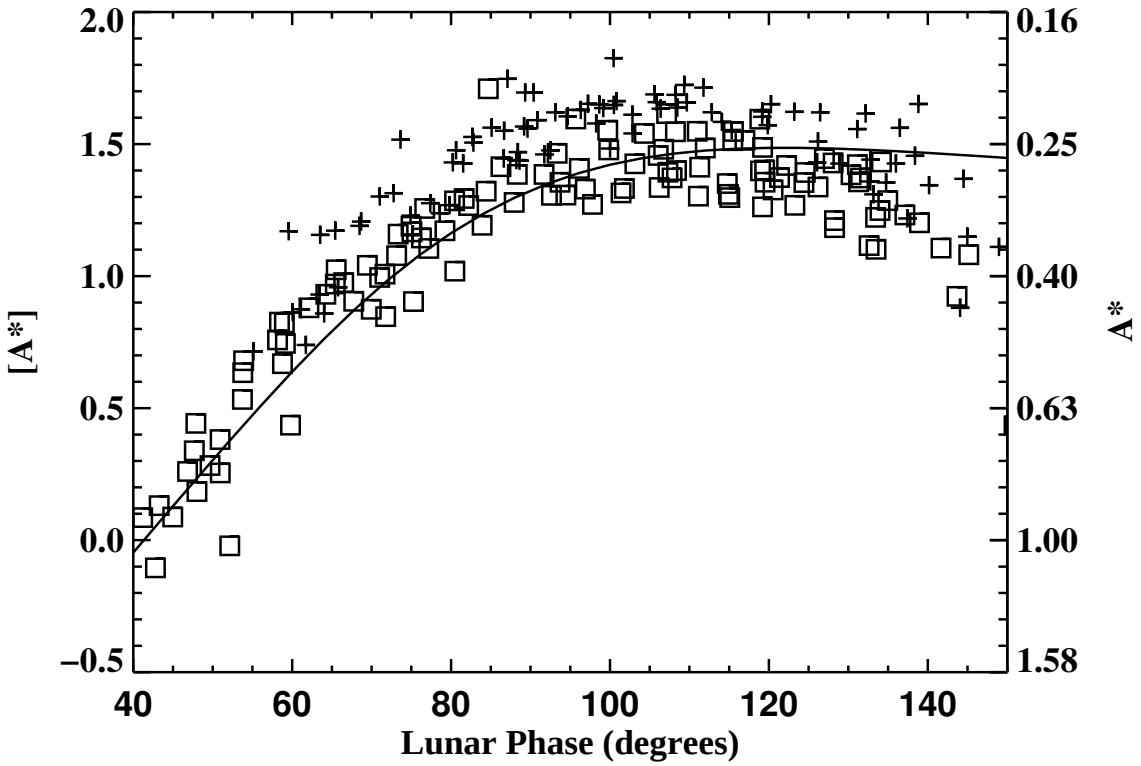

Fig. 24.— Danjon's lunar phase function (see Figure 14) was used to analyze our observational data. The solid curve is the regularized fit to the same data calculated using our lunar phase functions. The points shown in in the figure are those derived using Danjon's phase function. Since Danjon's phase function is systematically lower than the correct one, this explains how Danjon derived an albedo of about 0.4 from his observations, which is much higher than our observed and simulated values of about 0.3.

value of 0.30 comes mainly from Danjon's underestimate of the lunar opposition effect (Flatte et al., 1991; MacDonald and Koonin, 1992) which carries over from the significant overestimate of the lunar phase function near the quarter moon which dominates the determination of the albedo.

———————————

TO INCLUDE THE FOLLOWING INTO THE TEXT WE HAVE TO MAKE A FIGURE. THE CORRESPONDING FIGURE IS MISSING NOW. DO I HAVE TO MAKE THIS FIGURE? YES! In Figure 23, we also compare the results with model calculations using monthly averaged cloud cover data combined from 1987. The monthly averaged cloud cover data are from the International Satellite Cloud Climatology Project (ISCCP). The cloud cover which is input to the model cover the same areas as the earthshine. The cloud cover data span the ten year period from the beginning of 1984 through the end of 1993. We chose 1987 because of the availability of processed satellite data. We note that 1987 was a time of a rising new solar cycle, like 1999. We note that the latter calculations do not correlate quite as well with the observational data, as did the former calculations.

———————————————————————

N years Ae dAe,

———————————————————————

1 1996(jan) - 1998(mar) 0.293307 [Ae(3)-ae(1)]/Ae(1) = 1.1

2 2002(jan) - 2004(mar) 0.295585 [Ae(2)-ae(1)]/Ae(1) = 0.7

3 2008(jan) - 2010(mar) 0.296505 [Ae(3)-ae(2)]/Ae(2) = 0.3

———————————————————————

Attached is a plot of lunar latitudes for these years. Two gaps are 1999-2001 and 2005-2007. So, we see that in 96-98 the moon was much lower above the equator then in 2008-2010. This plot agrees with the values of Ae in the table.

Because the gravitational effects of the sun and moon are not always the same, there is some wobble in the motion of the earth's axis; this wobble, called nutation, causes the celestial poles to move, not in perfect circles, but in a series of S-shaped curves with a period of 18.6 years.

–NEED MONTHLY AVERAGES FROM ISCCP DATA. ————————————————-

7. Determining the Bond Albedo from the $[A^*]$

To determine the Bond albedo, A, from our earthshine observations we need to integrate $A^*(\theta)$ over all phases of the moon. Combining Equations (5), (6) and (8), we find

$$A = \frac{2}{3}\int_{-\pi}^{\pi} d\theta A^*(\theta) f_L(\theta)\sin\theta. \tag{34}$$

The kernel of the integrand, $f_L(\theta)\sin\theta$, is plotted in Figure 25. The figure illustrates one of the two basic problems in the earthshine to determine the earth's Bond albedo. The first, and more signficant problem, is that we cannot measure the earthshine for all phases of the moon. However, it is clear from Figure 25 that this becomes a problem primarily for lunar phases near the new moon, where the earth is most nearly Lambertian. Further, it can be seen in Figure 25 that the integrand in Equation (34) peaks near the quarter moon ($|\theta| \sim 130°$), when the moon shows a relatively sizeable earthshine, while its phase is not so large that the earthshine is visible only briefly near sunset or sunrise. To evaluate Equation (34) to an accuracy of 0.002 requires data for $|\theta| \geq 30°$. Thus, earthshine observations for most lunar phases are needed for an absolute value of the albedo, while observations near the new moon are most sensitive to variations in the albedo because so much of the earth is visible. The second basic problem in using the earthshine to determine the albedo arises because the orbit of the moon traces out an ellipse in the full three dimension space surrounding the earth, so we cannot measure the earthshine in all directions. Therefore, we are insensitive to any azimuthal anisotropy in the earthshine. Later in this section, we use simulations to show that the anisotropy is not significant, and one can account for it. We do this by taking advantage of full spatial coverage provided by the simulations. For the first problem, we find that we can obtain a quite reliable Bond albedo from the earthshine data using a

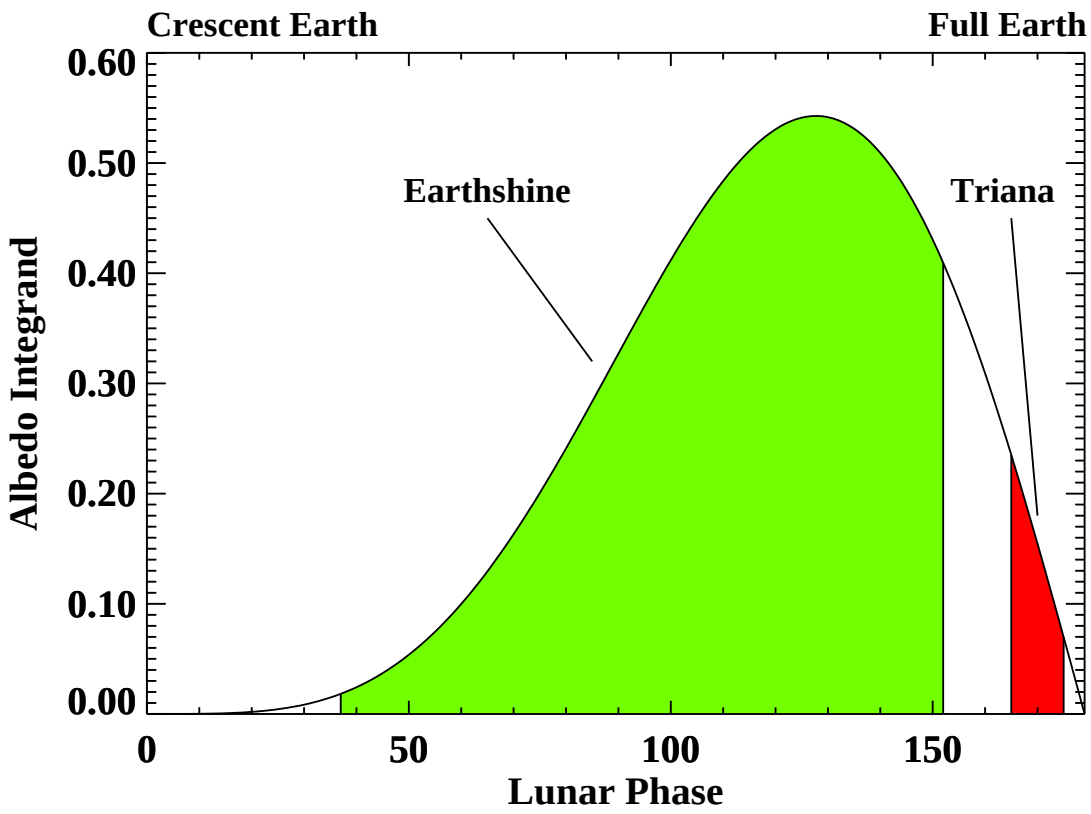

Fig. 25.— The kernel $(f_L(\theta)\sin\theta)$ from which the Bond albedo is determined (see Equation 34) is shown as a function of lunar phase. Its behavior is dominated by the Lambert phase function for small phase angles, and by $\sin\theta$ for large phase angles. In green, we indicate contribution to the Bond albedo that arises the range lunar phases over which we measure the earthshine. In red, we show the approximate contribution from a satellite orbiting about L1, assuming the proposed orbit of Triana.

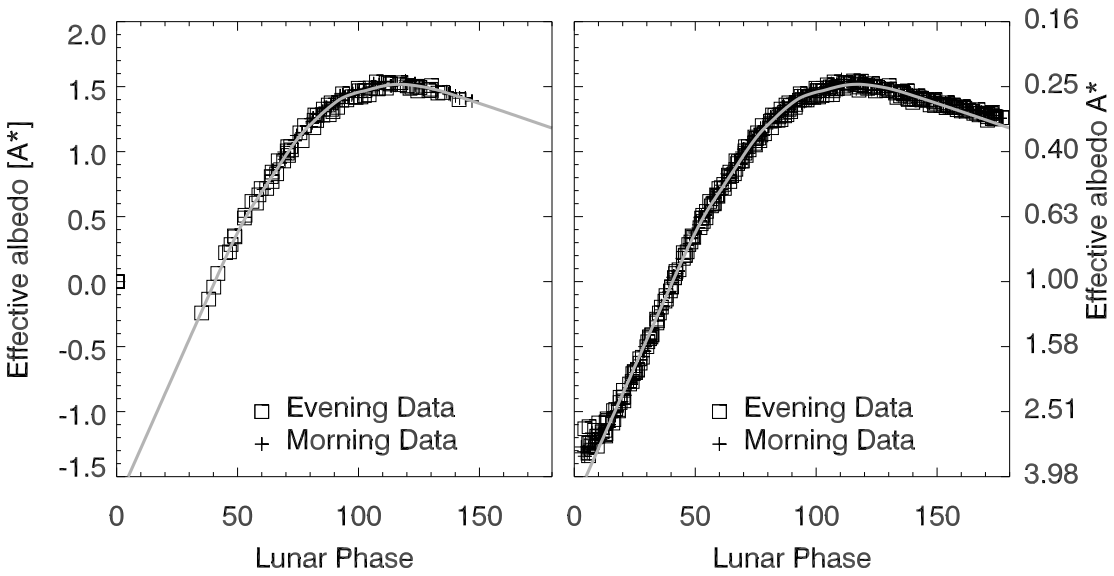

Fig. 26.— Each box represent a whole earth (i.e., covering a twenty-four hour period) simulated albedo. left panel) Whole earth simulations for which the twenty-four hour period includes nights for which we have earthshine data and cloud cover (171 nights). The 171 nights span the two-year period from 8December 1998-30November 2000. right panel) Whole earth simulations for all twenty-four hour periods, during the same two-year period, for which we have cloud cover data (506 nights – 272 during the waxing moon and 264 during the waning phase). The gray curve in both panels is derived from the constrained or regularized least-squares fit to the left panel. WHAT IS THE SPAN OF DATES HERE?

constrained least squares, or regularized fit to the data – guided by the simulations. For a review of regularization and its utility, see Goode (1995).

For the right panel of Figure 26, we do a least-squares determination of A^* as a function of lunar phase, and then use Equation (34) to determine a Bond albedo of 0.294±0.002, where the error is defined by the least squares error in the fit to the simulations in the the right panel of Figure 26. Note that the fit shown in the right panel is not from this least-squares fit. Rather, we show the fit to the left panel, which is developed later in this section. For the least-squares determination of A^* from the simulations in the right panel, we minimized χ^2 (per degree of freedom),

$$\chi^2 = \frac{1}{(N - N_f)} \sum_{j=1}^{N} \left(\frac{\Delta A_j^*}{\sigma_j} \right)^2 , \tag{35}$$

where N and N_f are the number of nights simulated and the number of degrees of freedom in the solution, and where ΔA_j^* and σ_j are the deviation of the fit from A_j^* and the error in the determination of A_j^*, respectively.

For the left panel, we use a regularized fit to extend to larger and smaller phase angles than we have in the data. In the regularization, we minimize

$$\chi^2 (1 - \frac{N}{N_f}) + \lambda \int_{-\pi}^{\pi} [\theta^2 \frac{d^2}{d\theta^2} (\frac{\Delta A_j^*}{A^*})]^2 d\theta, \tag{36}$$

where ΔA_j^* is the difference between the j^{th} data point and the fit to the data (the quantity we are determining) in the left panel, while λ is the regularization parameter which is, in reality, a smoothing constraint. In principle, the parameter is adjusted until χ^2 is the same as it was in the right panel of Figure 26. However, the χ^2 space is relatively flat, so one typically weakens λ until short wavelength oscillations almost begin to appear in the fitted A^* function. Other forms of the constraint are certainly possible, but a second derivative constraint seems to work best here. In applying the regularization to the left panel, we have the advantage of being able to check our result against the right panel. In direct application of the method, we find a Bond albedo of 0.296±0.002 (TRUEA?), which is quite consistent with the pure least-squares result for the right panel. The fit shown in the right panel is the regularized result from the left panel. The fit is

fairly insensitive to the choice of λ over nearly an order of magnitude.

Applying the same regularization to the observational data of Figure 15, which contains, as a subset, the 171 nights in the left panel of Figure 26, we find a Bond albedo of 0.294±0.004. The fit is shown in the the left panel of Figure 27. The right panel shows the corresponding fit for the simulations covering the same times and parts of the that contribute to the earthshine. The larger errors in observational results are indicative of the greater spread of the observational points about the mean (compare the left and right panels of Figure 27). TRUE A FOR RIGHT PANEL?

One of the prices paid using regularization is that the point to point values of the solution are correlated, implying that the meaning of the errors is somewhat damaged. The damage is reflected in errors that are smaller than they are in reality. For instance, if the constraint were dominant, the error at each point in the solution would be the standard deviation of the mean. To ascertain whether the errors quoted in this section are significantly too small, we determine the errors in a completely different way which does not suffer from the limitations imposed by regularization (see §7.1).

As mentioned at the beginning of this section, one concern about measuring the earthshine to precisely determine the earth's albedo is the amount of anisotropy in the earth's scattering. At any instant, the moon subtends $0^\circ.5$ as seen from the earth and the obliquity of the moon's orbit extends this coverage over the lunar month to only 6° on either side of the ecliptic; thus, earthshine is not sensitive to light scattered out of the ecliptic. We can directly test the sensitivity by comparing the result of simulating the Bond albedo for the *whole* earth to that using the simulated earthshine. For the whole earth case, we use Equation (30) and calculate a two year average, for which the result (A=0.300±0.002) is shown in Figure 19. For the earthshine, we are effectively assuming that for all lunar phases the earthshine does not depend on the azimuthal scattering angle. We test Equation (34) by using $A^*(\theta)$ from the right panel of Figure 26 from which we determine a two year average Bond albedo of 0.294±0.002. The discrepancy arises because the relatively brighter polar regions are sometimes in the sunshine, but not in the earthshine. This effect is illustrated in the right panel of Figure 22 for which the moon is northerly in the sky and

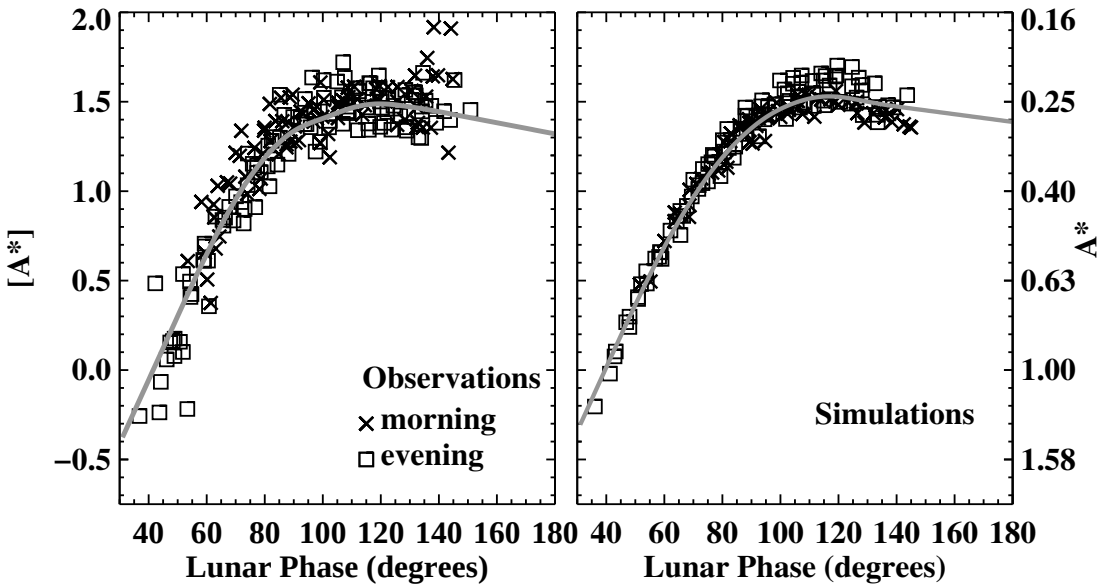

Fig. 27.— left panel) Observed (left panel) [A^*]'s plotted against the absolute value of the lunar phase from 225 clear observing nights from December 1998 through the beginning of November 2000. Simulations (right panel) are shown covering the time intervals and parts of the earth that contribute to the earthshine signal for the 171 nights for which there were observations and contemporaneous cloud cover data. Each data point represents a nightly average of 0.5-3.0 minute earthshine measurements taken once every five minutes with 0.1-5.0 second moonshine observations interspersed. Error bars for each night would be within the symbols. Constrained least square fits to the data and simulations are shown by the curves. For the 171 nights for which we have observations and simulations, the anomalies relative to the separate fitted curves are correlated at the 95% confidence level.

and doesn't receive light from the sunlight southernmost regions of the earth.

A higher order difficulty in determining the earth's reflectance from the albedo is that the intensity of the earthshine varies with the precession of the lunar nodes. This precession of the moon's orbital plane has a period of 18.6 years. The sensitivity of the earthshine arises from the anisotropy of the light scattered by the earth. For example, when the declination of the new moon is a maximum (some 29°), and it is near the northern-summer solstice, more of the arctic polar ice cap is visible and the earthshine will be brighter. Some nine years later, the lunar declination under the same conditions will be only 18°, and the earthshine will be a minimum. We have performed simulations to study this effect and the results appear in Figure 28. It is clear from the figure that the nutation of lunar nodes perturbs $[A^*]$ at the $0^m.004$ level or less. One must account for this in comparing earthshine results from different epochs, like we did in comparing 1994-5 to 1999-2000. We note that the effect of the precession on the changing albedo is negligible when we compare those two time frames. We can also compare 1999 and 2000.

The Bond albedo from earthshine observations for 1999-2000 is 0.294±0.004. Separating out the 1999 and 2000 data in Figure 15, and calculating the Bond albedo using Equation (34), we find for 1999 that A=0.296±0.003 and for 2000 that A=0.291±0.007. The effect of the precession of the plane of the moon's orbit would be to increase the Bond albedo by 0.001 from 1999 to 2000. So, correcting for the precession would actually increase the difference between the 1999 and 2000 results. The combined difference between 1999 and 2000 is 0.006±0.009, assuming the 1999 and 2000 errors are independent. Inspite of its marginal signifcance, we note that this result goes in the same direction as the picture in which the earth's albedo is lower when the cosmic ray flux is lower, i.e., times of high solar magnetic activity. In §7.2, we shall make a more detailed comparison of the temporal evolution of the Bond albedo from observations and simulations to the evolution of the terrestrial cosmic ray flux.

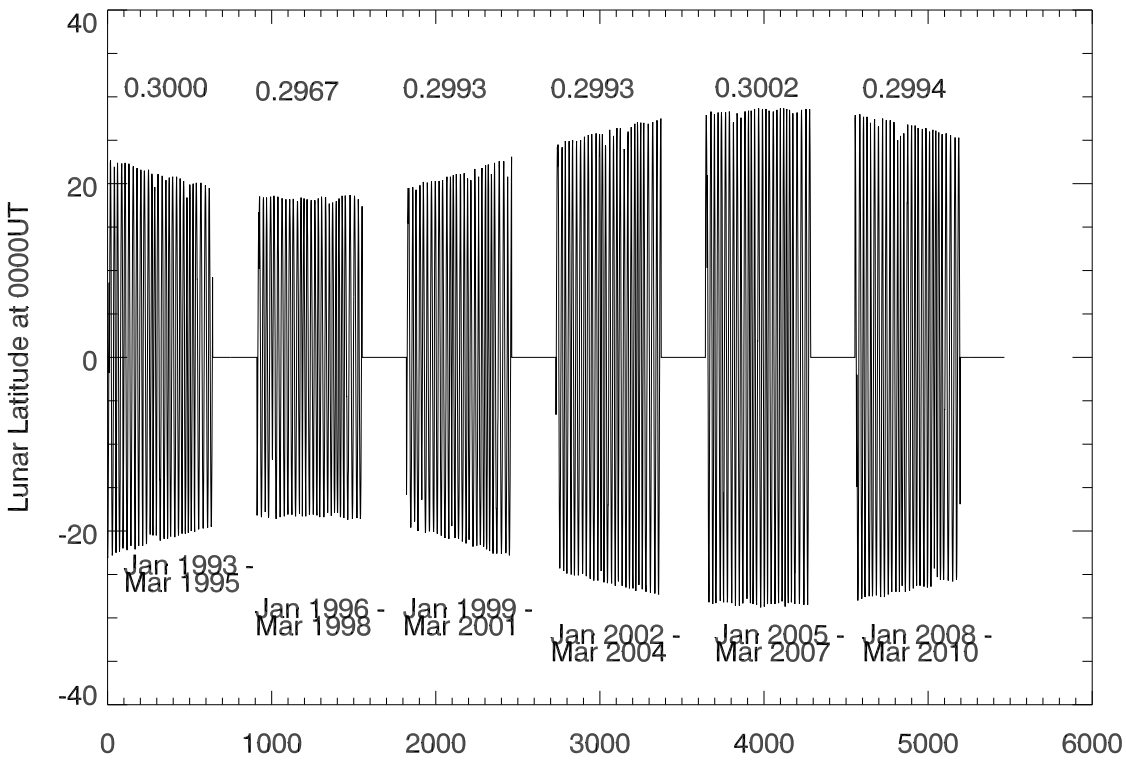

Fig. 28.— The precession of moon's orbital plane with a period of 18.6 years induces a corresponding periodicity in the earth's albedo. The figure shows simulations using 1999-2000 cloud cover for the two year pairs shown – counting backward and forward from 1999-2000. The albedo was simulated using Equation (34).

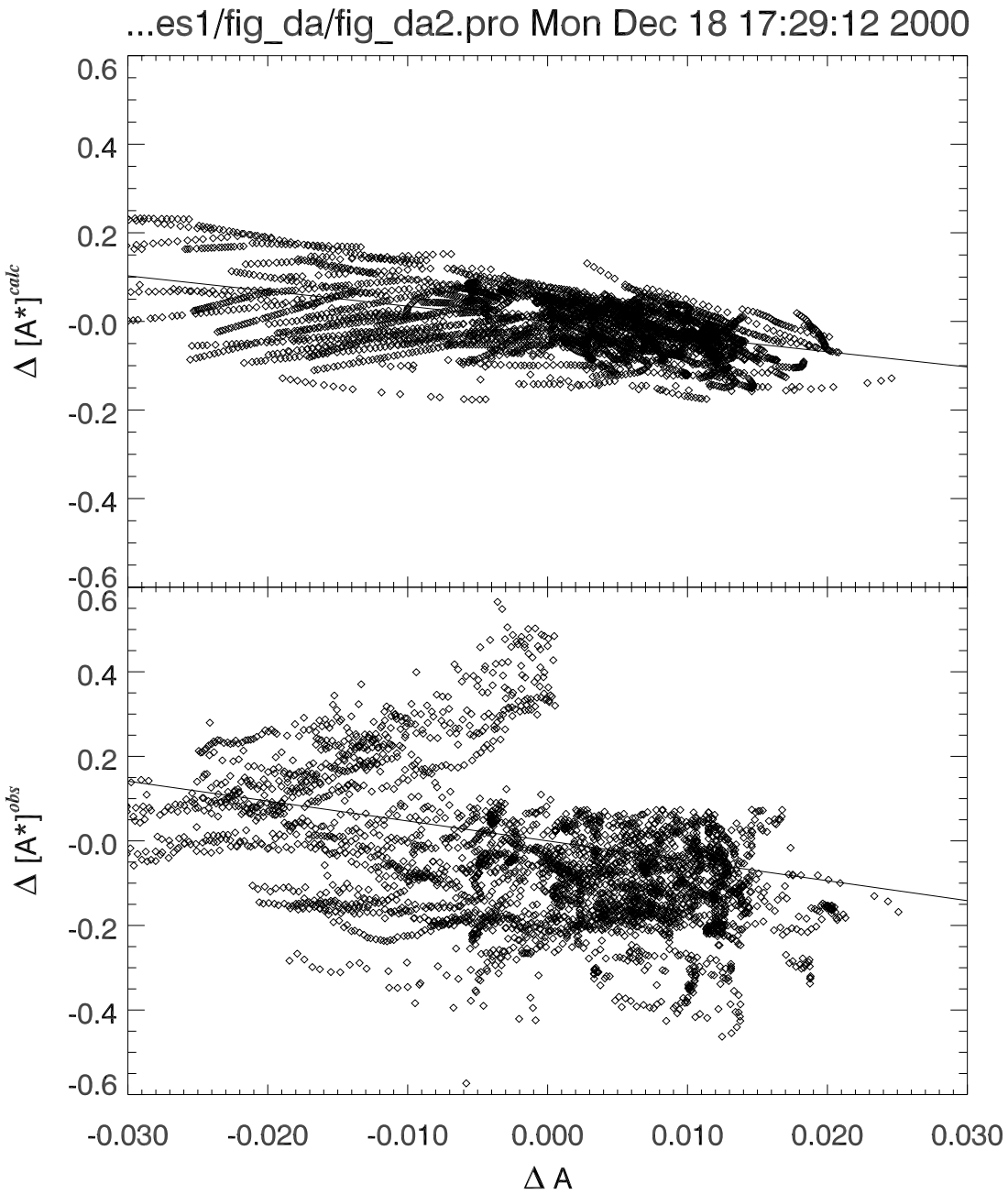

Fig. 29.— top panel) Linear correlation of the calculated earthshine anomaly, $\Delta[\mathrm{A}^*]^{\mathrm{calc}}$, with the calculated global albedo anomaly, ΔA for 3702 calculations for lunar phase angles for which $140^\circ \geq |\theta| \geq 40^\circ$. bottom panel) Linear fit to observational anomalies, $\Delta[\mathrm{A}^*]^{\mathrm{obs}}$, for the same 3702 time points, assuming ΔA is the same as that from the calculations.

7.1. Alternate Determination of Errors in the Bond Albedo

In calculating the Bond albedo, we need to connect the precision to which we determine the $[A^*]$ to the accuracy to which we determine A. To do this, we use the daily cloud cover map and calculate the whole earth albedo A, the effective earth's albedo $[A^*]$ and the variation of each during the full day. For the calculations, we use a third-order polynominal fit to $[A^*]$, which defines a mean calculated effective albedo for the earth, $\overline{[A^*(\theta)]}$, and residuals, $\Delta[A^*]^{calc} = [A^*] - \overline{[A^*(\theta)]}$; these latter carry information about the weather, climate and surface type. Their correlation with the calculated global albedo anomalies ($\Delta A = A - \overline{A}$) is shown in the top panel of Figure 29, where we have included the 142 nights for which we have cloud cover and observations. Further, in $[A^*]$ we only include the times for which we have observations (3702 time points). In the top panel, we show a linear fit to simulations.

For the observational data, we make a scatter plot for the same time points, and assume they correlate with ΔA, as shown in the lower panel of Figure 29. In detail, we used a third-order polynomial fit to define a mean observed effective albedo $\overline{[A^*(\theta)]}$ and observed residuals $\Delta[A^*]^{obs}$. Their correlation with the global calculated albedo anomalies ($\Delta A = A - \overline{A}$) is shown in the lower panel of Figure 29 including a linear fit to the points. For each time point in each night, we assume ΔA is the same as the corresponding calculated point. This figure gives us insight into how accurately we can measure the albedo.

Using Figure 29, we note that a variation in A of 0.01 corresponds to changes of 4.7% (for $[A^*]^{obs}$) and a 3.4% (for $[A^*]^{calc}$) in the effective albedo ($0^m.047 - 0^m.034$ in $[A^*]$). Equivalently, a 1% earthshine measurement determines the albedo with a precision of 0.002. To place this precision in context, we note that independent satellite determinations of the monthly mean albedo can differ by 0.005 or more and that the seasonal range of the monthly mean albedo is 0.015 or more. The seasonal variations of our simulations are plotted in Figure 23. The individual simulated points have error bars of about 0.005 and the seasonal variations have an amplitude of 0.027. These values are close to those from satellite data.

Our nightly $\sim 2\%$ observational error in each nights measurement of A^* corresponds to an error in of $\sim 0^m.02$ $[A^*]$ which implies measuring A to ± 0.006. This value is comparable to that from satellite data. From the figure, we converted the error in $[A^*]$ into the error in A, which averaging over a year, implies measuring A to 0.006 – even though we have observed a about a third of the nights in the year. These errors are smaller than those we determined using constrained least-squares for A. Thus, we conclude that the regularization has not underestimated the errors in a meaningful way.

7.2. The Earth's Bond Albedo and the Cosmic Ray Flux

One key question is whether there is a solar cycle variation in the earth's reflectance. To probe this, in the lower panel of Figure 30, we compare a twelve month running mean of the Bond albedo calculated from the observational data with a three month running mean of simulated Bond albedo determined for the same times and places as the observations covered. The twelve month running mean eliminates the seasonal variation, which is quite sizeable for the observations (see Figure 23). Further, each twelve month running has enough data that we can obtain a stable solution using regularization. To get, say, a monthly Bond albedo, we would require much greater coverage, which we anticipate from the world-wide earthshine network we are currently constructing. For the simulations shown in the lower panel of Figure 30, we use a three month running mean because the seasonal modulation is more muted. The smaller running mean enables use to compare more local variations in the Bond albedo. It is clear that the simulationed and observational Bond albedo's are closely correlated with both showing a decreasing trend during 1999-2000. The simulated albedo shows a reversal of this this trend beginning near the end of 2000. In the upper panel of Figure 30, we show a thirty day running mean of the cosmic ray flux observed at the McMurdo Station. It is well known that the cosmic ray flux is anti-correlated with solar activity (see http://ulysses.uchicago.edu/NeutronMonitor/Misc/neutron2.html). From the figure, it is clear that the cosmic ray flux and the Bond albedos are closely correlated. In fact, the correlation between the cosmic ray flux and the simulations is 0.67.

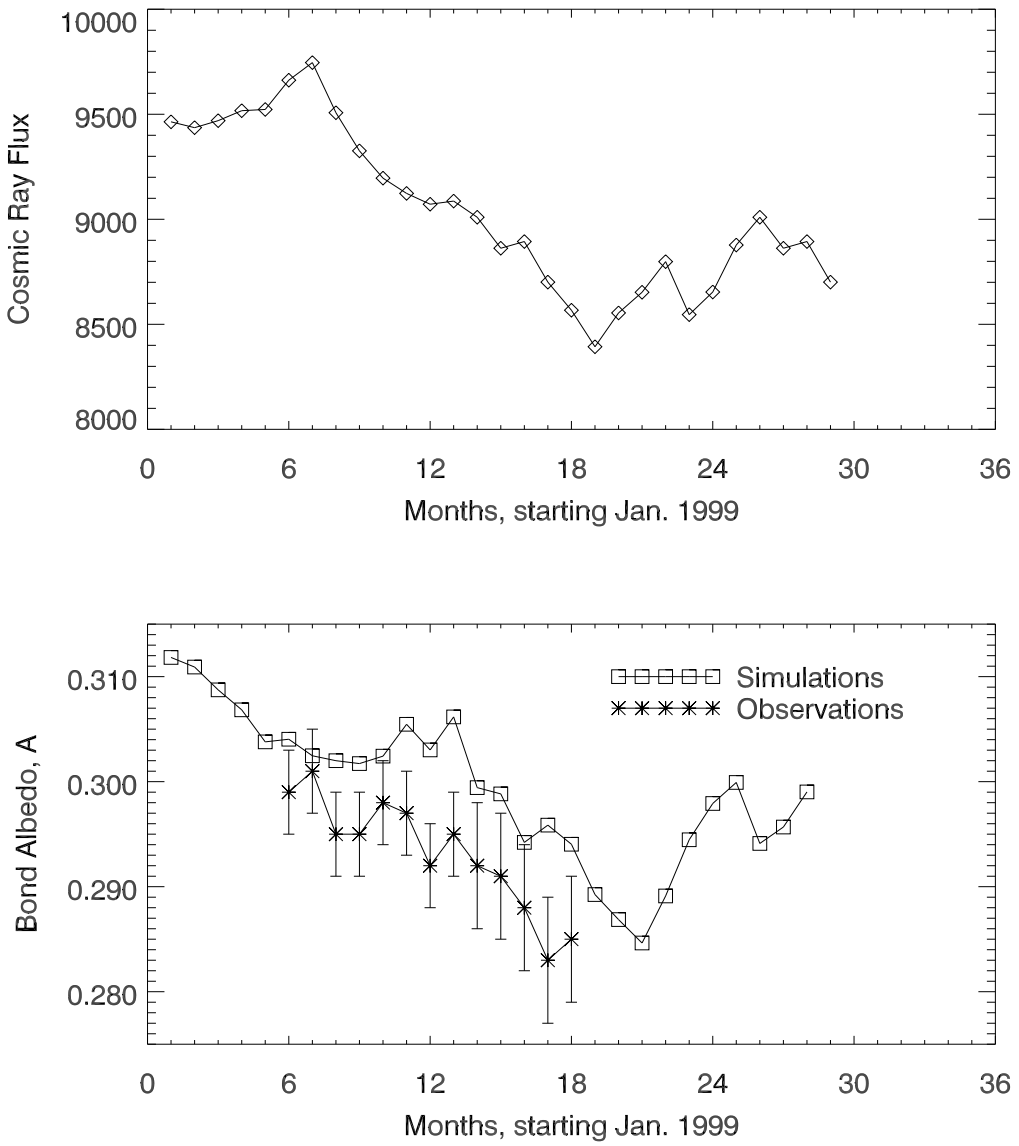

Fig. 30.— The top panel shows the cosmic ray flux at the McMurdo Station (http://www.bartol.udel.edu/ neutronm/) smoothed with a thirty day running mean. The lower panel shows the Bond albedo determined from observations (the X's) and simulations (the boxes). Each observational point is a twelve month running mean, while the simulations show a three month running mean.

Svensmark and Friis-Christensen (1997) have argued that changes in the earth's albedo are anti-correlated with changes in solar activity. They argue that the solar wind more effectively shields the earth from galactic cosmic rays at activity maximum, and that the cosmic rays somehow seed clouds. Figure 30 is consistent with their picture.

To compare the relative roles of the sun's changing irradiance to the earth's changing reflectance in determining the net sunlight reaching earth, we modify Equation (29) to account for the fact that we now do not have to assume a proportionality between the A^*'s and the A's, so that we have directly that

$$\frac{\delta P_{\rm in}}{P_{\rm in}} = \frac{\delta C}{C} - \frac{\delta A}{1-A}. \tag{37}$$

Comparing the observational result of 1999 to that for 2000, we have $\frac{-\delta A}{1-A} \sim 0.009 \pm 0.012$. This change is in phase with the changing irradiance, but is about ten times larger. For the same period, the simulations yield $\frac{-\delta A}{1-A} \sim 0.020 \pm 0.004$(CORRECT ERROR BAR?). Since the observed and simulated Bond albedos seem to scale together, this gives us confidence that we can us cloud cover data from earlier epochs to determine how the earth's albedo changed with solar activity.

7.3. Simulating the Earth's Albedo, 1984-1993

In §6.2, we compared the observed effective albedo betweeen the present time (1999-2000) of high solar activity and the most recent previous time of low solar activity (1994-1995). Further, is §7.2, we compared the evolution of the Bond albedo from the observations to that in the simulations. Here we use the ISCCP-D2 data to compare simulations of albedo from the previous solar cycle. Following Willson and Hudson (1991), we compare the simulated albedo changes between 1986 and 1990. These two times correspond to the solar activity minimum and a time near maximum. Actually, 1991 was the maximum, but we chose 1990 because 1986 and 1990 are roughly at the same phase of the El Niño and Mt. Pinatubo erupted in June of 1991. Over the four years between 1986 and 1990, the solar irradiance increases by about 0.1% (see Figure 18), while the simulated albedo decreases by about 0.004. To compare, we again use Equation (37) to

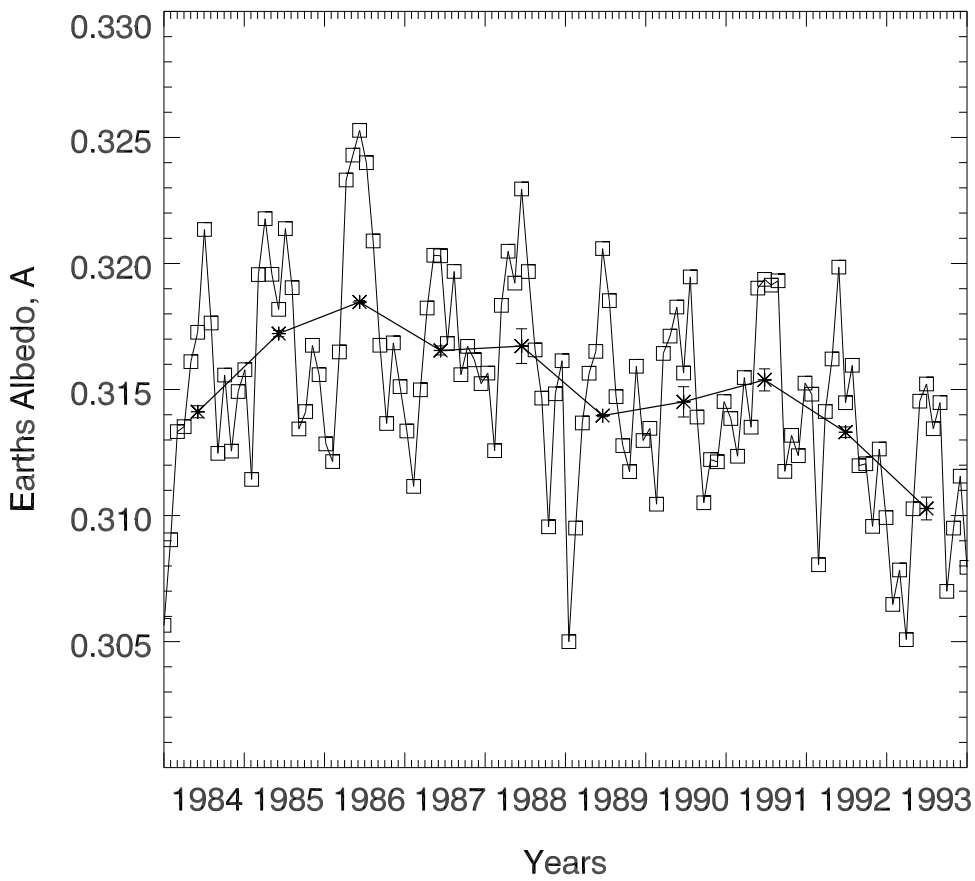

Fig. 31.— Using monthly average cloud cover data from the ISCCP data as input to the scene model, we calculate monthly average of A that are shown by the boxes. We also show the annual averages of A including calculated error bars. The averages are plotted against year.

account for the fact that in the simulations we do not have to assume a proportionality between the A^*'s and the A's As in §6.2, we use Figure 18 to determine the first term on the right hand side of Equation (37), and we find $\frac{\delta C}{C} \sim 0.001$. Using Figure 31, we have $\frac{-\delta A}{1-A} \sim 0.006 \pm 0.001$. The two contributions have the same sign, but the effect of the albedo is about six times larger. This compares quite favorably the $\frac{-\delta A}{1-A} \sim 0.011 \pm 0.007$ from the difference betweeen our 1999-2000 observations and those from 1994-1995.

Thus, the results in §6.2, §7.2 and §7.3, present a consistent picture of the net sunlight reaching the earth depending on the solar cycle, but with the driver being the systematicaly changing terrestrial albedo – rather than the sun's varying irradiance.

7.4. Mean Albedos from Different Cloud Cover Data

Figure 32 shows binned, monthly mean earth's albedos calculated using the ISCCP (thin solid curves) and the WSI data (diamonds and boxes connected by thick lines). The ISCCP data set includes nine years of satellite observations. Solid thick curve shows an averaged over the nine years monthly mean albedo. The error bar for each year is determined from the quality of the fit to the averaged monthly variation in the earthshine. In Figure 31, we see a decrease in A of about 0.008 between 1986 and 1993. As we have seen, this accuracy is well within what we can measure.

Figure 32 shows apparent difference between albedos obtained using different data sets. The WSI albedo is significantly lower than the ISCCP one. The computed averaged ISCCP albedo $\overline{A}$, is 0.315 and the WSI averaged albedo $\overline{A}$ is 0.299. This difference is also well-within what we can measure. The former result arises from cloud cover data that have been most carefully calibrated. The latter is in good agreement with the satellite-derived value of 0.30 (Gibson et al. 1990; Rossow and Lacis 1990). The latter also show the expected seasonal variation with an August minimum and November and May maxima (Danjon 1928; Dubois 1942; Dubois 1947). The dominant source of the seasonal variability is the interplay of the annual cycle of snow/ice cover with the cloud cover; the greater land fraction in the northern hemisphere plays only a small

role. WHAT ABOUT THE OFFSET BETWEEN THE TWO SETS OF CURVES?

8. Discussion

From BBSO, we have observed the earthshine for two years. We determined a large scale average of the earth's albedo for major areas in Europe, Africa and the Atlantic Ocean in our morning observations, when the sun is high in Africa and the Atlantic Ocean and the moon is in its declining phase. We also measured the albedo for large areas in southeast Asia and the Pacific in our evening observations during the rising phase of the moon.

We have compared our results with models of the earth's scenes inputting contemporaneous snow/ice cover from models and cloud cover from satellites. We find a close correlation between the observed and calculated results, with the calculated results uniformly showing milder seasonal variations. From this, we suggest that the models are overly smoothed. We argue that the earthshine data provide an important complement to satellite observations of the earth.

We argue that the albedo we determine is as precise as determined from satellites, while providing an excellent complement. One of the obvious advantages of earthshine observations is having an absolute calibration coming from the bright side of the moon. A clear drawback of earthshine observations has determining the lunar phase function – the reflection of light from the moon as a function of the phase of the moon. We have solved this problem, as demonstrated in §5, so that we know the standard deviation of the phase function to within 0.5%.

From the earthshine data, we see that southeast Asia and West Africa/Southern Europe have very nearly the same albedo. However, the evening obsrvations show a greater spread about the mean which is due to the relatively greater cloud cover variability in southeast Asia. We also see that the albedo is the largest in the spring.

With our level of accuracy, we can track longer time frame changes in the earth's albedo if they are at a climatologically significant level. By extrapolation, we seem to have confirmed the suggested dependence of the earth's albedo on solar activity. We have found that the change in

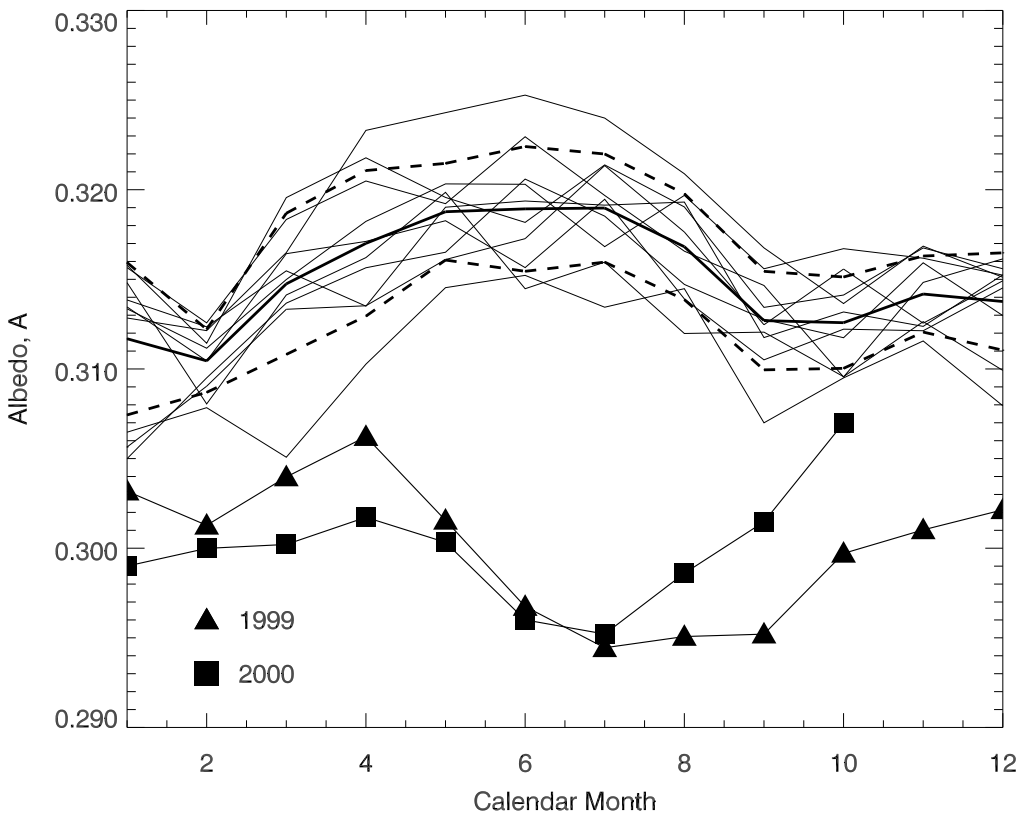

Fig. 32.— Comparison of albedos using different datasets. The WSI results for 1999 and 2000 are indicated by the lines which are connecting the diamonds and boxes. The ISCCP-D2 results cover 1985-1993 and are indicated by the band of light solid lines. The solid line is the mean of 1985-1993 and the dashed lines give the $\pm 1\sigma$ bands about the mean.

the net sunlight into the climate system from a time of high activity to low activity from varying cloud cover is several times greater than changes in the sun's irradiance. However, the two effects work in concert. From our observations, we find from 1994-1995 to 1999-2000 $\frac{\delta P_{\rm in}}{P_{\rm in}}$ increased by 0.012±0.007. Whereas, our simulations show from 1986 to 1990 $\frac{\delta P_{\rm in}}{P_{\rm in}}$ increased by 0.007±0.001. However, the change from 1999-2000, although not statistically significant, seems to go in the opposite direction. Putting that aside, would the other changes be sufficient to be climatologically significant over the solar cycle? The observed change implies an effective increase in the solar irradiance of 11.5±6.7 W/m^2, or a surface averaged (i.e., divide by four) increase of 2.9±1.7 W/m^2 over the five year span. We change here to a surface-averaged value, since that is the way in which the climate model results are presented. Between 1986 and 1990, the simulations using the ISCCP-D2 data imply a surface-averaged increase of 1.7±0.2 W/m^2. The latest Intergovernmental Panel on Climate Change (IPCC) argues for a comparably sized 2.4 W/m^2 increase in greenhouse gas forcing since 1850. The greenhouse gasses are dominated by CO_2, and include CH_4, N_2O and CFCs. IPCC also argues that greenhouse gasses have dominated climate change since the industrial revolution. The 2.4 W/m^2 is larger than changes in the sun's irradiance, aerosols and their effect on clouds. These latter changes are typically associated with global warming. Contrasting the similar size changes due to varying albedo and that due to greenhouse gasses, the change arising from the albedo, over just five years is too abrupt to change the global climate – considering the thermal inertia of the oceans. However, Stevens and North (1996) have used ocean surface temperature data to suggest a subtle variation, with an eleven year period, since 1850.

Svensmark and Friis-Christensen (1997) have argued that changes in the earth's albedo are anti-correlated with changes in solar activity. They argue that the solar wind more effectively shields the earth from galactic cosmic rays at activity maximum, and that the cosmic rays seed clouds. Thus, they explain their observation that there is a greater cloud cover at activity minimum. They argue for a 1.3 W/m^2 increase in surface-averaged flux from 1987 to 1990. Using Figure 31 and the second term on the right hand side of Equation (**??**), we find a comparable increase of 0.9 W/m^2 over the same span. Kirkby (1998 UPDATED REFERENCE) argues that the whole of the warming since the beginning of the industrial revolution may be attributable

to the interplay of cosmic rays and cloud formation. One key to the argument comes from the study of ^{10}Be concentration in Greenland ice cores by Beer, Raisbeck and Yiou (1991) to show that the cosmic ray flux at activity maximum a hundred years ago was greater than it is now at activity minimum. ^{10}Be is created by cosmic rays and falls to earth in about two years. As such, it is a good proxy for the cosmic ray flux. Of course, placing solar magnetism at the heart of terrestrial climate change is controversial, but merits consideration based on the results here and from Svensmark and Friis-Christensen.

Relating these changes in flux to changes in the earth's surface temperature is problematic. We focus here on changes in the earth's emission temperature as would be seen in the IR near 15.5 μm. In those terms, we have from Equation (2) that

$$\frac{\delta P_{\rm out}}{P_{\rm out}} = \frac{4\delta T_e}{T_e}, \tag{38}$$

under the assumption the ϵ in Equation (1) doesn't change. Taking $T_e \approx 255K$, we find a temperature perturbation due to the sun of about 0.1 K and about 0.5 K from the albedo. We note that the largest variations in Figure 31 correspond to temperature variations of about 1 K for the earth. The temperature changes here are simply related to changes in the net sunlight into the climate system, not changes in the temperature of the earth's surface.

We plan an automated network of earthshine telescopes so that we can have long-term data covering all geographic regions.

REFERENCES

Beer, J., Raisbeck, G.M. and Yiou, F., 1991, in *The Sun in Time*, eds. C.P.Sonett, M.S. Giampapa and M.S. Matthews, University of Arizona Press, Tucson.

Bengtsson, 1999, private communication.

Flatte, S., Koonin, S., and MacDonald, G., 1991,in Global Change and the Dark of the Moon, JSR-91-315(McLean, VA: The MITRE Corporation)

Danjon, A., 1928, Ann. Obs. Strasbourg, 2, 165

Danjon, A., 1954, in The Earth as a Planet, ed. Kuiper, p.726, Chicago

Dubois, J., 1942, Ciel et Terre, 58, 352.

Dubois, J., 1947, Bull. Astron., 13, 193

Flatte, S., Koonin, S., and MacDonald, G., 1991. in Global Change and the Dark of the Moon, JSR-91-315 (McLean, VA: The MITRE Corporation)

Franklin, F.A., 1967, J.Geophys.Res., 72, 2963

Fritz, S., 1949, J. Meteor., 6, 277

Gibson, G.G., et al., 1990, SPIE, 1299, 253

Goode, P.R., Denker, C., Marquette, W. and Wang. H., 1999, Solar Phys., in press.

Hapke, B., Physics and Astronomy of the Moon, 2nd edition, ed. Z. Kopal (Academic Press, New York, 1971), 155

Huffman, D., Weidman, C. and Twomey, S., 1990, Colloq Andre Danjon, Jounees 1990, Capitaine and Detarbat, eds. (Paris: Paris Observatory), p. 111

Intergovermental Panel on Climate Change (IPCC), 1992, Climate Change 1992, Suppl. Rep IPCC Sci. Assess, ed. J.T. Houghton, B.A. Callender, S.K. Varney, Cambridge, MA: Cambridge University Press.

Intergovermental Panel on Climate Change (IPCC), 1995, Climate Change 1994, Radiative Forcing of Climate Change and an Evaluation of the IPCC 1992 Emission Scenarios, ed.

J.T. Houghton, L.G. Meira Filho, J. Bruce, H. Lee, B.A. Callender, E. Haites, N. Harris, K. Maskell, Cambridge, MA: Cambridge University Press.

Kennedy, J.R., 1969, M.S. Thesis, Fresno State College, unpublished

Lean, J., 1997, Ann. Rev. Astron., 35, 33

Ram, M. and Stoltz, M.R., 1999, Geophys. Res. Lett., 26, No. 12, 1763

Rougier, M., 1933, Ann. Obs. Strasbourg, 2, Part 3, 203

Settles, J.T., et al., 1988, NASA Reference Publication RP-1184, v. 1

Stevens, M.J. and North, G.R., 1996, J. Atmos. Sci., 53, 2594

Svensmark, H. and Friis-Christensen, E., 1997, J. of Atm. and Solar-Terrest. Physics, 59, 1225

Willson, R.C. and Hudson, H.S., 1988, Nature, 332, 810

Willson, R.C. and Hudson, H.S., 1991, Nature, 351, 42

Very, F., 1915, Astron.Nach., 201, 353

This manuscript was prepared with the AAS LaTeX macros v4.0.